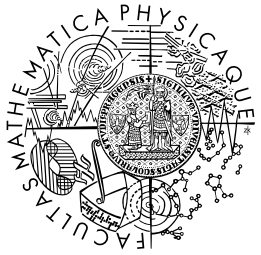

FACULTY
OF MATHEMATICS
AND PHYSICS
Charles University

DOCTORAL THESIS

Martin Hladík

Nanostructures for solar cells: controlling the surface electronic properties by monolayers of carborane molecules

Institute of Physics,
Czech Academy of Sciences, v.v.i.

Supervisor of the doctoral thesis: RNDr. Antonín Fejfar, CSc.
Co-supervisor of the doctoral thesis: Héctor Vázquez Melis, Ph.D.
Study programme: Physics
Study branch: Quantum Optics and Optoelectronics

Prague 2023

I declare that I carried out this doctoral thesis independently, and only with the cited sources, literature and other professional sources. It has not been used to obtain another or the same degree.

I understand that my work relates to the rights and obligations under the Act No. 121/ 2000 Sb., the Copyright Act, as amended, in particular the fact that the Charles University has the right to conclude a license agreement on the use of this work as a school work pursuant to Section 60 subsection 1 of the Copyright Act.

In ..... date ....

Author's signature

First of all, many thanks are dedicated to my supervisor, Antonín Fejfar, and co-supervisor, Héctor Vázquez, for guiding me throughout my doctoral study and teaching me to constantly grow and develop into my next professional life. I also want to thank my former colleague, Aleks Vetuško, who gave me valuable advice important for connecting theory with experiment. Furthermore, I also want to express my gratitude to all my colleagues in the Department of Thin Films and Nanostructures for helpful discussions.

Last but not least, I thank my family, close relatives and friends for their continuous support during my doctoral study.

Title: Nanostructures for solar cells: controlling the surface electronic properties by monolayers of carborane molecules

Author: Martin Hladík

Department: Department of Thin Films and Nanostructures, Institute of Physics, Czech Academy of Sciences, v.v.i.

Supervisor: RNDr. Antonín Fejfar, CSc.; Institute of Physics, Czech Academy of Sciences, v.v.i.

Co-supervisor: Héctor Vázquez Melis, Ph.D.; Institute of Physics, Czech Academy of Sciences, v.v.i.

Abstract: Doped layers of crystalline silicon are currently the main driver of conventional photovoltaic devices. Direct introduction of group III and V atoms into the silicon matrix is still the mainstream of mass production of doped silicon. In this thesis, we are interested in non-invasive ways of doping of silicon wafers through the adsorption of molecules with a large intrinsic dipole moment on the semiconductor surface. These molecules, namely carboranedithiols, create a self-assembled monolayer accompanied by the surface dipole formation. In order to stabilise the dipole layer, an interfacial charge transfer can occur between the adsorbate and the substrate, modifying the density of accumulated charge carriers just below the silicon surface. These are the fundamental features of the surface transfer doping of the silicon substrate where we employ the carboranedithiol molecules as mediators of adsorbing dipole layer. Regarding the structure of the thesis, we first test the carboranedithiol molecules on gold, and then we move on to the issue of silicon-molecule junctions. We characterise the geometry and the electronic properties of the carboranedithiol molecules on both of these substrates by means of atomistic simulations based on a density functional theory.

Keywords: surface transfer doping, work function, silicon-carboranedithiol junction, self-assembled monolayer, van der Waals density functional theory

Contents

Introduction

Energy, its permanent supply and consumption are part and parcel of modern world. For such a way of life, it was necessary to learn to use a wide range of resources freely available in nature (coal, crude oil, natural gas, sunlight, falling and flowing water, blowing wind, biomass, uranium, etc.). The important milestone was the Industrial Revolution which started the extraction and processing of fossil fuels (coal, oil, natural gas), the use of which became the driving force of the world energy industry in the 20^{th} century. However, since the turn of 1970's and 1980's, an alternative solution has been sought because high-carbon resources have a negative impact on economic stability and Earth's climatic conditions. This alternative solution is renewable energy sources as the richest (and oldest) area of primary sources that nature offers. Current renewable technologies typically use wind energy (onshore and offshore), solar energy (thermal and photovoltaic), hydroelectric power, marine energy, geothermal energy, ambient heat captured by heat pumps, bioenergy (solid biofuels and renewable waste, biogas, liquid biofuels), etc. Renewable sources excel in a high level of diversity which generally supports economic stability and possess a minimum carbon footprint. Currently, they are the main driver of the growing share of electricity in the world energy consumption (WEC). Electricity from renewable sources can be used for the electrolytic production of "green" hydrogen as a potentially suitable fuel for types of energy demand that rely on fossil fuels and remain difficult to electrify (shipping, aviation, steel and chemical industry, refineries, etc.) [1].

Among all end-use energy sources, electricity is a unique guarantee of excellent final conversion efficiency, precise consumption control, productivity, flexibility and versatility across all energy sectors (industry, transport, buildings, commercial and public services, etc.). Currently, electricity accounts for about 20 % of the total of $\sim$120 PWh of annual WEC. By 2050, it should be almost 30 % of the more than 150 PWh under current world policies [2]. This electrification path should be driven by renewable technologies, namely those using wind and solar energy. The popularity of wind and solar energy technologies began to increase in the early 2010's, mainly due to their steepest drop in costs from all available electricity generation sources [1].

In addition to electrification, there are also key issues regarding the gradual decarbonisation of all energy sectors. In particular, it is about the transformation of energy towards zero net emissions by 2050 [2]. Solar photovoltaic (PV) systems are the main driver of the world energy decarbonisation and we are interested in them in more detail in the following section.

i Solar photovoltaics

Solar photovoltaics (PV) occupies an extraordinary position in the modern electric power industry because it produces electricity from sunlight through a PV effect which is a unique direct energy conversion. The PV effect takes place in a PV cell, a planar semiconductor photodiode. In conventional use, however, individual PV cells are connected in series or in parallel into larger assemblies, PV modules, in order to achieve required voltages and currents. Appropriate interconnection of PV modules creates a PV array, the predominant power-generating component of solar farms.

Although the efficiency of electricity production in utility-scale PV modules (16 - 21 %) is lower than, for example, in utility-scale wind (30 - 45 %) or water turbines (85 - 90 %), in many other regards the solar PV is the most useful renewable technology and the most important for the future of electric power industry. Unlike other common

ways of renewable electricity generation, the PV systems:

- are quiet, have no mechanical components that would otherwise wear out, and may reach lifetimes above 30 years or more
- use a natural resource that is practically inexhaustible, clean, and free
- are respectful of living ecosystems, do not change the environment
- consume no fuel and produce no contaminants during the operation
- are globally applicable (installation can also be set up in regions with less sunlight)
- have a high specific power (power-to-weight ratio), which allows their use on roofs, especially in places without access to power grid
- require little maintenance if they are properly manufactured and installed
- are flexible in a wide range of energy applications from ordinary households (of tens of m^2 size) to large PV power plants (of units of km^2 size)

On the other hand, wind turbines are noisy and require much more maintenance than PV modules. Moreover, entire wind farms are usually located in distant places with little access to actual end-users and negatively affect the environment of local fauna. Hydroelectric power plants, although by far the most efficient in generating electricity, are even worse in terms of environmental impact, as their implementation is mediated by large dams. The construction of a dam has the ability to change the entire ecosystem, takes over the natural flow of waterways, prevents fish migration, and affects wildlife in the nearby area.

Solar PV is currently the fastest growing market in the electric power sector due to the many advantages it has over other technologies. In the 2010's, it experienced the largest increase in electricity generation and power capacity addition of all available electricity generation sources. Since the current decade, the PV industry has reached breakthrough values; in 2021, the total solar PV generation exceeded 1 PWh per year, and in 2022, the total installed PV capacity overcame 1 TWp [2]. Despite the fact that such a pace is still not enough to meet the already promised climate commitments by 2050, current intentions are to accelerate the growth of PV electricity and added capacity and make solar PV a truly new king of electric power industry. The permanently declining technological costs of utility-scale solar PV systems are quite helpful to these intentions. Their levelised costs of energy[①] in the European Union is below 50 USD/MWh, in China already below 35 USD/MWh. By 2050, these costs should be lower by ∼40 and ∼55 %, respectively [2].

Photovoltaics of crystalline silicon wafers

Crystalline silicon (c-Si) solar cells have always been the most successful systems of the global PV market [3]. Their basic building block is a c-Si wafer, a thin slice of semiconductor, which is modified into the final cell structure by industrially established technological procedures [4]. The great advantage of silicon lies in its plentiful occurrence in nature, as it is the second most abundant element in the Earth's crust. Native silicon does not occur in its elemental form and is primarily a part of rock-forming minerals. It forms compounds with oxygen, the best known of which is quartz, chemically silicon dioxide (SiO_2).

[①] This quantity express the price of a unit of produced energy the plant must achieve to cover all costs incurred during its life cycle.

Fabrication of c-Si wafers. For the manufacturing of c-Si wafers, high purity solar-grade (99.99 %) elemental silicon is required. It is produced by melting quartz in the presence of carbon and subsequent purification from residual impurities. The melt of solar-grade silicon is then subjected to a crystal growth process to form monocrystalline or multicrystalline forms of silicon ingots. The monocrystalline silicon (mono-Si) ingot is a cylindrical structure with a diameter of about 22 to 30 cm created by the Czochralski crystal growth process. In this method, a dislocation-free silicon seed of a specific crystallographic orientation, most commonly (100), is slowly pulled from the melt and rotated to create a cylindrical ingot. The grown ingot is then transversely cut to mono-Si wafers having a thickness of about 160 to 170 μm and a "pseudo-square" shape. Regarding the crystallisation of multicrystalline silicon (multi-Si), the respective ingot has a rectangular shape and is produced from the molten solar-grade silicon by a directional solidification process without any reference crystal orientation. The solidified ingot is then cut to bricks and square multi-Si wafers [4, 5].

Multi-Si ingots and wafers have a much more defective structure than mono-Si equivalents. The more defective structure leads to the lower PV efficiency of the resulting solar cells. Defects manifest themselves in the form of energy states in the band gap which trap electrons and holes from the conduction and the valence band edge, respectively, and cause their mutual recombination. Therefore, the lifetime of the charge carriers is shortened and the PV cell efficiency is reduced. Solar cells made from mono-Si wafers have a higher conversion efficiency but at the cost of more expensive and time-consuming production. In terms of specific imperfections of multi-Si, there are mainly surface defects caused by interfaces between regions (grains) of different crystallographic orientations as well as point and line defects induced by vacancies or interstitial Si atoms. In mono-Si, due to the uniform crystallographic orientation, grain boundaries do not occur; dominant are point defects.

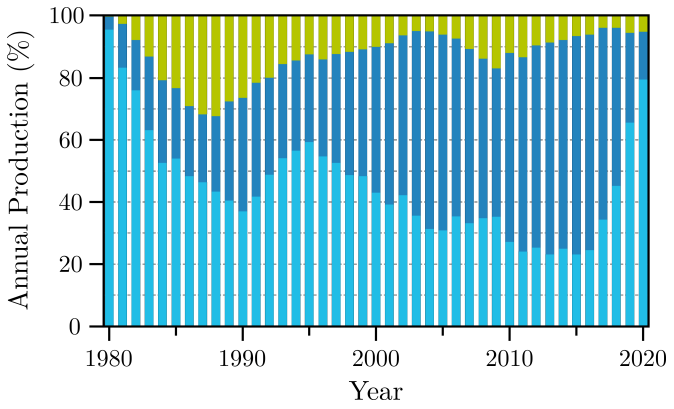

Figure 1: Annual PV production by technology. Time evolution of the percentage share of given technologies in the annual PV production from 1980 to 2020. Thin film, multi-Si, and mono-Si, are marked with green, blue, and cyan bars, respectively. Taken from [3].

Global PV production. At present, mono-Si is unambiguously the mainstream of the global PV market. It accounts for more than 80 % of annual PV production and its dominance should continue to grow in the coming years [5]. However, in the first half of the 2010's, the situation was completely different and mono-Si, with an average share of annual production slightly above 20 %, was at its historic minimum (Fig. 1). The market share of a given PV technology (mono-Si, multi-Si, thin film) grows as its profitability increases within the life cycle of conventional PV systems, especially PV modules. Thus, between about 2010 and 2015, multi-Si PV technology was the most

cost-effective for mass production. Eventually, the entire PV market returned to its original roots and entered the new era of mono-Si in which we live today.

The recovery of mono-Si was ensured by quite revolutionary changes in the manufacture of wafers and solar cells, coming after 2010 and causing a sharp drop in market prices and a significant increase in power outputs of conventional PV modules during the 2010's. With falling market prices, the price gap between silicon technologies has narrowed greatly and mono-Si modules are currently more expensive than multi-Si ones by about 0.01 *USD/Wp* [6]. On the contrary, with growing module power outputs, the difference between mono-Si and multi-Si technology has magnified, specifically in favour of mono-Si modules which are currently ahead of multi-Si ones by several tens of *Wp* [5, 7].

Regarding the particular causes of the mono-Si market resurrection, it is mainly the size diversification of silicon ingots and wafers towards larger wafer areas producing higher power outputs with minimal or almost no impact on other production costs. This reduces all possible costs per *Wp*, including the manufacturing costs of solar cells and modules and other construction costs of solar power plants not related to PV modules (wiring, mounting systems, solar inverters, energy storages, etc.) [8]. For mono-Si, the growth of power output with wafer area is more efficient and therefore the cost reduction is faster. In addition, after 2012, the mono-Si market began to be supported by the advent of solar cells using various rear side passivation technologies, namely the passivated emitter and rear side (PERx) solar cells, pushing the PV efficiency well above the level of 20 % of standard cells [8, 9]. The main innovation of PERx cell architectures is the presence of the rear passivation layer which not only acts as a potential barrier for minority carriers (in standard cells) but also reduces surface and bulk defects of silicon. However, due to additional costs, this advanced surface technology requires higher quality and less defective mono-Si base to appreciable increase power outputs [9]. Over 60 % of today's PV production is mediated by mono-Si PERx cells with an average PV efficiency of about 23 % [5].

ii Doping of semiconductors

Doping is part and parcel of the entire semiconductor industry. It is the process of introducing a small amount of impurities (dopant atoms) into the host lattice of an intrinsic semiconductor in order to modify the charge carrier density inside the matrix. When the impurity atoms are electron donors, excess electrons as free negative charge carriers are released into the semiconductor (n-type doping), bringing the Fermi level, E_{F}, closer to the conduction band. On the contrary, the introduction of electron acceptors into the lattice induces the formation of empty valence electron orbitals, which in solid-state physics are referred to as "holes" (p-type doping). These are positively charged quasi-particles that can move freely throughout the crystal and cause a shift of E_{F} towards the valence band. The main goal of both n-type and p-type doping is to tune the electrical conductivity of the semiconductor to the required level for the given technology.

With respect to group IV semiconductors, the appropriate dopant atoms are group III electron acceptors (p-type) and group V electron donors (n-type). In the case of silicon, the typical p-type dopant is boron or gallium and the n-type dopant is phosphorus. Based on the atomic density in the intrinsic (i-type) c-Si of about 5×10^{22} cm^{-3}, the usual doping concentration in the doped c-Si approximately ranges from 10^{13} to 10^{18} cm^{-3}. Below 10^{18} cm^{-3}, silicon is considered an extrinsic semiconductor with a light ($< 10^{14}$ cm^{-3}) or a moderate level of doping. When 10^{18} cm^{-3} is exceeded, silicon is degenerate [10].

Lightly doped mono-Si wafer is the basic pillar not only of PV systems but also of many electronic devices. Extrinsic mono-Si is fabricated already during its crystallisation by adding a suitable amount of alloying elements to the melt from which the lightly doped mono-Si ingot grows. For photovoltaic purposes, after cutting the doped ingot into wafers, the doping level of the front wafer side is inverted to the opposite type of conductivity to form a thin heavily doped emitter layer and a *pn*-junction between the emitter and the rest of the lightly doped silicon base. Because the emitter is only a few hundred nanometres wide and is therefore much thinner than the wafer itself [4], the *pn*-junction is practically located just below the front silicon surface. This is essential for the proper operation of the solar cell because sunlight falls on the front wafer side where it is absorbed the most. As a result, more light energy reaches the depletion region of the *pn*-junction where more charge carriers, i.e. electron-hole pairs, are generated. These carriers contribute to the photo-generated current and thus to the overall cell efficiency.

Homogeneous emitter layers in c-Si wafers are conventionally fabricated by high-temperature diffusion from gaseous phase and, to a much lesser extent, also by ion implantation [5]. However, state-of-the-art technologies in the semiconductor industry require more and more miniaturised electronic devices with more uniform, thinner, or even less concentrated doped layers. In this regard, gas phase diffusion may in some cases lack sufficient uniformity and control over the dosing of dopant atoms. Ion implantation can cause crystal damage due to a high-energy ion bombardment of the surface [11–13]. These shortcomings can be overcome by alternative and more modern technologies based on monolayer doping (MLD) and surface transfer doping (STD), which are able to form shallow ($<$100 nm) to ultra-shallow ($<$10 nm) doped regions in the silicon matrix [13, 14]. We elucidate the key features of these methods in the following paragraph.

MLD and STD-based strategies. Dopant mediators of MLD or STD-based approaches are dopant-containing or electronically active molecules, respectively, grafted onto the surface of the host semiconductor via chemical reactions between hydrogen terminal groups of the H-passivated silicon wafer[②] and anchoring functional groups of molecular adsorbates. The covalently bonded molecules are arranged into large organised two-dimensional arrays known as self-assembled monolayers (SAMs)[③] which deterministically cover the entire silicon wafer [14, 15].

In the case of MLD, the doped layer is formed by means of a rapid high-temperature annealing step that breaks the grafted dopant-rich monolayer into atoms and incorporates them into the Si matrix. The result is a uniform, shallow, and heavily doped region whose very well tunable concentration and depth are particularly useful in the production of heavily doped source/drain contacts in field-effect transistors [11, 12, 14, 19].

Unlike MLD, STD strategy is non-invasive because it does not physically introduce foreign atoms into the host semiconductor lattice. Instead, it utilises interfacial charge transfer across the silicon-molecule interface, thereby modifying the energy level alignment between the substrate and the adsorbed monolayer [20–22], including the position of E_F within the semiconductor gap [15, 23]. In the following Sec. iii, we deal with a detailed description of STD of mono-Si surface.

[②] It is the oxide-free silicon surface prepared by a wet chemical etching of the conventional SiO_2-covered mono-Si wafer in a dilute aqueous solution of HF [14, 15].

[③] The monolayers are "self-assembled" because their formation is controlled by a thermodynamically spontaneous organisation of their building blocks into stable, clearly defined structures from which clearly defined properties are derived. SAMs not only reduces surface free energy but also significantly interferes with physical and chemical properties of the substrate [16–18].

iii Surface transfer doping

The building blocks of the electronically active monolayer are molecules having electron-donor or electron-acceptor properties. Due to these features, electron exchange takes place between the substrate and the adsorbed monolayer, leading to a local alteration of the charge carrier density inside the semiconductor [13, 15]. The electronic activity of the adsorbed structure depends on its polarity, i.e. on its electric dipole moment, μ. Each polar molecule, or polar molecular adsorbate, has its own intrinsic molecular dipole moment, μ_{Mol}, whose magnitude changes with respect to the gas phase when adsorbed on the surface. The larger the magnitude of μ_{Mol}, the more extensive the electron exchange between the substrate and the adsorbed monolayer. In this thesis, we use the convention in which any type of μ points from the negative to the positive pole.

Stabilisation of dipole layer. The grafted monolayer composed of molecular permanent dipoles represents a dipole layer on the surface in which the individual building blocks interact with each other, in particular by means of intermolecular dipole-dipole interactions. As the level of organisation and tight arrangement of the molecular dipoles increases, the electric field strength across the dipole layer amplifies and destabilises the system. If the potential energy of this electric field exceeds the binding energy of the monolayer-substrate interaction, the junction breaks down. Therefore, in order for the dipole layer to "self-assemble" without "self-destruction", the intensity of the dipole-dipole repulsions must be mitigated, bringing the transverse electric field strength below the breakdown value [22, 24].

The electric field across the dipole layer depends only on the projection of μ into the surface-normal direction, $\mu_{\perp}$. Hence, we always examine the dipole μ_{Mol} only in terms of its surface-normal component, so $\mu_{\text{Mol}} \parallel \mu_{\perp}$[4]. The path getting below the breakdown electric field is thus a matter of certain processes causing a reduction in the magnitude of μ_{Mol}.

The reduction of μ_{Mol}, or the molecular depolarisation, takes place either with or without the cooperation of the substrate. Without the substrate participation, the dipole layer depolarises itself, either by intramolecular charge rearrangements or by molecular conformation changes. However, these stabilisation ways only occur when individual building blocks are very polarisable or are assembled into more flexible configurations, respectively. A typical example of conformational changes is the tilting of the molecular dipoles to the surface [22, 24].

In the case of a highly organised (close-packed) dipole layer made up of molecules with low polarisability, the reduction of the electrostatic field across the layer takes place in the cooperation with the substrate by means of interfacial charge transfer. During this process, the charge, or rather the electron, crosses the interface between the substrate and the molecular adsorbate and is therefore exchanged between these subsystems [24]. In the case of the semiconductor substrate, the charge transfer modifies the density of accumulated charge carriers[5] just below the surface, creating the subsurface space-charge layer. Depending on whether the accumulated carriers are either electrons or holes, the space-charge region below the interface is either the n-type or the p-type doped layer, respectively, and is analogous to the doped layer created by

[4] With this expression, we do not indicate any constraints to our study, rather we point out the relevance of only the perpendicular component.

[5] They are analogous to free charge carriers. In the context of STD, however, we are more careful about the label "free", because in the doping process, we rather observe their "accumulation" just below the surface of the substrate.

the conventional introduction of dopant atoms into the substrate [13, 15, 22, 25, 26].

The mutual collaboration between the semiconductor and the adsorbed dipole layer leading to the stabilisation of grafted molecules and the formation of the space-charge region just below the semiconductor-molecule interface is the basic essence of STD strategy. The course of STD depends on the magnitude and the orientation of μ_{Mol}. In this thesis, we always align the surface normal along the z-axis, so $\mu_{\perp} \equiv \mu_{\mathrm{z}}$ and $\mu_{\mathrm{Mol}} \parallel z$-axis. When μ_{Mol} is pointed away from the surface ($\mu_{\mathrm{Mol}} > 0$), the molecular dipole layer donates electrons to the semiconductor, making it an n-type doping agent (Fig. 2). In the case of μ_{Mol} pointed towards the surface ($\mu_{\mathrm{Mol}} < 0$), the dipole layer is an p-type dopant because it withdraws electrons from the substrate (Fig. 3).

To describe the STD approach, we use the concept of the energy diagram which is a plot of allowed electronic energy levels as a function of position along the surface normal. In the following text, we first describe the individual parts of the energy diagram of the silicon-molecule junction and clarify all the important quantities associated with the STD process. Then, we move on the detailed characterisation of the n-type and the p-type STD of the silicon surface.

Energy diagram of the silicon-molecule junction

Fig. 2 and 3 show the patterns of the energy diagram of the silicon-molecule junction with the electron-donating and the electron-withdrawing properties of the adsorbed molecular dipole layer, respectively. The energies of the most prominent electronic states in the system are depicted on the vertical axis. The horizontal axis (the z-axis) shows the spatial positions of these electronic states along the surface normal that points from left to right in the diagram.

Along the surface-normal direction, the diagram can be divided into four cross-sectional regions: (1) the intrinsic bulk silicon (green), (2) the subsurface space-charge layer of accumulated electrons/holes (blue/red), (3) the adsorbed dipole layer, or the monolayer, of adsorbed molecules having the intrinsic dipole μ_{Mol} (yellow), and (4) the vacuum above the covered surface. The semi-transparent white area passing through the intrinsic bulk silicon and the subsurface space-charge layer indicates the band gap of the silicon substrate. We discuss the individual parts of the energy diagram in detail below.

(1) The intrinsic bulk silicon. The green cross-sectional regions on the left-hand side of Fig. 2 and 3 are identical and represent the energy diagram of intrinsic silicon. The bottom area introduces the valence band confined from above by the valence-band edge (maximum), E_{VB}. The parallel progressively-transparent top area shows the conduction band limited from below by the conduction-band edge (minimum), E_{CB}. The valence and the conduction band are the regions of allowed electronic Si states closest to E_{F} and are therefore responsible for the final electrical conductivity of the semiconductor. E_{CB} and E_{VB} are separated by the band-gap energy, E_{g}:

$$E_{\mathrm{g}} = E_{\mathrm{CB}} - E_{\mathrm{VB}} \tag{1}$$

where the silicon E_{F} is located. At the absolute zero temperature, i.e. $T = 0\ K$, each intrinsic semiconductor has its E_{F} in the middle of the band gap, i.e. in $(E_{\mathrm{CB}} + E_{\mathrm{VB}})/2$. As the temperature rises, the position of E_{F} leaves the mid-gap due to the different effective densities of states of the conduction and the valence band. In the case of intrinsic silicon, the rising temperature shifts E_{F} towards E_{VB}. When room temperature

($T = 300\ K$) is reached, the band gap of silicon is $E_g \approx 1.12\ eV$ [10, 27, 28][6] and the silicon E_F is below the middle of the band gap by about $7 \times 10^{-3}\ eV$ [10].

Allowed Si states are the levels of any electron bound to the solid. Above all these states, there is the vacuum level, E_{vac}, as the lowest energy level that the electron have to reach in order to leave the solid. The electron staying on E_{vac} is at rest with respect to the solid and is located just above the surface. The energy barrier that prevents the electron from escaping into the free space corresponds to the work function, Φ, of the given material. This barrier culminates at E_{vac} and is therefore defined as the difference:

$$\Phi = E_{vac} - E_F\,. \tag{2}$$

The equation applies to both intrinsic and doped semiconductor [20, 23].

In this thesis, we consider the hydrogen-terminated silicon without any other molecular adsorbates to be the intrinsic form of the silicon substrate. Its E_{vac} is shown on the left-hand side of Fig. 2 and 3. The energy difference between this level and the silicon E_F gives the work function of the bare hydrogen-terminated silicon, Φ_{Si}.

(2) The subsurface space-charge layer. When moving from the bulk in the surface-normal direction, the silicon bands pass into the subsurface space-charge layer. The blue region in Fig. 2 introduces the layer of accumulated electrons and the complementary red one in Fig. 3 specifies the layer of accumulated holes. As in the bulk region, the valence and the conduction band are characterised by the more opaque bottom and the gradually transparent top area, respectively.

The thickness of the subsurface space-charge layer depends on the accumulated-carrier density profile. From the region of intrinsic semiconductor towards the silicon-molecule interface, the accumulated-carrier density across the space-charge layer grows, E_F gets closer to the edge of the band gap, and the silicon substrate becomes more and more doped semiconductor. Due to the electronic equilibrium between the intrinsic and the doped silicon, the Fermi levels of these regions are aligned and the band edges are bent either upwards or downwards [15, 20, 23].

Regarding the band bending, ΔU_{BB}, itself, its value (sign and magnitude) corresponds to the difference between the band edge at the silicon-molecule interface and the band edge in the bulk region of intrinsic silicon. The STD process does not change the silicon E_g and therefore ΔU_{BB} is the same for both E_{VB} and E_{CB}. The type and the concentration of accumulated carriers govern the sign and the magnitude of ΔU_{BB}, respectively, and also the position of E_{vac} relative to the silicon Fermi level. The band edges and E_{vac} proceed simultaneously across the space-charge layer because the ability of a given type of accumulated charge carrier to escape into the free space increases in direct proportion to its concentration in the solid. Therefore, at the interface where the bending of E_{VB} and E_{CB} is maximum, ΔU_{BB} is equal to the energy shift of E_{vac} caused by the interfacial charge transfer [23, 25, 26, 29].

(3) The adsorbed dipole layer and (4) the vacuum. When proceeding further in the surface-normal direction, the energy diagram leaves the silicon bands, crosses the silicon-molecule interface, and enters into the region of the adsorbed dipole layer and the surrounding vacuum. The molecular dipole layer is highlighted in Fig. 2 and 3 by the faint yellow area. The vacuum is represented by the empty area to the right of

[6] Based on experimental studies of optical properties of silicon at various temperatures T, E_g of silicon is a decreasing function of T. At $T = 0\ K$, the extrapolated values of E_g are between 1.16 and 1.20 eV [27, 28].

the dipole layer. Blue/red arrows inside the yellow area show the orientation of μ_{Mol} of each molecular adsorbate of the stabilised dipole layer.

The adsorption of the electronically active molecule causes the change of the surface dipole, $\Delta\mu_{\mathrm{surf}}$, which is the sum of the intrinsic dipole μ_{Mol} and the dipole of the newly formed substrate-molecule interface, μ_{int}. The $\Delta\mu_{\mathrm{surf}}$ gives rise to the surface potential-energy step, ΔU_{surf}, across the layer via the relation [30]:

$$\Delta U_{\mathrm{surf}} = -\frac{e\,(\Delta\mu_{\mathrm{surf}})}{\epsilon_0 \Omega} = -\frac{e\,(\mu_{\mathrm{Mol}} + \mu_{\mathrm{int}})}{\epsilon_0 \Omega} \tag{3}$$

where e is the elementary charge, ϵ_0 the vacuum permittivity, and Ω is the surface area taken by one molecule of the monolayer. The equation show ΔU_{surf} as the function of the ratio $\Delta\mu_{\mathrm{surf}}/\Omega$, i.e. the change of the surface dipole density. According to the vacuum level path that spans the entire energy diagram, ΔU_{surf} is equal to the difference between E_{vac} in the vacuum region and E_{vac} at the silicon-molecule interface. This difference corresponds to the energy shift of E_{vac} caused by the surface dipole [25, 29].

The value of E_{vac} on the right-hand side of Fig. 2 and 3 corresponds to E_{vac} just above the surface of the silicon-molecule junction. The energy difference between this level and the silicon E_{F} gives the work function of the silicon-molecule junction, $\Phi_{\text{Si-Mol}}$. The line of E_{F} is artificially elongated from the silicon substrate region to the vacuum in order to make it easier to read $\Phi_{\text{Si-Mol}}$ and other important quantities connecting the properties of the silicon and the dipole layer.

Region (1-4): work function change. After the detailed analysis of the vacuum level path in Fig. 2 and 3, we can conclude that the adsorption and the subsequent stabilisation of the dipole layer on the hydrogen-terminated silicon surface leads to the total shift of E_{vac} which is equal to the sum of ΔU_{BB} and ΔU_{surf}. This total shift corresponds to the work function change of the silicon substrate, $\Delta\Phi_{\mathrm{Si}}$:

$$\Delta\Phi_{\mathrm{Si}} = \Phi_{\text{Si-Mol}} - \Phi_{\mathrm{Si}} = \Delta U_{\mathrm{BB}} + \Delta U_{\mathrm{surf}}\,. \tag{4}$$

The equation shows that $\Delta\Phi_{\mathrm{Si}}$ depends on both the interfacial charge transfer between both subsystems and the stabilised surface dipole [25, 26, 29].

Region (3): carrier injection barriers. An appropriate measure of interfacial charge transfer between the substrate and the adsorbate are the barrier heights for electron injection, ΔU_{e}, and for hole injection, ΔU_{h}, or more briefly, the electron and the hole injection barriers, respectively. The quantities are the potential energy differences between E_{F} of the substrate and frontier orbital energies of the molecular adsorbate:

$$\Delta U_{\mathrm{e}} = E_{\mathrm{LUMO}} - E_{\mathrm{F}}\,, \tag{5}$$

$$\Delta U_{\mathrm{h}} = E_{\mathrm{F}} - E_{\mathrm{HOMO}}\,, \tag{6}$$

where E_{LUMO} is the energy of the lowest unoccupied molecular orbital (LUMO) and E_{HOMO} the energy of the highest occupied molecular orbital (HOMO). The greater the electron-donating properties of the adsorbed molecules, the smaller ΔU_{e} and the larger ΔU_{h}. In the case of electron-withdrawing molecules, the opposite trends apply to the barrier heights.

Similar to the band bending or the barrier heights for carrier injections, one can also quantify the interfacial charge transfer by monitoring the differences: E_{LUMO} - E_{CB}, or

E_{VB} - E_{HOMO}, and their changes due to the adsorption. With the increasing electron-donating character of the adsorbate, the first difference decreases and the second one increases. For the increasing electron-withdrawing properties, the opposite behaviour applies to the both differences.

n-type STD of the silicon surface

When the adsorbed dipole layer has $\mu_{\mathrm{Mol}} > 0$ (Fig. 2), the negative pole of μ_{Mol} oriented more towards the silicon-molecule interface donates a negative charge to the substrate in order to reduce the dipole magnitude. The donated electrons pass through the interface and reach only the nearby subsurface Si layers where they acquire the features of accumulated negative charge carriers. This creates the subsurface space-charge layer of accumulated electrons (blue region) in which E_{CB} gets closer to E_{F}, i.e. $\Delta U_{\mathrm{BB}} < 0$. Thus, in this region, the substrate achieves the properties of the *n*-type semiconductor. Along the surface normal, the number of accumulated electrons in the conduction band and their probability of escape from the semiconductor increase simultaneously within the space-charge layer. Therefore, E_{vac} decreases at the same rate as E_{CB} and E_{VB}.

After reducing the size of μ_{Mol}, the change of the surface dipole density is still positive and, according to Eq. 3, creates the negative ΔU_{surf} across the dipole layer. According to Eq. 4, this surface dipole contribution together with the negative band bending (*n*-type STD) bring about the negative $\Delta\Phi_{\mathrm{Si}}$.

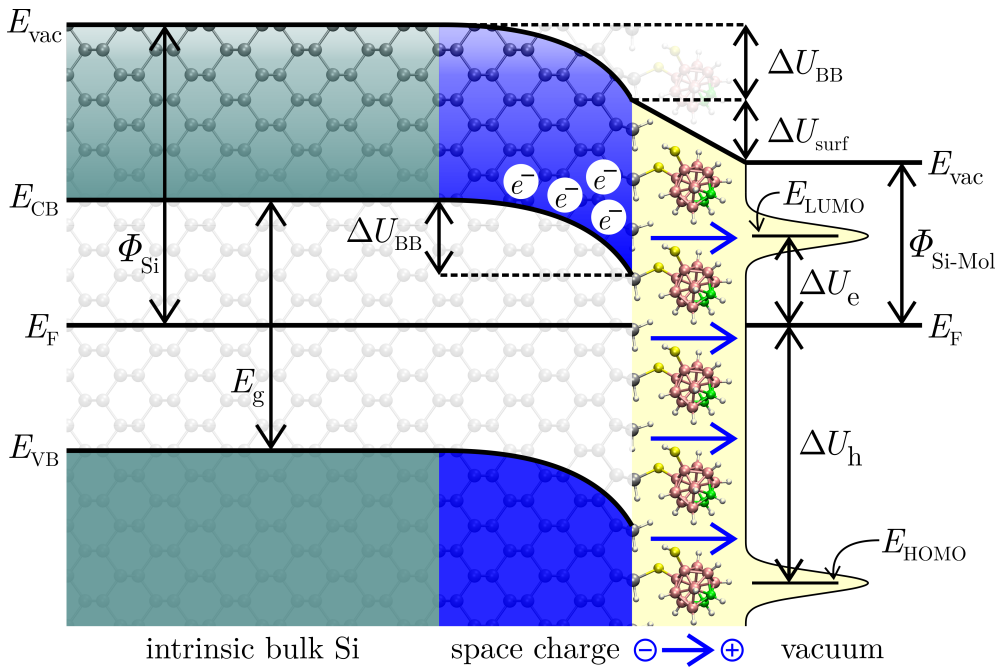

Figure 2: *n*-type STD of the silicon substrate. Energy diagram of the hydrogen-terminated mono-Si surface modified with electron-donating molecules with μ_{Mol} pointed away from the surface. All labelled quantities and colour-coded cross-sectional regions are described in the main text. White circles with "e^-" labels mark accumulated electrons.

p-type STD of the silicon surface

As for the adsorbed dipole layer having $\mu_{\mathrm{Mol}} < 0$ (Fig. 3), the appropriate interfacial charge transfer, of course, again leads to the reduction in the magnitude of μ_{Mol}, but this time it proceeds in the opposite direction than in the case of the *n*-type STD. In particular, μ_{Mol} is oriented towards the silicon by its positive pole, making the

dipole layer capable of withdrawing electrons from the nearby subsurface Si layers. The withdrawn electrons come from the valence band of the semiconductor where they leave behind empty valence orbitals, i.e. accumulated holes. The result of this electron exchange is the formation of the subsurface space-charge layer of accumulated holes (red region) in which the silicon substrate acquires the character of the p-type semiconductor. The corresponding ΔU_{BB} is positive, or E_{VB} gets closer to E_{F}.

In the surface-normal direction, the growing density of accumulated holes proportionally lowers the probability of escape of the valence electron from the solid. Thus, the increase of the band edges coincides with the increase of E_{vac} within the space-charge layer. Regarding the stabilised dipole layer itself, the positive ΔU_{surf} passes through it due to the negative change of the surface dipole density (Eq. 3). This effect of the surface dipole and the positive band bending (p-type STD) together cause the positive $\Delta\Phi_{\mathrm{Si}}$ (Eq. 4).

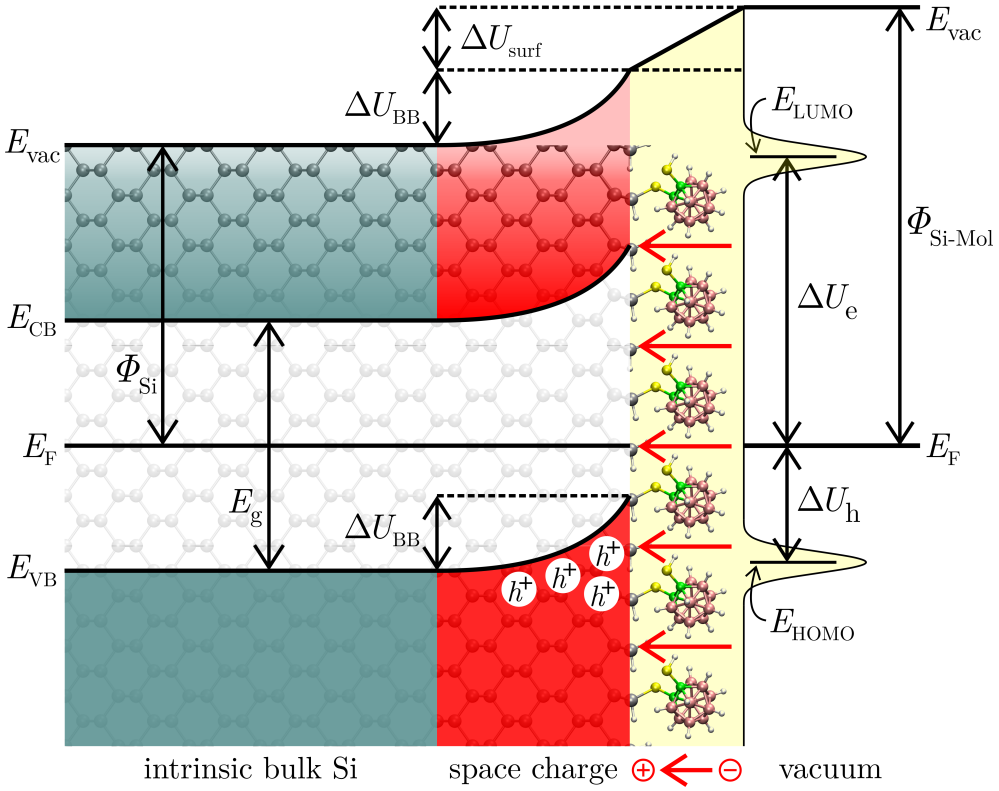

Figure 3: p-type STD of the silicon substrate. Energy diagram of the hydrogen-terminated mono-Si surface modified with electron-withdrawing molecules with μ_{Mol} pointed towards the surface. All labelled quantities and colour-coded cross-sectional regions are described in the main text. White circles with "h^+" labels mark accumulated holes.

iv Thesis aims and outline

In this thesis, we aim at a detailed theoretical description of physical and chemical properties of the gold-carboranedithiol and the silicon-carboranedithiol junctions. To fully characterise these issues, we also investigate the isolated subsystems, i.e. the bare gold and silicon substrates and the isolated carboranedithiol adsorbate, and the course of their mutual interaction leading to the junction formation.

We choose carborane-based adsorbates as mediators of electronic changes of the substrate surface for two main reasons. Firstly, from a purely physico-chemical point of view, they are thermally stable and chemically resistant cage-like molecules with a large intrinsic molecular dipole that can be directed either towards the surface or away from it. Secondly, the research of these cluster structures already has a long-lasting impact on the Czech academic field, thanks to the long-standing tradition of boron chemistry developed in Řež near Prague and the successful study of effects of adsorbed carborane monolayers on the surface work function of metal substrates using probe force microscopy methods [31–38].

We perform all theoretical studies using the SIESTA code based on a density functional theory (DFT) approach [39, 40]. Molecular monolayers grafted on the metal substrate via the sulphur anchoring groups are already a well-researched topic [16, 17, 31–34, 37, 38, 41–48]. Therefore, in this thesis, we take the study of the gold-carboranedithiol junctions only as a suitable training model in which our main goal is to verify the influence of the adsorbed molecular dipole layer on the electrostatic properties of the gold surface. We observe this influence as the change in the gold work function and fully characterise the various contributions [49]. Then, we move on to the topic of the SAMs of organothiols on the silicon substrate [50], the scope of which in current research is still negligible compared to the SAMs on the metal surfaces. Regarding the study of the silicon-carboranedithiol junctions, we survey the impact of the adsorbed dipole layer on the electrostatic surface properties of the silicon [51], similarly to the gold, and also on the band structure shifts inside the substrate. By means of these electronic changes, we provide a full description of the surface transfer doping and the work function change of the silicon wafer.

In the first chapter, we summarise the theoretical background of electronic-structure calculations. First, we describe the electron density as a fundamental property of a many-electron systems. Then, we introduce the functional of the spatially dependent electron density and the basic features of the DFT-based approach. Finally, we are interested in the SIESTA, i.e. both a method and a computer implementation transferring the fundamentals of DFT calculations to the field of solid state physics.

In the second chapter, we deal with the geometric and the electronic study of the bare gold and the bare silicon substrates and the isolated carboranedithiol adsorbate. A detailed description of these subsystems is a guide for us to assemble the substrate-adsorbate junctions.

In the third chapter, we study the formation and the physico-chemical properties gold-carboranedithiol junctions. In particular, we focus on the investigation of the formation of the gold-molecule interface and the influence of the carboranedithiol adsorbate on the electrostatic properties of the gold wafer. We divide the topic into two main sections, the first one dealing with the geometric study of various junction geometries and the second one focusing on the calculations of the electronic features of the most representative junction conformations. For us, the main goal of this chapter is to find the correct connection between the dipole moment of the molecule and the

change of the work function of the metal surface.

We present the most important results of this thesis in the fourth chapter where our main topic is the silicon-carboranedithiol junctions, representing the most comprehensive part of our research. First, we search for the most stable junction geometries with their full geometric description. Then, we subject the most stable conformations to further studies related to the examination of their electronic and mechanical features. Regarding electronic properties, we deal with the calculation of the charge density changes in the interface region and the electrostatic potential energy changes above the silicon surface (the first component of the silicon work function change), both caused by the carboranedithiol adsorption and the junction formation. In terms of mechanical properties, we observe the forces emerged between the molecule and the substrate upon the junction stretching and characterise the Si-S bond strength. We close this chapter a study of band characteristics of the substrate in the most stable conformations where we concern the carboranedithiol-mediated shifts of the silicon band structure. We directly relate these shifts to the band bending in the energy diagram of the silicon-molecule junction, giving us the second component of the silicon work function change.

1. Density functional theory

In this chapter, we give the basic principles of DFT as the first-principle approach of calculating the electronic structure of N-electron systems where the electron density is used as the fundamental variable. DFT is a variational method based on searching the electron density of the ground state, i.e. the state in which the system acquires the lowest possible total energy. When the ground-state density is reached, we gain access to all properties of the studied system. In this thesis, we employ SIESTA as the DFT implementation designed to perform electronic structure calculations for periodic systems such as solids, isolated molecules surrounded by a sufficient volume of vacuum, or substrate-molecule junctions. As for junctions, an essential part of the simulations is the study of electronic states of the molecules affected by the adsorption, especially the frontier molecular orbitals. In the presence of a semiconductor substrate at the interface, the band edges are also the subject of calculations. In such situations, DFT suffers from inherent errors in the interpretation of molecular resonance energies and fundamental band gaps [52], which affects the calculation of carrier injection barriers and interfacial charge transfers. Nevertheless, DFT describes these phenomena qualitatively and semi-quantitatively and provides an acceptable balance between accuracy and computational cost. Fpr these reasons, DFT remains the standard theoretical method for atomistic simulations of molecular interfaces and this motivates pur choice. For these reasons, DFT remains the standard theoretical method for atomistic simulations of molecular interfaces and this motivates our choice.

Throughout this chapter, all relationships and equations are expressed in Hartree atomic units for simplicity, i.e. the reduced Planck constant $\hbar$, the elementary charge e, the Bohr radius a_0, and the electron mass m_e, are set to 1.

1.1 Variational principle

In quantum mechanics, solving the Schrödinger equation is a standard mathematical issue. However, for systems with a huge number of electrons, such as molecules or solids, the equation is analytically unsolvable, so turning to approximate methods becomes a necessary step. One of these approximate ways is the variational method. Let us apply this method to the time-independent Schrödinger equation: $\mathcal{H}\,|\Psi\rangle = E_{\text{tot}}\,|\Psi\rangle$, where $\mathcal{H}$ is a Hermitian operator called the Hamiltonian, $|\Psi\rangle$ the wave-function representing a particular state of the system, and E_{tot} is the total energy of this system. The clue to the approximate solution is the variational principle, which states that the expectation value of the Hamiltonian, $\langle\Psi\,|\,\mathcal{H}\,|\,\Psi\rangle$, computed from the trial wave-function, $|\Psi\rangle$, is an upper bound to the true ground-state energy, E_0:

$$\langle\Psi\,|\,\mathcal{H}\,|\,\Psi\rangle = E_{\text{tot}}[\Psi] \geq E_0 = \langle\Psi_0\,|\,\mathcal{H}\,|\,\Psi_0\rangle\ , \tag{1.1}$$

where the wave-function is normalised: $\langle\Psi\,|\,\Psi\rangle = 1$. The path to the true ground-state wave-function, $|\Psi_0\rangle$, which gives rise to E_0, can be expressed via a minimisation procedure:

$$E_0 = \min_{\Psi\to N}\{E_{\text{tot}}[\Psi]\} = \min_{\Psi\to N}\left\{\left\langle\Psi\,\middle|\,\hat{T}_{\text{e}} + \hat{V}_{\text{ee}} + \hat{V}_{\text{en}}\,\middle|\,\Psi\right\rangle\right\}, \tag{1.2}$$

where $\hat{T}_{\text{e}}$, $\hat{V}_{\text{ee}}$, and $\hat{V}_{\text{en}}$, are the operators of the kinetic energy of electrons and the potential energies of Coulomb electron-electron repulsions and electron-nucleus attractions, respectively. The subscript $\Psi \to N$ indicates the searched Ψ is an allowed N-electron wave-function [53, 54].

1.2 Electron density

Supramolecular structures, polymers, condensed matter, and many others are today the main issue of modern methods of electronic-structure theory. As noted above, these many-electron systems cannot be solved analytically, making them suitable issues for the variational method. Furthermore, the situation can be greatly simplified by avoiding the complex direct search for the N-electron wave-function, concentrating on the electron density instead. The wave-function, $\Psi = \Psi(\{\mathbf{r}_i\})$[①], represents a particular state of N electrons that are distributed according to the set of respective positions $(\{\mathbf{r}_i\}) = (\mathbf{r}_1, \mathbf{r}_2, \ldots, \mathbf{r}_N)$ in 3-dimensional space, so $3N$ variables are needed for a complete description. However, the electron density, $\rho(\mathbf{r})$, depends only on 3 spatial coordinates, it is a physical observable, it can be probed (for example by scanning tunnelling microscopy), calculated and well visualised (typically in the form of density maps after X-ray diffraction experiments) [53, 54].

The system described by the normalised N-electron wave-function has the electron density:

$$\rho(\mathbf{r}) = N\int\cdots\int|\Psi(\mathbf{r},\mathbf{r}_2,\ldots,\mathbf{r}_N)|^2\,\mathrm{d}\mathbf{r}_2\cdots\mathrm{d}\mathbf{r}_N\,, \tag{1.3}$$

expressed here as the probability density distribution of finding *any* electron from the N-electron system within the infinitesimal volume element $\mathrm{d}\mathbf{r}$ while the positions of the other $N-1$ electrons are arbitrary. The multiplication factor N before the integral is due to electrons being indistinguishable. From this equation, several important properties emerge:

[①] The wave function is only electronic, i.e. it describes only the motion of electrons within the Born-Oppenheimer approximation.

- The electron density is the function of three spatial coordinates, it is non-negative: $\rho(\mathbf{r}) > 0$, and has the asymptote at zero at infinite distances: $\lim_{\mathbf{r}\to\infty} \rho(\mathbf{r}) = 0$.
- It integrates to the total number of electrons in the system:

$$\int \rho(\mathbf{r})\,\mathrm{d}\mathbf{r} = N\,. \tag{1.4}$$

- In the position of any α-th nucleus, $\mathbf{R}_\alpha$, the electron density distribution is discontinuous due to a singularity in the attractive potential energy as $\mathbf{r}_i \to \mathbf{R}_\alpha$. The resulting local maxima in the density distribution have "cusp" properties providing information on both the positions of the corresponding nuclei $\{\mathbf{R}_\alpha\}$ as well as their atomic numbers $\{Z_\alpha\}$.
- For long-range distances from all nuclei, the electron density shows an asymptotic exponential decay with the first ionisation potential energy, I_{min}, in the argument:

$$\rho(\mathbf{r}) \propto \exp\left[-2(2I_{\mathrm{min}})^{1/2}\,|\mathbf{r}|\right] \tag{1.5}$$

1.3 Functional of electron density

DFT builds its physical foundations on the properties of the ground state because, according to the Hohenberg–Kohn theorems [55], in this state, the total energy is a functional of the electron density. Furthermore, at the ground state, Eq. 1.3 can be reversed, meaning that knowledge of the true ground state $|\Psi_0\rangle$ implies knowledge of the true ground-state electron density, $\rho_0(\mathbf{r})$, and, *vice versa*, that knowledge of $\rho_0(\mathbf{r})$ implies knowledge of $|\Psi_0\rangle$. This means that $|\Psi_0\rangle$ is a unique functional of $\rho_0(\mathbf{r})$[②], i.e. $|\Psi_0\rangle = |\Psi[\rho_0]\rangle$ or $|\Psi_0\rangle = |\Psi[\rho_0(\mathbf{r})]\rangle$. Therefore, the dependence of E_0 on $\rho_0(\mathbf{r})$ follows:

$$E_0 = E_{\mathrm{tot}}[\rho_0] = \left\langle \Psi[\rho_0] \middle| \mathcal{H} \middle| \Psi[\rho_0] \right\rangle = T_{\mathrm{e}}[\rho_0] + V_{\mathrm{ee}}[\rho_0] + V_{\mathrm{en}}[\rho_0]. \tag{1.6}$$

where all three terms on the right-hand side are ground-state density functionals of the respective operators described in Eq. 1.2. Only the attraction term $V_{\mathrm{en}}[\rho_0]$ is an explicit functional of $\rho_0(\mathbf{r})$:

$$V_{\mathrm{en}}[\rho_0] = \left\langle \Psi[\rho_0] \middle| \hat{V}_{\mathrm{en}} \middle| \Psi[\rho_0] \right\rangle = \int \mathcal{V}_{\mathrm{en}}(\mathbf{r})\,\rho_0(\mathbf{r})\,\mathrm{d}\mathbf{r}\,. \tag{1.7}$$

Here, the integrand $\mathcal{V}_{\mathrm{en}}(\mathbf{r})$ is the "external"[③] potential due to charges of nuclei $\{Z_\alpha\}$ acting on any electron from the N-electron system within the infinitesimal volume element $\mathrm{d}\mathbf{r}$. The integral in Eq. 1.7 represents the electrostatic interaction between the external potential and the electron density of the ground state. The functional $V_{\mathrm{en}}[\rho_0]$ is the so-called system-dependent part of the energy $E_{\mathrm{tot}}[\rho_0]$, because it is determined not only by N electrons, but also by the external field composed of the positions and the charges of nuclei. The other two functionals $T_{\mathrm{e}}[\rho_0]$ and $V_{\mathrm{ee}}[\rho_0]$ do not depend on the external field, making them universal properties of the system.

The fundamental way leading to the true ground-state electron density is mediated by the variational principle for the density functional, which can be expressed as a two-step minimisation procedure:

[②] The wave-function depends on $\mathbf{r}$. However, the electron density also depends on $\mathbf{r}$, so the wave function depends on the electron density in all space.

[③] External means that the quantity does not come from the electrons themselves. This quantity reads: $\mathcal{V}_{\mathrm{en}}(\mathbf{r}) = -\sum_{\alpha=1}^{M} (Z_\alpha/|\mathbf{r} - \mathbf{R}_\alpha|)$.

$$E_0 = \min_{\rho \to N} \{E_{\text{tot}}[\rho]\} = \min_{\rho \to N} \left\{ \min_{\Psi \to \rho} \left[\left\langle \Psi \middle| \hat{T}_{\text{e}} + \hat{V}_{\text{ee}} \middle| \Psi \right\rangle \right] + \int \mathcal{V}_{\text{en}}(\mathbf{r})\, \rho(\mathbf{r})\, \mathrm{d}\mathbf{r} \right\}. \tag{1.8}$$

Here, the inner minimisation refers to the first step as the search over the subset of all wave-functions subject to the constraint of a particular density $\rho(\mathbf{r})$, which is specified by the subscript $\Psi \to \rho$. The result of this step is the wave-function delivering the lowest energy for the particular $\rho(\mathbf{r})$. The second step, expressed by the outer minimisation, release the constraint, extending the search over all densities with the aim to find $\rho_0(\mathbf{r})$. Here, the subscript $\rho \to N$ indicates the searched density comes from the allowed N-electron wave-function. When $\rho_0(\mathbf{r})$ is obtained, the corresponding lowest-energy wave-function is found through the first minimisation step. This wave-function is Ψ_0 and provides the lowest energy of all, i.e. E_0.

The first step of the variational principle does not concern the external potential energy $V_{\text{en}}[\rho_0]$ which depends explicitly on the density. Therefore, in Eq. 1.8, the inner minimisation term is shorter, introducing the so-called universal functional, $F[\rho]$, the unknown structure of which is the central issue of DFT-based methods.

1.4 Kohn-Sham density functional theory

DFT is often considered an *ab initio*[④] method as far as all quantum mechanical properties of electrons, i.e. exchange and correlation interactions, are described by density functionals arising from first-principles strategies (see Sec. 1.5). These strategies apply approximations to suitable theoretical models without using any adjustable parameters, i.e. properties scaled by e.g. experimentally measured quantities. Within the limitations of the approximations used, the electronic properties are completely determined by the geometry and the chemical nature of the constituents. In addition to its nature, the practical accuracy of DFT is also at the *ab initio* level.

Practically applicable DFT calculations employ the Kohn-Sham (KS) ansatz showing a hands-on way to deal with the unknown structure of the universal functional $F[\rho]$. Specifically, there is the idea the functional $F[\rho]$ can be divided into two main parts: the first simpler part composed of analytically solvable functionals, and the other more complex one including everything unknown that needs to be approximated [53, 54]. In that case, $F[\rho]$ consists of four terms:

$$F[\rho] = \underbrace{T_{\text{KS}}[\rho] + T_{\text{C}}[\rho]}_{= T_{\text{e}}[\rho]} + \underbrace{V_{\text{H}}[\rho] + V_{\text{ncl}}[\rho]}_{= V_{\text{ee}}[\rho]} = \underbrace{T_{\text{KS}}[\rho] + V_{\text{H}}[\rho]}_{\substack{\text{analytically} \\ \text{solvable}}} + \underbrace{T_{\text{C}}[\rho] + V_{\text{ncl}}[\rho]}_{\text{unknown}} \tag{1.9}$$

where the density functionals on the right-hand side describe the kinetic energy of non-interacting Kohn-Sham electrons, $T_{\text{KS}}[\rho]$, the residual part of the total kinetic energy, $T_{\text{C}}[\rho]$, the Hartree potential energy of the classical Coulomb repulsion, and the potential energy of the non-classical exchange-correlation contribution to the electron-electron interactions, $V_{\text{ncl}}[\rho]$. All these quantities are described below.

Kinetic-energy functional. The separation of $T_{\text{e}}[\rho]$ into the known $T_{\text{KS}}[\rho]$ and the unknown $T_{\text{C}}[\rho]$ stems from the KS concept of the non-interacting reference system

[④] The methods are based on reliable physical foundations and solve the Schrödinger equation using a hierarchy of variously clever approximations without additional experimental or adjustable parameters. One only needs to know the fundamental physical constants in advance.

where each non-interacting electron moves independently of the others in the effective potential, $\mathcal{V}_{\text{eff}}(\mathbf{r})$, of nuclei and other electrons. Therefore, electron correlations are thereby neglected and the reference system is described only by a normalised single-determinant wave-function, $\mathcal{D}$, composed of a set of orthonormal orbitals, $\{\psi_i\}$.

The Kohn-Sham strategy is interested in a direct connection between this non-interacting artificial system and the interacting real one, namely by means of an appropriate choice of the effective potential $\mathcal{V}_{\text{eff}}(\mathbf{r})$. One denotes this appropriate field as the KS potential, $\mathcal{V}_{\text{KS}}(\mathbf{r})$, in which the corresponding non-interacting KS density, $\rho_{\text{KS}}(\mathbf{r})$, is identical to the ground-state electron density of the real interacting system. Through a simple probability-density formula:

$$\rho_{\text{KS}}(\mathbf{r}) = \sum_{i=1}^{N} \left|\psi_i^{\text{KS}}(\mathbf{r})\right|^2 = \rho_0(\mathbf{r})\,, \tag{1.10}$$

one sees the real density $\rho_0(\mathbf{r})$ is provided by the set of KS orbitals, $\{\psi_i^{\text{KS}}\}$, i.e. the set from which the KS-based single-determinant wave-function, $\mathcal{D}_{\text{KS}}$ $(= \mathcal{D}[\rho_0])$, is composed. In this basis, the ground-state kinetic energy, $T_{\text{KS}}[\rho_0]$, reads:

$$T_{\text{KS}}[\rho_0] = \left\langle \mathcal{D}_{\text{KS}} \middle| \hat{T}_{\text{e}} \middle| \mathcal{D}_{\text{KS}} \right\rangle = -\frac{1}{2}\sum_{i=1}^{N} \left\langle \psi_i^{\text{KS}} \middle| \left(\nabla_i\right)^2 \middle| \psi_i^{\text{KS}} \right\rangle \tag{1.11}$$

where ∇_i denotes the vector gradient operator acting on the components of $\mathbf{r}_i$ of the i-th electron.

The residual kinetic energy $T_{\text{C}}[\rho]$ is positive and poses only the minor portion of $T_{\text{e}}[\rho]$; therefore $T_{\text{KS}}[\rho] \leq T_{\text{e}}[\rho]$.

Potential-energy functional. Just like the kinetic energy, the two-electron functional $V_{\text{ee}}[\rho]$ can also be divided into the known $V_{\text{H}}[\rho]$ and the unknown $V_{\text{ncl}}[\rho]$. In the wave-function-free expression, the electron-repulsion functional $V_{\text{ee}}[\rho]$ reads:

$$V_{\text{ee}}[\rho] = \underbrace{\frac{1}{2}\iint \frac{\rho(\mathbf{r})\rho(\mathbf{r}')}{|\mathbf{r}-\mathbf{r}'|}\,\mathrm{d}\mathbf{r}\,\mathrm{d}\mathbf{r}'}_{=V_{\text{H}}[\rho]} + \underbrace{\frac{1}{2}\iint \frac{\rho(\mathbf{r})\rho_{\text{XC}}(\mathbf{r},\mathbf{r}')}{|\mathbf{r}-\mathbf{r}'|}\,\mathrm{d}\mathbf{r}\,\mathrm{d}\mathbf{r}'}_{=V_{\text{ncl}}[\rho]} \tag{1.12}$$

where the factor $1/2$ enters to prevent double counting. The first classical term $V_{\text{H}}[\rho]$ is the functional of the single-particle density, i.e. $\rho(\mathbf{r})$, resulting in the involvement of the uncorrelated interaction of each electron with the whole electron density, including its own density[5]. This non-physical self-interaction is corrected by means of the second non-classical term $V_{\text{ncl}}[\rho]$. In particular, $V_{\text{ncl}}[\rho]$ describes the interaction between the single-particle density $\rho(\mathbf{r})$ and the exchange-correlation hole, $\rho_{\text{XC}}(\mathbf{r},\mathbf{r}')$, as the physical quantity describing the reduction of the electron density at $\mathbf{r}'$ caused by the presence of an electron at $\mathbf{r}$. The exact hole includes the potential-energy contributions of electron exchange (arising from the antisymmetry of the wave-function) and electron correlations, and also the self-interaction corrections, making this quantity the real correction for the completely uncorrelated mutual repulsions of the single-particle density distributions. Eq. 1.12 can be written in a shorter form, namely in terms of the electron-pair density: $\rho_2(\mathbf{r},\mathbf{r}') = \rho(\mathbf{r})\rho(\mathbf{r}') + \rho(\mathbf{r})\rho_{\text{XC}}(\mathbf{r},\mathbf{r}')$.

1.4.1 Kohn-Sham equations

Within the KS-DFT approach, all unknown functionals are incorporated into the exchange-correlation energy: $E_{\text{XC}}[\rho] = T_{\text{C}}[\rho] + V_{\text{ncl}}[\rho]$. Therefore, the total energy

[5] However, most of this quantity involves the (correct) repulsion of one electron with another electron.

reads: $E_{\text{tot}}[\rho] = T_{\text{KS}}[\rho] + V_{\text{H}}[\rho] + E_{\text{XC}}[\rho] + V_{\text{en}}[\rho]$, and its minimum is the true ground-state energy E_0. Finding this minimum is associated with finding the KS potential and the set of KS orbitals giving rise to the true ground-state electron density. To reveal these properties, the method of Lagrange undetermined multipliers is used. In particular, the minimisation (or the extremalisation) of the functional $E_{\text{tot}}[\rho]$ is subject to the constraint: $\int \rho(\mathbf{r})\,\mathrm{d}\mathbf{r} = N$, and one constructs the unconstrained functional $\mathcal{L}[\{\psi_i\},\{\varepsilon_{ij}\}]$, i.e. the functional of the set of orthonormal orbitals $\{\psi_i\}$ and the set of Lagrange multipliers $\{\varepsilon_{ij}\}$:

$$\mathcal{L}[\{\psi_i\},\{\varepsilon_{ij}\}] = E_{\text{tot}}[\rho] - \sum_{i=1}^{N}\sum_{j=1}^{N}\varepsilon_{ij}\left(\int \psi_i^*(\mathbf{r})\psi_j(\mathbf{r})\,\mathrm{d}\mathbf{r} - N\right) \tag{1.13}$$

where $\rho(\mathbf{r}) = \sum_{i=1}^{N}|\psi_i(\mathbf{r})|^2$ is taken into account.

Now, one looks for the set of orbitals that minimises the unconstrained functional, i.e. that gives the first variation in $\mathcal{L}$ equal to zero: $\delta\mathcal{L} = 0$. Specifically, one is interested in such stationary conditions, where the functional derivative of $\mathcal{L}$ with respect to ψ_i^* is zero: $(\delta\mathcal{L}/\delta\psi_i^*) = 0$. Assuming the set of Lagrange multipliers forms a Hermitian matrix ($\varepsilon_{ij} = \varepsilon_{ji}^*$) that can be converted to a diagonal form, one gets the system of Kohn-Sham one-electron equations:

$$\Bigg(-\frac{1}{2}(\nabla_i)^2 + \underbrace{\overbrace{\int \frac{\rho(\mathbf{r}')}{|\mathbf{r}-\mathbf{r}'|}\,\mathrm{d}\mathbf{r}'}^{=\mathcal{V}_{\text{H}}(\mathbf{r})} + \overbrace{\frac{\delta E_{\text{XC}}[\rho]}{\delta\rho(\mathbf{r})}}^{=\mathcal{V}_{\text{XC}}(\mathbf{r})} + \mathcal{V}_{\text{en}}(\mathbf{r})}_{=\mathcal{V}_{\text{eff}}(\mathbf{r})}\Bigg)\psi_i(\mathbf{r}) = \varepsilon_i\psi_i(\mathbf{r}) \qquad i = 1,\ldots,N$$

where ε_i is the orbital energy, $\mathcal{V}_{\text{H}}(\mathbf{r})$ the Hartree potential, and $\mathcal{V}_{\text{XC}}(\mathbf{r})$ is the exchange-correlation potential. These two potentials together with the external term $\mathcal{V}_{\text{en}}(\mathbf{r})$ give rise to the total effective potential $\mathcal{V}_{\text{eff}}(\mathbf{r})$, i.e. the mean field surrounding the i-th independent electron. Through this potential, all these one-electron equations are mutually coupled and therefore have to be solved iteratively.

If one knew the exact form of the functional, solving the KS equations would lead to finding the set of KS orbitals that would give rise to the ground-state electron density of the real interacting system (see Eq. 1.10). In this case, $\mathcal{V}_{\text{eff}}(\mathbf{r})$ corresponds to $\mathcal{V}_{\text{KS}}(\mathbf{r})$ and the system of KS equations read:

$$\left(-\frac{1}{2}(\nabla_i)^2 + \mathcal{V}_{\text{KS}}(\mathbf{r})\right)\psi_i^{\text{KS}}(\mathbf{r}) = \hat{h}_i\psi_i^{\text{KS}}(\mathbf{r}) = \varepsilon_i^{\text{KS}}\psi_i^{\text{KS}}(\mathbf{r}) \qquad i = 1,\ldots,N \tag{1.14}$$

where $\hat{h}_i$ is the Kohn-Sham one-electron operator for the i-th electron; $\varepsilon_i^{\text{KS}}$ is the eigenvalue of this one-electron operator and represent the KS orbital energy of the i-th occupied state.

If one knew the exact $E_{\text{XC}}[\rho]$, the Kohn-Sham approach would essentially be the strategy for obtaining the true ground-state electron density. Unfortunately, the explicit forms of $E_{\text{XC}}[\rho]$ or $\mathcal{V}_{\text{XC}}(\mathbf{r})$ are unknown, leading to necessary approximations of these quantities.

1.5 Exchange-correlation functionals

In this thesis, we employ approximate forms of $E_{\text{XC}}[\rho]$ obtained by first principles applied to suitable theoretical models. One can start with the general form of the

exact $E_{\mathrm{XC}}[\rho]$ that can be expressed in terms of the exchange-correlation energy per particle, $\varepsilon_{\mathrm{XC}}(\mathbf{r})$:

$$E_{\mathrm{XC}}[\rho] = \int \rho(\mathbf{r})\, \varepsilon_{\mathrm{XC}}(\mathbf{r})\, \mathrm{d}\mathbf{r} \tag{1.15}$$

where one assumes $\varepsilon_{\mathrm{XC}}(\mathbf{r})$ to be a function of $\mathbf{r}$. In other words, $\varepsilon_{\mathrm{XC}}(\mathbf{r})$ depends on the electron density in all space and is therefore the functional of the electron density, i.e. $\varepsilon_{\mathrm{XC}}(\mathbf{r}) = \varepsilon_{\mathrm{XC}}[\rho(\mathbf{r})]$. The approximation strategies of the exact $E_{\mathrm{XC}}[\rho]$ aim at this one-particle quantity, while certain physical features of the exact functional have to be preserved, typically the sum rules of the exchange-correlation hole[6].

There are several different types of $E_{\mathrm{XC}}[\rho]$ that differ in the degree of accuracy, computational demands and their specialisation on a particular issue. In this section, we briefly discuss three fundamental types of functionals that are important for our calculations: local-density approximation (LDA)[56, 57]; generalised-gradient approximation (GGA)[58–60]; and van dar Waals density functional (vdW-DF)[61–64]. For interested readers, a detailed description of other exchange-correlation functionals can be found in Koch and Holthausen [54].

1.5.1 Local-density approximation

The LDA is a starting point for all approximated functionals. It stems from a model of the uniform electron gas (also known as the jellium) in which interacting electrons give rise to the electron density throughout the space that is in balance with a uniformly distributed positive charge in the background. The jellium model provides analytically solvable calculations and accurate simulations, making the model very useful in the DFT framework.

From a mathematical point of view, the LDA-based strategy replaces the functional $\varepsilon_{\mathrm{XC}}[\rho(\mathbf{r})]$ by the local function of the electron density:

$$\varepsilon_{\mathrm{XC}}(\mathbf{r}) = \varepsilon_{\mathrm{XC}}[\rho(\mathbf{r})] \xrightarrow{\mathrm{LDA}} \varepsilon_{\mathrm{XC}}^{\mathrm{LDA}}(\rho(\mathbf{r}))\,. \tag{1.16}$$

where on the right-hand side, $\varepsilon_{\mathrm{XC}}^{\mathrm{LDA}}(\rho(\mathbf{r}))$ represents the exchange-correlation energy per particle of the uniform electron gas of density $\rho(\mathbf{r})$. The quantity $\varepsilon_{\mathrm{XC}}^{\mathrm{LDA}}(\rho(\mathbf{r}))$ depends on the density locally, i.e. its value is determined by $\rho(\mathbf{r})$ just at $\mathbf{r}$, regardless of the rest of the electron density distribution. In particular, the LDA neglects $T_{\mathrm{C}}[\rho]$, so it only concerns the non-classical term $V_{\mathrm{ncl}}[\rho]$:

$$\frac{1}{2}\int \frac{\rho_{\mathrm{XC}}(\mathbf{r},\mathbf{r}')}{|\mathbf{r}-\mathbf{r}'|}\,\mathrm{d}\mathbf{r}' \xrightarrow{\mathrm{LDA}} \varepsilon_{\mathrm{XC}}^{\mathrm{LDA}}(\rho(\mathbf{r}))\,. \tag{1.17}$$

The approximated one-particle energy gives rise to the LDA-based energy $E_{\mathrm{XC}}[\rho]$:

$$E_{\mathrm{XC}}^{\mathrm{LDA}}[\rho] = \int \rho(\mathbf{r})\, \varepsilon_{\mathrm{XC}}^{\mathrm{LDA}}(\rho(\mathbf{r}))\, \mathrm{d}\mathbf{r}\,. \tag{1.18}$$

In practice, one divides all space into infinitesimal volume elements $\mathrm{d}\mathbf{r}$. In the middle of each element, one finds the value of $\rho(\mathbf{r})$ which is then substituted into the relation for $\varepsilon_{\mathrm{XC}}^{\mathrm{LDA}}(\rho(\mathbf{r}))$ valid for the jellium (see below). This gives the energy in the particular element $\mathrm{d}\mathbf{r}$ and the total energy $E_{\mathrm{XC}}^{\mathrm{LDA}}[\rho]$ is obtained by the sum over all elements.

[6] The physically meaningful hole $\rho_{\mathrm{XC}}(\mathbf{r},\mathbf{r}')$ has to satisfy the normalisation condition: $\int \rho_{\mathrm{XC}}(\mathbf{r},\mathbf{r}')\,\mathrm{d}\mathbf{r}' = -1$, making the hole intended for exactly one electron. Moreover, the exchange part has to fulfil the condition of non-positivity everywhere because of the Pauli exclusion principle. The correlation part only modifies the shape of the hole; the normalisation condition stems from the exchange part only. All these properties are collectively referred to as the sum rules.

To express the specific form of $\varepsilon_{\mathrm{XC}}^{\mathrm{LDA}}(\rho(\mathbf{r}))$, one splits this quantity into the exchange, $\varepsilon_{\mathrm{X}}^{\mathrm{LDA}}(\rho(\mathbf{r}))$, and the correlation part, $\varepsilon_{\mathrm{C}}^{\mathrm{LDA}}(\rho(\mathbf{r}))$:

$$\varepsilon_{\mathrm{XC}}^{\mathrm{LDA}}(\rho(\mathbf{r})) = \varepsilon_{\mathrm{X}}^{\mathrm{LDA}}(\rho(\mathbf{r})) + \varepsilon_{\mathrm{C}}^{\mathrm{LDA}}(\rho(\mathbf{r})) \tag{1.19}$$

Within the jellium model, the exchange part is given analytically [53, 54], while the correlation part takes an explicit form only at the low- or the high-density limits. However, there are very accurate numerical expressions of the correlation part encompassing both of these extremes and are obtained by means of sophisticated interpolation schemes applied to very accurate data from stochastic simulations of the jellium [65].

The LDA-based functionals are widely used for solid states, condensed systems with homogeneous electron density, homogeneous materials with delocalised electrons, etc.

1.5.2 Generalised-gradient approximation

In many cases where inhomogeneities in the density distribution are to be expected, it is necessary to proceed beyond the LDA framework. The most straightforward step in this direction, originally proposed by Kohn and Sham [66], is the introduction of the local density gradient, $\nabla\rho(\mathbf{r})$, by means of the gradient expansion of the density just at $\mathbf{r}$. This delivers $E_{\mathrm{XC}}[\rho]$ as the series of increasingly higher even-order density gradient terms. In practice, however, this straightforward step does not lead to any consistent improvement over the LDA as it violates the sum rules for the exchange-correlation hole (see Fn. ⑥), leading to the divergence of the exchange potential in a vacuum where the electron density decays exponentially.

Therefore, one has to impose necessary constraints to preserve the required sum rules even for the holes of the beyond-LDA functionals. There is the first-principles procedure, largely proposed by Perdew [67], which leads to the GGA-based functionals, the mainstream of modern DFT calculations in condensed matter physics research. The general form of the GGA reads:

$$E_{\mathrm{XC}}^{\mathrm{GGA}}[\rho] = \int f(\rho(\mathbf{r}), \nabla\rho(\mathbf{r}))\,\mathrm{d}\mathbf{r} \tag{1.20}$$

where the integrand $f = f(\rho(\mathbf{r}), \nabla\rho(\mathbf{r}))$ is the semi-local⑦ function chosen by a certain set of criteria. The most common structure of $f(\rho(\mathbf{r}), \nabla\rho(\mathbf{r}))$ is constructed by a first-principles strategy where only the rules of quantum mechanics and special constraining conditions are used to numerically determine all the parameters in $E_{\mathrm{XC}}^{\mathrm{GGA}}[\rho]$. Among such types of functionals, the most popular implementation has been proposed by Perdew, Burke, and Ernzerhof [59], referred to as PBE. The relatively simple structure of the PBE-GGA functional ensures its applicability to both molecules and solids.

1.5.3 van der Waals density functional

The van der Waals (vdW) dispersion forces arise from non-local dispersion correlations [68] and represent attractive interactions⑧ between separate regions in space that exhibit some ability to polarise. This is a common phenomenon where the electron density is not uniform, e.g. biomolecules, soft matter, solid-molecule interface, etc. To cover vdW forces within the DFT framework, one has to introduce the non-local correlation functional, $E_{\mathrm{C}}^{\mathrm{nl}}[\rho]$. This gives rise to the vdW-DF functional, denoted as $E_{\mathrm{XC}}^{\mathrm{vdW}}[\rho]$, composed of the local/semi-local exchange-correlation part and the non-local correlation part:

⑦ The quantity is semi-local as it depends on the local value and on the local gradient of the density.

⑧ At short distances, it has a repulsive part.

$$E_{\mathrm{XC}}^{\mathrm{VDW}}[\rho] = E_{\mathrm{XC}}^{0}[\rho] + E_{\mathrm{C}}^{\mathrm{nl}}[\rho]\,. \tag{1.21}$$

Here, $E_{\mathrm{XC}}^{0}[\rho]$ is the reference energy representing the regular portion of the vdW-DF functional within the local/semi-local framework. The regular part serves as a foundation for the construction of $E_{\mathrm{C}}^{\mathrm{nl}}[\rho]$, so it is important to express both of them in one quantity. The long-range exchange effects are negligible due to the asymptotic exponential decay of the density (see Eq. 1.5). In this thesis, we employ the vdW-DF functional developed by Dion et al. [64]. See App. A and B for more details.

1.6 SIESTA

The SIESTA (Spanish Initiative for Electronic Simulations with Thousands of Atoms) implementation efficiently performs standard self-consistent KS-DFT calculations of molecules and solids [39, 40]. All nuclei and electrons of a given system are introduced into the parallelepiped-shaped unit cell that, by means of the appropriately chosen periodic boundary conditions (PBCs), is periodically repeated in all three lattice vectors in order to assemble the final super-cell. The super-cell approach can also be applied to non-periodic structures when a sufficient amount of vacuum is included in the unit cell to effectively separate the images. In this way, slabs, wires, or molecules are studied by introducing vacuum in one, two, or three directions, respectively.

Basis sets. Each searched valence KS orbital $\psi_i(\mathbf{r})$ corresponds to a linear combination of basis functions, $\phi_\nu(\mathbf{r})$, of known properties:

$$\psi_i(\mathbf{r}) = \sum_{\nu=1} C_{\nu i}\phi_\nu(\mathbf{r}) \tag{1.22}$$

where $C_{\nu i} = \langle\phi_\nu|\psi_i\rangle$. The orbital $\psi_i(\mathbf{r})$ is exact as far as the basis set $\{\phi_\nu\}$ is complete. In practical calculations, including DFT-SIESTA, the expansion is truncated to a finite number of terms, making the final $\psi_i(\mathbf{r})$ approximated. In addition, the finite basis set is non-orthogonal and the individual members of the expansion thus give rise to the overlap matrix: $S_{\mu\nu} = \langle\phi_\mu|\phi_\nu\rangle$. The KS one-electron operator in this basis forms the Hamiltonian matrix: $H_{i,\mu\nu} = \langle\phi_\mu|\hat{h}_i|\phi_\nu\rangle$, making each KS one-electron equation in Eq. 1.14 a generalised eigenvalue problem:

$$\sum_{\nu=1} H_{i,\mu\nu}C_{\nu i} = \varepsilon_i^{\mathrm{KS}} \sum_{\nu=1} S_{\mu\nu}C_{\nu i}\,, \tag{1.23}$$

Each basis function in $\{\phi_\nu\}$ is expressed in terms of localised atomic-like orbital, i.e. $\{\phi_\nu\} \equiv \{\phi_{\alpha,nlm}\}$, where each $\phi_{\alpha,nlm}(\mathbf{r})$ is centred on the specific atom α and constructed as the product of a numerical radial function, $\mathcal{R}_{\alpha,nl}(|\mathbf{r}_\alpha|)$, and a spherical harmonic, $Y_{lm}(\hat{\mathbf{r}}_\alpha)$, which depend on the magnitude of the electron-nucleus distance: $|\mathbf{r}_\alpha| = |\mathbf{r} - \mathbf{R}_\alpha|$ and the corresponding unit vector: $\hat{\mathbf{r}}_\alpha = \mathbf{r}_\alpha/|\mathbf{r}_\alpha|$, respectively. The radial part of $\phi_{\alpha,nlm}(\mathbf{r})$ is confined by a cutoff radius, r_{C}, beyond which it is set to zero and thus does not extend to the vacuum. The use of localised orbitals possessing a certain r_{C} has important consequences for the numerical evaluation of the Hamiltonian. Specifically, if two atoms (labelled e.g. as 1 and 2) are separated from each other by more than $r_{\mathrm{C},1} + r_{\mathrm{C},2}$, their mutual interaction will be zero because there is no overlap between the orbitals of these atoms. This makes the Hamiltonian and the overlap matrices sparse, where many of the elements are zero. Therefore, one can use numerical techniques for sparse matrices which are very efficient. As for spherical harmonics, they are well-defined orthogonal functions of angular momenta denoted by l and m determining the

shape and the spatial orientation of $\phi_{\alpha,nlm}(\mathbf{r})$, respectively. Numerical radial functions represent a certain degree of freedom that we can play with and come from the valence shell, i.e. the highest energy level occupied by an electron specified by the highest principal quantum number, denoted by n, and the values of $l = 0, \ldots, n-1$.

In the most common cases, each valence atomic orbital is described by either one or two basis functions and the corresponding basis set is thereby classified as the single-ζ (SZ) or the double-ζ (DZ), respectively. For example, when describing atomic species of the second ($n = 2$) or the third periods ($n = 3$), the SZ basis set is constructed from a single s-orbital ($l = 0$; $m = 0$) and three p-orbitals ($l = 1$; $m = -1, 0, 1$), while in the DZ case, each orbital is described by two basis functions. To increase the flexibility, it is usual to extend these kinds of basis sets with additional polarisation[9] functions, leading to the single-ζ plus polarisation (SZP) and the double-ζ plus polarisation (DZP) types. For $n = 2$ or 3, there are five polarisation d-orbitals ($l = 2$; $m = -2, -1, 0, 1, 2$). In this thesis, we employ the SZP and the DZP basis sets for the substrate (gold or silicon) and the molecular atoms (boron, carbon, sulphur, and hydrogen), respectively.

Pseudo-potentials. In solid state physics, there is a common practice in which the description of core electrons, i.e. electrons of inner shells tightly bound to the nucleus, is approximated by an effective potential, or pseudo-potential. Specifically, valence electrons representing the part of the electronic structure responsible for creating chemical bonds and determining material properties are explicitly included in the system, while core electrons are included indirectly - in the pseudo-potential for valence electrons. In addition, pseudo-potentials eliminate the complex curvatures of the radial course of atomic orbitals in the core region and thus significantly reduce the computational cost of the simulation.

Fig. 1.1 shows the pseudo-potential method for the Si atom acting on the valence $3p$ orbital. In each panel, the vertical dashed line defines the l-dependent core radius, r^l_{core}, for $l = 1$. In the left panel, the solid curve plots the course of the valence atomic orbital, ϕ^l_v, for $l = 1$, encompassing the contributions of all the electrons in the atom. Its nodes inside the atom-centred sphere of radius $r < r^l_{\text{core}}$ are replaced by the smooth, nodeless valence pseudo-orbital, $\widetilde{\phi}^l_v$, depicted by the dashed curve. The all-electron valence atomic orbital satisfies the equation: $\hat{h}\,|\phi^l_v\rangle = \varepsilon^l_v\,|\phi^l_v\rangle$, where ε^l_v is its corresponding eigenenergy. Expressing the pseudo-orbital in terms of the all-electron orbital via the linear combination of core states: $|\widetilde{\phi}^l_v\rangle = |\phi^l_v\rangle + \sum_c a^l_{cv}\,|\phi^l_c\rangle$, where $a^l_{cv} = \langle\phi^l_c|\widetilde{\phi}^l_v\rangle \neq 0$, and applying $\hat{h}$ onto this expression, one gets:

$$\left[\hat{h} + \sum_c \left(\varepsilon^l_v - \varepsilon^l_c\right)|\phi^l_c\rangle\langle\phi^l_c|\right]|\widetilde{\phi}^l_v\rangle = \hat{h}^l_{\text{PS}}\,|\widetilde{\phi}^l_v\rangle = \varepsilon^l_v\,|\widetilde{\phi}^l_v\rangle\ . \tag{1.24}$$

Here, the indices α and n labelling the nucleus and the electron shell, respectively, are omitted for simplicity. On the left-hand side, the second term in the square bracket is the additional repulsive potential, $\mathcal{V}^l_{\text{rep}}(r)$, which partially screens the attractive effect of the all-electron potential: $-Z/r$ (Fig. 1.1, black curve), between the electron and the nucleus, leading to the associated pseudo-potential: $\mathcal{V}^l_{\text{PS}}(r) = -(Z/r) + \mathcal{V}^l_{\text{rep}}(r)$, of the l-th angular momentum. In the right panel of Fig. 1.1, with a decreasing electron-nucleus distance, there is an increasing difference between the all-electron potential and the pseudo-potential as the core radius is crossed.

The general form of the l-dependent pseudo-potential is: $\hat{V}_{\text{PS}}(\mathbf{r}) = \sum_{l=0}^{\infty}\mathcal{V}^l_{\text{PS}}(r)\,\hat{P}_l$, where $\hat{P}_l = \sum_{m=-l}^{+l}|Y_{lm}\rangle\langle Y_{lm}|$ is the projection onto the l-th angular momentum. The operator $\hat{V}_{\text{PS}}(\mathbf{r})$ is local in the radial coordinates via the local term $\mathcal{V}^l_{\text{PS}}(r)$ but non-

[9] The polarisation function has a higher l than the highest l in the ground state of the atom.

local in the angular coordinates via the non-local term $|Y_{lm}(\hat{\mathbf{r}})\rangle\langle Y_{lm}(\hat{\mathbf{r}}')|$. In practice, only the core states with low-angular momenta up to $l_{\max}$ are occupied. Therefore, for values of $l > l_{\max}$, the corresponding l-components of the orbitals feel the ionic core in the same way, leading to the pseudo-potential $\hat{V}_{\rm PS}(\mathbf{r})$ of the semi-local nature:

$$\hat{V}_{\rm PS}(\mathbf{r}) = \mathcal{V}_{\rm PS}^{\rm loc}(r)\sum_{l=0}^{\infty}\hat{P}_l + \sum_{l=0}^{l_{\max}}\sum_{m=-l}^{+l}|Y_{lm}\rangle\,\delta\mathcal{V}_{\rm PS}^{l}(r)\,\langle Y_{lm}| \tag{1.25}$$

where $\mathcal{V}_{\rm PS}^{\rm loc}(r)$ is the average local pseudo-potential of the non-core angular momenta ($l > l_{\max}$) and describes the long-range effects of the unscreened potential: $-Z/r$, out of the core region, i.e. at the distance of $r \geq r_{\rm core}^{l}$; the other difference term, $\delta\mathcal{V}_{\rm PS}^{l} = \mathcal{V}_{\rm PS}^{l} - \mathcal{V}_{\rm PS}^{\rm loc}$, is the short-range part of the local $\mathcal{V}_{\rm PS}^{l}(r)$, it depends on l and vanishes at $r \geq r_{\rm core}^{l}$.

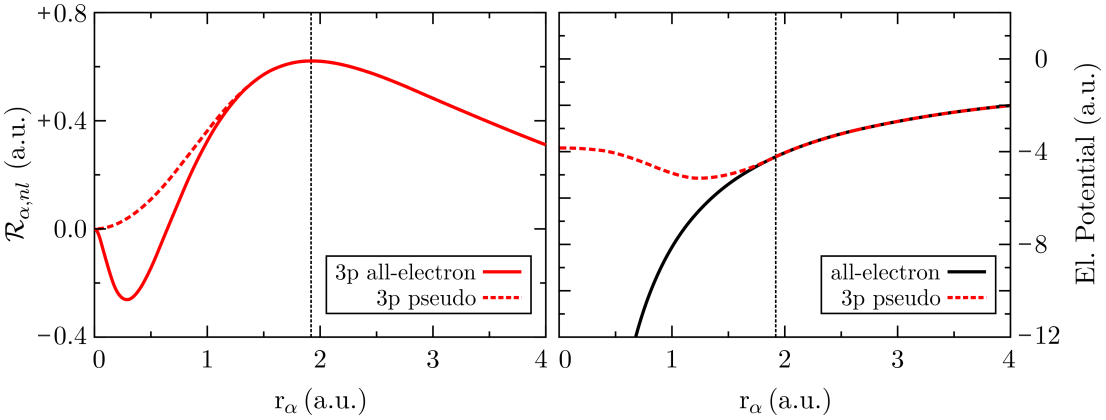

Figure 1.1: Pseudo-potential method applied to Si atom. In the left panel, the red solid line depict the dependence of the radial part of the all-electron valence atomic orbital with $l = 1$ ($3p$) on the electron-nucleus distance. In the right panel, the black curve corresponds to the all-electron potential: $-Z/r$. In both panels, the red dashed lines depict the atomic pseudo-orbital and the atomic pseudo-potential, and the vertical dashed lines picture the core radius $r_{\rm core}$ for $l = 1$. In the left panel, the pseudo-orbital in the core region ($r_\alpha < r_{\rm core}$) is node-less, making the oscillations completely damped.

The second term in Eq. 1.25 is computationally demanding as it provides three-centre integrals. However, there is a strategy developed by Kleinman and Bylander (KB) [69] replacing the local term $\delta\mathcal{V}_{\rm PS}^{l}(r)$ with the non-local quantity that is separable in the radial coordinates: $\delta\mathcal{V}_{\rm KB}^{l}(r,r') = f_l(r)f_l^*(r')$, making the second term in Eq. 1.25 fully non-local. Specifically, the KB-based projection operator reads:

$$\delta\hat{V}_{\rm KB}^{l} = \sum_{m=-l}^{+l}\frac{\left|\delta\hat{V}_{\rm PS}^{l}\,\phi_{\rm PS}^{lm}\right\rangle\left\langle\phi_{\rm PS}^{lm}\,\delta\hat{V}_{\rm PS}^{l}\right|}{\left\langle\phi_{\rm PS}^{lm}\left|\delta\hat{V}_{\rm PS}^{l}\right|\phi_{\rm PS}^{lm}\right\rangle} \tag{1.26}$$

where $\psi_{\rm PS}^{lm}$ is the reference pseudo-orbital obtained from the reference calculation of the isolated-atom configuration in the norm-conserving pseudo-potential.

The general pseudo-potential belonging to the α-th atom is: $\hat{V}_{\rm PS}^{\alpha}(\mathbf{r}) = \hat{V}_{\rm loc}^{\alpha}(\mathbf{r}) + \hat{V}_{\rm KB}^{\alpha}(\mathbf{r})$, where $\hat{V}_{\rm loc}^{\alpha}(\mathbf{r})$ and $\hat{V}_{\rm KB}^{\alpha}(\mathbf{r})$ are the local long-range part and the non-local short-range part, respectively. Thus, one gets the final Kohn-Sham one-electron operator:

$$\hat{h} = -\frac{1}{2}\nabla^2 + \sum_{\alpha}\hat{V}_{\rm loc}^{\alpha}(\mathbf{r}) + \sum_{\alpha}\hat{V}_{\rm KB}^{\alpha}(\mathbf{r}) + \mathcal{V}_{\rm H}(\mathbf{r}) + \mathcal{V}_{\rm XC}(\mathbf{r}) \tag{1.27}$$

where the pseudo-potential terms replace the external potential $\mathcal{V}_{\rm en}(\mathbf{r})$.

2. Isolated subsystems

In this chapter, we provide a basic characterisation of the gold and the silicon substrates and the isolated carboranedithiol adsorbates. Through three sections, we create a complete geometric description of all the mentioned isolated subsystems in the state before they become the parts of the respective substrate-adsorbate junctions, representing the main subjects of the third and the fourth chapters.

2.1 Gold

Gold is one of the most noble metals in the world, has a yellow colour and is very rare in nature. Its content in the Earth's crust is in the order of 10^{-7} %. From a chemical point of view, gold is an extraordinarily resistant metal. It is insoluble in common mineral acids (with the exception of aqua regia) and reluctantly reacts with oxygen, making its surface resistant to corrosion. However, it shows a great willingness to form a strong covalent bond with sulphur [70] with a strength close to that of the Au-Au bond [47, 71, 72].

In this section, we go through the geometric properties of crystal structure of gold. We divide the section into three parts. In the first two parts, we investigate the bulk structure of gold and its lattice parameters. Then, we proceed to the issue of assembling the Au(111) wafer as the most prominent metal substrate in the field of SAMs of organothiols [38, 43, 45, 47, 48]. In addition to the wafer construction, we also explain other properties of the wafer related to surface reconstructions and possibilities of interaction with certain types of adsorbates.

2.1.1 Bulk structure of gold

The geometry of the gold crystal follows the face-centred cubic (FCC) Bravais lattice. The conventional unit cell of this lattice has a gold atom at each of the corners and in the centre of each of the faces (Fig. 2.1(a)). Its edge length is equal to the lattice constant of gold, a_{Au}, the value of which fully determines the position of all atoms in the crystal. The coordination number of each gold atom is 12 with the interatomic distance $d_{\text{Au-Au}} = (1/\sqrt{2})\, a_{\mathrm{Au}}$. The experimental value of a_{Au} at 293 K is 4.072 $Å$ [73].

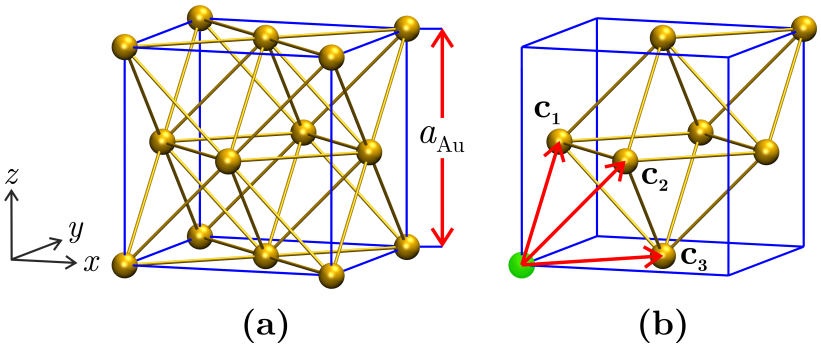

Figure 2.1: Bulk structure of gold crystal. **(a)** The conventional and **(b)** the primitive unit cell of the FCC lattice. Blue lines indicate the edges of the cubic crystal system. Red arrows show the primitive translation vectors. The green-labelled Au atom forms the basis.

The conventional unit cell in Fig. 2.1(a) is composed of 14 gold atoms but contains only 4 atoms in volume, i.e. 4 lattice points. From this structure, it is possible to derive a primitive unit cell, the smallest possible unit which can fill the entire crystal space. The primitive unit cell in Fig. 2.1(b) is constructed of 8 atoms that together make up one atom, or one lattice point, in the primitive cell volume. Geometrically, it is a parallelepiped spanned by three primitive translation vectors, $\mathbf{c_1}$, $\mathbf{c_2}$, and $\mathbf{c_3}$:

$$\mathbf{c_1} = \frac{a_{\mathrm{Au}}}{2}(\hat{\mathbf{y}} + \hat{\mathbf{z}})\,, \qquad \mathbf{c_2} = \frac{a_{\mathrm{Au}}}{2}(\hat{\mathbf{x}} + \hat{\mathbf{z}})\,, \qquad \mathbf{c_3} = \frac{a_{\mathrm{Au}}}{2}(\hat{\mathbf{x}} + \hat{\mathbf{y}})\,, \tag{2.1}$$

where $\hat{\mathbf{x}}$, $\hat{\mathbf{y}}$, and $\hat{\mathbf{z}}$ are unit vectors in the directions of x, y, and z-coordinate axis, respectively.

2.1.2 Bulk structure of gold: theoretical study

In this part, we only examine the geometric optimisation of the bulk gold in order to obtain its most important structural parameter, namely the relaxed value of a_{Au}.

Computational details

We build the unit cell from one basis atom of gold located at $(0, 0, 0)$ and define three lattice vectors according to Eq. 2.1. As the original estimation of a_{Au}, we use its experimental value of 4.072 *Å*. We employ the PBE implementation [59] of the GGA functional for exchange-correlation. For gold atomic species, we use a local-orbital SZP basis with a confinement energy shift of 0.01 *Ry*. In addition, we use a real-space cutoff of 250 *Ry* and sample the Brillouin zone using a 20×20×20 Monkhorst–Pack k-point grid with the displacement of 0.5 in all three real directions. With these parameters and the force tolerance of 0.02 $eV \cdot Å^{-1}$, we allow the value of a_{Au} to change while keeping the directions of the unitary lattice vectors fixed.

Lattice constant optimisation. For the relaxed gold crystal, we find the lattice constant of $a_{\mathrm{Au}} = 4.200$ *Å*, which is approximately 3 % above the zero-point corrected experimental value of 4.062 *Å*. Within the PBE-DFT framework, this positive relative error is one of the larger ones, but it is commonly accepted [74].

Overestimation of lattice constants is a natural shortcoming of semi-local functionals (PBE) because there is no way to accurately distinguish a two-particle Coulomb interaction from a self-interaction. The self-interaction error emerging in GGA functionals results in too high Coulomb repulsions and charge delocalisations, making the electrons more loosely bound to the atom. Therefore, larger inter-atomic distances, i.e. overestimated lattice constants, are expected.

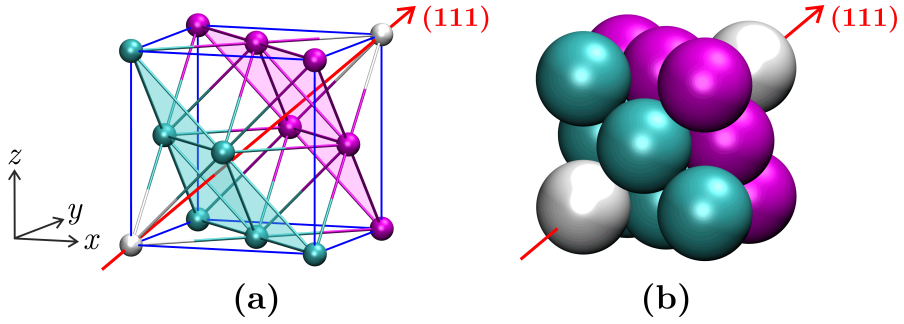

Figure 2.2: Crystal planes in gold crystal. (a) The conventional unit cell of the FCC lattice and **(b)** the cubic close-packed arrangement of equal spheres with the three types of colour-coded (111) crystal planes. The planes A, B, and C, are highlighted in white, turquoise, and magenta, respectively. Blue lines indicate the edges of the cubic crystal system. Red arrow shows the (111) direction.

2.1.3 Au(111) wafer

The FCC lattice of gold includes three repeating (111) crystal planes which are perpendicular to the body diagonal of the cubic crystal system and intersect each of the three perpendicular Cartesian axes at regular distances equal to a_{Au}. We denote this planes as A, B, and C (Fig. 2.2(a)). The equidistant spacing between planes in the (111) direction is therefore $(1/\sqrt{3})a_{\mathrm{Au}}$. Each atom has 6 neighbours in the plane, 3 below and 3 above the plane. Such the bond coordination corresponds to the close-packed arrangement of equal spheres (Fig. 2.2(b)).

Au(111) wafer construction. By stacking the (111) planes on top of each other, we get the Au(111) wafer, a two-dimensional periodic array with a finite thickness. When assembling the wafer, we follow the simple hexagonal Bravais lattice in which the z-axis coincides with the (111) direction. The corresponding primitive cell has the shape of a right rhombic prism, contains 3 whole Au atoms (lattice points) in its volume and is spanned by three primitive translation vectors, $\mathbf{h_1}$, $\mathbf{h_2}$, and $\mathbf{h_3}$ (Fig. 2.3(a)). These vectors meet:

$$\mathbf{h_1} = \frac{a_{\mathrm{Au}}}{2\sqrt{2}}\left(\hat{\mathbf{x}} - \sqrt{3}\hat{\mathbf{y}}\right), \qquad \mathbf{h_2} = \frac{a_{\mathrm{Au}}}{2\sqrt{2}}\left(\hat{\mathbf{x}} + \sqrt{3}\hat{\mathbf{y}}\right), \qquad \mathbf{h_3} = \left(\sqrt{3}a_{\mathrm{Au}}\right)\hat{\mathbf{z}}\,. \tag{2.2}$$

The horizontal $\mathbf{h_1}$ and $\mathbf{h_2}$ are the same length and form an angle $\gamma = 120°$ (Fig. 2.3(b)). The vertical $\mathbf{h_3}$ is perpendicular to them.

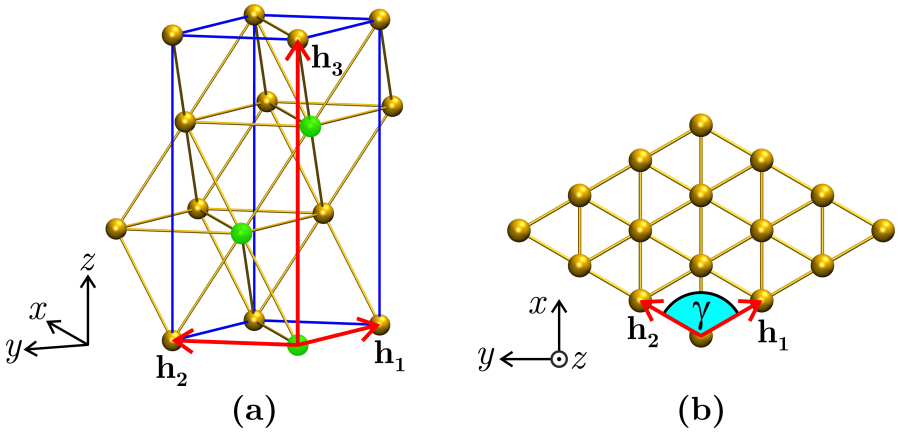

Figure 2.3: Au(111) wafer geometry. (a) The primitive unit cell of the hexagonal lattice and **(b)** the top view of the (4×4) unit cell of the (111) crystal plane. Blue lines indicate the edges of the hexagonal crystal system. Red arrows show the primitive translation vectors whose origin is in the A plane. The three green-labelled Au atoms form the basis.

Adsorption sites on Au(111) wafer. In this thesis, we use the four-layer Au(111) wafer with the *CBAC* layer sequence composed of (4×4) unit cells (Fig. 2.4). Its surface have many possible adsorption sites, four of which show a high level of symmetry and thus a considerable probability that adsorption will take place on them [75, 76]. Specifically, these are the atop, the bridge, the hcp hollow, and the fcc hollow sites (Fig. 2.4(c)).

The atop and the bridge sites are above the gold atom and above the gold-gold bond of the topmost C layer, respectively. The hcp and fcc hollow sites are above the centre of the triangle of 3 gold atoms of the C layer under which is the gold atom of the first subsurface B layer and the second subsurface A layer, respectively. At different adsorption sites, the contact between the anchoring atom and the metal surface acquires different degrees of coordination. The anchoring atom at the atop or bridge site is in a single or double coordination with the surface, respectively. The hollow sites provide a triple coordination with the surface. Many scientific papers [38, 76–78] have dealt with finding the energetically most favourable positions for the adsorption of sulphur atoms and sulphur-containing molecules on Au(111) surfaces, with the fcc hollow position being found to be the most advantageous one.

Surface free energy of Au(111) wafer. In an ideal approximation, the Au(111) wafer is an atomically flat close-packed FCC surface, which is often used in DFT cal-

culations of gold-molecule junctions with thiol anchoring groups [38, 49, 77, 79, 80]. According to Fig. 2.4, we see that topmost gold atoms have a reduced coordination number to 9 (6 in the plane and 3 below the plane). The same goes for the bottom layer. Surface atoms with reduced bond coordination experience an increase in surface stress leading to a higher surface free energy. This makes the surface more reactive [81, 82]. In combination with the strong affinity of sulphur for the gold surface [47, 72], SAMs of molecules with thiol anchoring groups are very readily formed [47, 83–85].

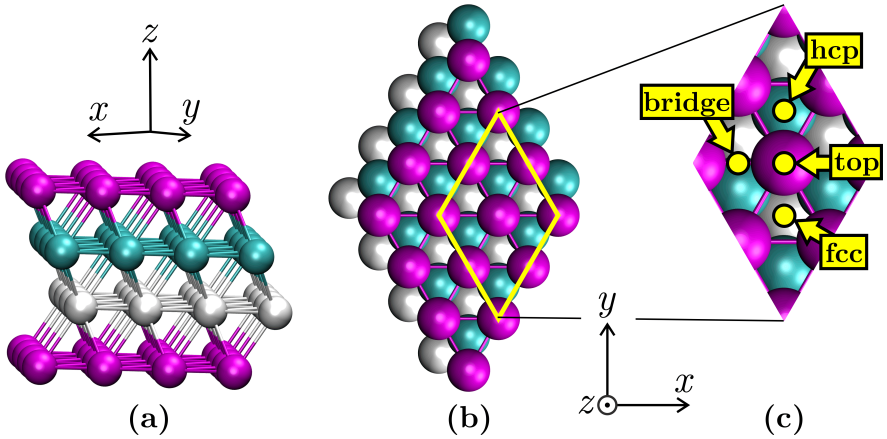

Figure 2.4: Au(111) unit cell and adsorption sites. **(a)** The side and **(b)** the top view of the (4×4) unit cell of the four-layer Au(111) wafer with the *CBAC* layer sequence. The planes *A*, *B*, and *C* are white, turquoise, and magenta, respectively. Yellow rhombus defines the (2×2) area referring to **(c)** the location of four types of high-symmetry adsorption sites. These sites are marked with yellow dots.

In addition to the increased surface reactivity, the flat gold surface is also subject to surface reconstructions [81, 82]. We imitate these reconstructions in the form of added surface asperities, which are the topic of the fourth chapter.

2.2 Silicon

In this thesis, we design all semiconductor substrates from mono-Si. We have two reasons for this: 1) mono-Si is the flagship of the modern PV industry and 2) represents the simplest form of silicon in terms of constructions and theoretical calculations. Since multi-Si is not the subject of our research, we use the terms ”mono-Si” and ”c-Si” interchangeably for the rest of the thesis.

In this section, we are interested in the geometric and partially the electronic features of the crystalline silicon, the gradual explanation of which we divide into five parts. In the first two parts, we pay attention to the bulk structure of c-Si. Then, we devote the rest of the section to the study of the Si(100) wafer, especially the ways of its assembling and its surface stabilisation. Regarding the stabilisation methods itself, we refer to the surface reconstruction and particularly the hydrogen passivation. In the last two parts, we investigate only the unreconstructed and fully hydrogen-passivated Si(100) wafer, i.e. the substrate intended for the formation of the silicon-molecule junctions studied in the fourth chapter.

2.2.1 Bulk structure of silicon

Monocrystalline form of silicon reveals a diamond-like structure following the FCC Bravais lattice whose the conventional unit cell has the edge length equal to the lattice constant of silicon, a_{Si}, (Fig. 2.5(a)). The diamond lattice can be viewed as a pair

of intersecting FCC lattices that are offset from each other by $(1/4, 1/4, 1/4)\, a_{\text{Si}}$. The resulting unit cell of the diamond lattice is geometrically composed of 18 silicon atoms and contains 8 atoms in volume, i.e. 8 lattice points. The first 4 lattice points come from one FCC unit cell and the other 4 lattice points come from the other FCC unit cell shifted by $(1/4, 1/4, 1/4)\, a_{\text{Si}}$.

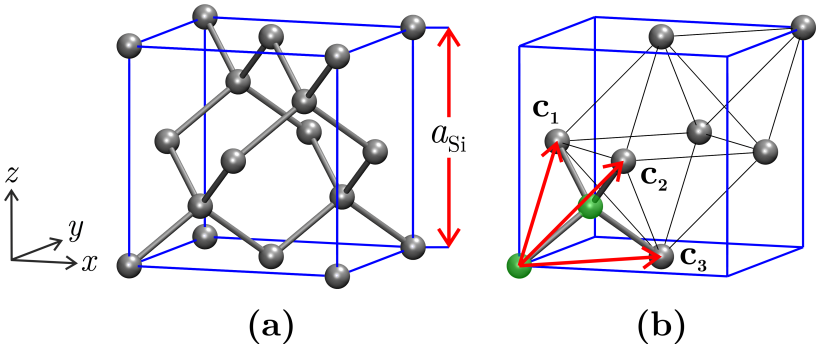

Figure 2.5: Bulk structure of c-Si. **(a)** The conventional and **(b)** the primitive unit cell of the cubic diamond lattice. Blue lines indicate the edges of the cubic crystal system. Red arrows show the primitive translation vectors. The two green-labelled Si atoms form the basis.

Silicon is a covalent crystal in which each silicon atom has a tetrahedral arrangement of covalent bonds with its four nearest neighbours. Covalent bonds in the diamond-like structure can be mathematically well described by sp^3 hybridisation supporting only σ-overlap of hybrid orbitals. The σ-bonds are the strongest types of covalent bonds in which electrons are strongly localised. This explains the considerable hardness and poor electrical conductivity of the crystal. The covalent Si-Si bonds have the length $d_{\text{Si-Si}} = (\sqrt{3}/4)\, a_{\text{Si}}$. The experimentally measured value of a_{Si} for high purity single crystal at 295.7 K in vacuum is 5.431 $\mathring{A}$. [86].

The basis of the cubic diamond lattice consists of two identical atoms which are located at $(0, 0, 0)$ and $(1/4, 1/4, 1/4)\, a_{\text{Si}}$ within the conventional cell. Based on this, the corresponding primitive cell (Fig. 2.5(b)) has 2 atoms in its volume, i.e. 2 lattice points. With the exception of one extra lattice point, the primitive cell of the diamond-like structure is geometrically identical to the primitive cell of the FCC lattice (Fig. 2.1(b)). Thus, gold and silicon have the same system of primitive translation vectors, which differ only in the value of lattice constants (Eq. 2.1).

2.2.2 Bulk structure of silicon: theoretical study

Regarding the theoretical study of the bulk silicon, we first optimise a_{Si} and subsequently calculate the band structure of the relaxed crystal.

Computational details

To relax the value of a_{Si}, we build the unit cell from two basis atoms of silicon located at $(0, 0, 0)$ and $(1/4, 1/4, 1/4)\, a_{\text{Si}}$ and define the corresponding $\mathbf{c_1}$, $\mathbf{c_2}$, and $\mathbf{c_3}$ in the same manner as in Eq. 2.1. As the original estimation of a_{Si}, we choose its experimental value of 5.431 $\mathring{A}$. We describe exchange-correlation using the PBE implementation [59] of the GGA functional and characterise silicon atoms through a local-orbital SZP basis set [87] with a confinement energy shift of 0.01 Ry. We employ a real-space cutoff of 250 Ry and a 20×20×20 Monkhorst–Pack k-point grid with the displacement of 0.5 in all three real directions. Under these

conditions, with the force tolerance of 0.02 $eV{\cdot}\mathring{A}^{-1}$, we allow the value of a_{Si} to change while keeping the directions of the unitary lattice vectors fixed.

After the lattice optimisation, we calculate the band structure of the optimised bulk silicon. We constrain the lattice geometry and use the same exchange-correlation and silicon atoms description, real-space cutoff and k-point grid as in the a_{Si} optimisation. We choose the **k**-point path: L $\rightarrow$ Γ $\rightarrow$ X $\rightarrow$ U|K $\rightarrow$ Γ.

Lattice constant optimisation. For the relaxed lattice of the bulk crystalline silicon, we receive the lattice constant of $a_{\mathrm{Si}} = 5.497(372)\ \mathring{A}$. As in the case of gold (part 2.1.2), we get an overestimated value relative to the zero-point corrected experimental one of 5.415 $\mathring{A}$, giving a positive relative error of 1.5 % [74].

Band structure. The calculated band structure of the relaxed bulk silicon is depicted in Fig. 2.6, from which we can read the band-gap energy: $E_{\mathrm{g}} = 0.83\ eV$, and the band-gap energy at Γ point: $E_{\Gamma} = 2.58\ eV$. Crystalline silicon is an indirect band gap semiconductor and therefore $E_{\Gamma} > E_{\mathrm{g}}$.

The value of 0.83 eV is strongly underestimated with respect to the experimental one of 1.17 eV [28]. The reason is again the self-interaction error arising in the PBE functional that reduces the electron binding energy of the solid. So the energies of the occupied states are shifted upwards and the band gap is narrowed [88].

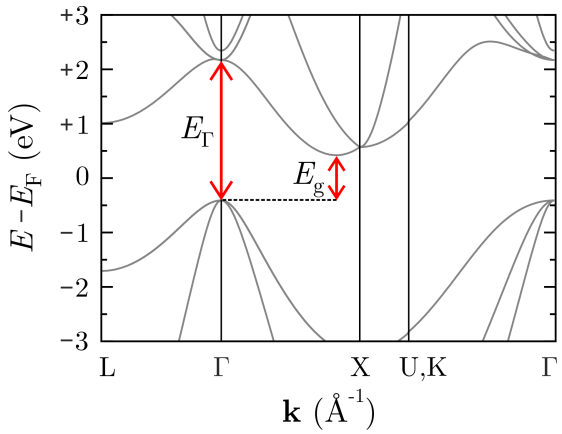

Figure 2.6: Band structure of bulk c-Si. The electronic energy levels of crystalline bulk Si as functions of the position along the **k**-point path: L $\rightarrow$ Γ $\rightarrow$ X $\rightarrow$ U|K $\rightarrow$ Γ. The levels are highlighted by grey lines. The Fermi level is shifted to zero to place all occupied and all empty states in the regions of negative and positive energies, respectively. Red arrows indicate $E_{\mathrm{g}} = 0.83\ eV$ and $E_{\Gamma} = 2.58\ eV$.

2.2.3 Si(100) wafer

Crystalline silicon contains only one type of repeating (100) crystal plane which is parallel to the xy-area and intersects the z-axis at regular distances equal to a_{Si} (Fig. 2.7(a)). So the z-axis is perpendicular to the (100) planes and coincides with the (100) direction. The inter-planar spacing corresponds to one Si(100) monolayer having a thickness of 4 Si layers. Stacking these monolayers on top of each other in the (100) direction, the Si(100) wafer is formed, the structure of which follows the simple tetragonal Bravais lattice. The respective primitive cell has the shape of a rectangular prism with a square base (Fig. 2.7(b)), contains 4 whole silicon atoms in its volume and is described by three primitive translation vectors, $\mathbf{t_1}$, $\mathbf{t_2}$, and $\mathbf{t_3}$:

$$\mathbf{t_1} = \left(\frac{a_{\mathrm{Si}}}{\sqrt{2}}\right)\hat{\mathbf{x}}\,, \qquad \mathbf{t_2} = \left(\frac{a_{\mathrm{Si}}}{\sqrt{2}}\right)\hat{\mathbf{y}}\,, \qquad \mathbf{t_3} = a_{\mathrm{Si}}\,\hat{\mathbf{z}}\,. \tag{2.3}$$

The horizontal $\mathbf{t_1}$ and $\mathbf{t_2}$ are the same length and all three vectors are perpendicular to each other.

The wafer in the form shown in Fig. 2.7(b) does not normally exist, mainly due to the reduced coordination number of surface silicon atoms. Specifically, surface atoms feel an unsatisfied valence of a radical nature, which leads to an increase in surface free energy. These radicals are immobilised on the surface and are called "dangling" bonds. If the tetragonal (bulk) arrangement of bonds on the Si(100) surface is maintained, then each atom of the topmost layer has the coordination of 2 and thus two dangling bonds. This corresponds to the bulk-terminated (1×1) surface (Fig. 2.8(a)) which has a considerable surface energy and is therefore unstable.

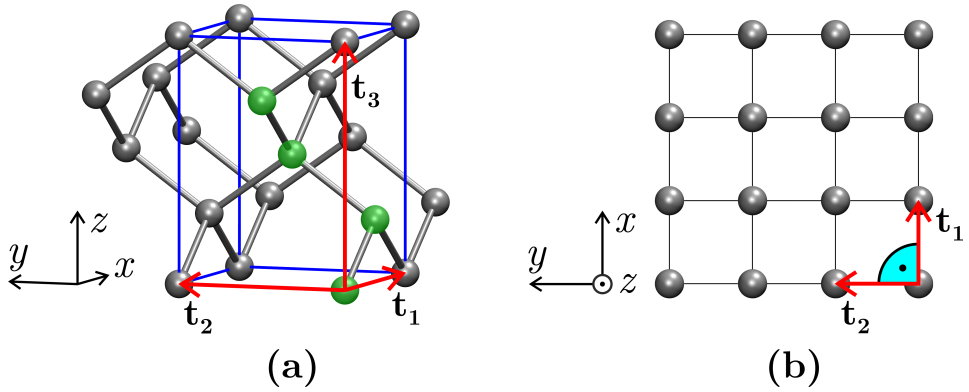

Figure 2.7: Si(100) wafer geometry. **(a)** The primitive unit cell of the tetragonal lattice and **(b)** the top view of the (4×4) unit cell of the (100) crystal plane. Blue lines indicate the edges of the tetragonal crystal system. Red arrows show the primitive translation vectors. The four green-labelled Si atoms form the basis.

Surface stabilisation processes. Silicon generally undergoes the two most common processes of surface stabilisation, namely surface reconstruction [89] and surface passivation [90, 91]. In both cases, the driving force is the balance between the reduction of dangling bonds and the minimisation of newly emerging surface stresses. In the following text, we first give a brief description of the surface reconstructions of the Si(100) wafer. Then, we describe in more detail the surface passivation by means of hydrogen atoms. In this thesis, we do not introduce surface reconstructions to stabilise the silicon surface. We remove all dangling bonds only by direct covalent grafting of hydrogen atoms.

Surface reconstructions. Surface reconstructions are geometric rearrangements of atoms, which mainly concern the surface and first subsurface layers. On the Si(100) surfaces, these are typically the formation of Si-Si dimers that reduce the number of dangling bonds per one topmost atom by half [89]. During the dimerisation, two adjacent topmost atoms tilt towards each other and form a σ-bond emerging from two dangling bond orbitals between them. The other two dangling bond orbitals pointed away from the σ-bond create a weak π-bond giving the symmetric dimer a partial π-bond character [89, 92]. Small atomic displacements from the bulk-like positions create stresses in the Si-Si bonds, which also extend into the subsurface layers and thus partially offset the surface energy drop caused by the dangling bond reduction [93]. Parallel arrays of dimers halve the surface symmetry because the corresponding

primitive cell is doubled. Such the surface, denoted as (2×1) (Fig. 2.8(b)), can only exist in a vacuum because it is still surrounded by reactive dangling bonds pointed away from the dimers. To remove the remaining reactive sites, the surface needs to be passivated. Details are described below.

Hydrogen passivation. In the field of semiconductors, passivation is either a spontaneous or controlled surface coverage by atoms or molecules that protect the properties of the substrate from various external influences. For photovoltaics, passivation is one of the most important surface treatments. It eliminates material defects, prevents recombinations of charge carriers and thus generally improves material properties leading to higher overall cell efficiencies. A typical example of spontaneous passivation is the covering the silicon surface with a thin layer of native oxide. This layer is formed during the oxidation of silicon in air and electrically isolates and stabilises the surface.

In terms of controlled surface coverage, hydrogen passivation is the simplest method as the relevant adsorbates are only hydrogen atoms. The hydride-terminated silicon has not only an almost absolute chemically homogeneous surface but also strong infrared stretching vibrations of Si-H bonds (ν(Si–H) $\sim$ 2100 cm^{-1}) which are suitable for surface geometry observation [94]. From a scientific point of view, hydrogen passivation is a relatively fundamental way of surface treatment because it is followed by almost all oxide-free functionalisation reactions [14, 91, 94]. The relevant products are various types of SAMs, the important features of which are described in Sec. ii.

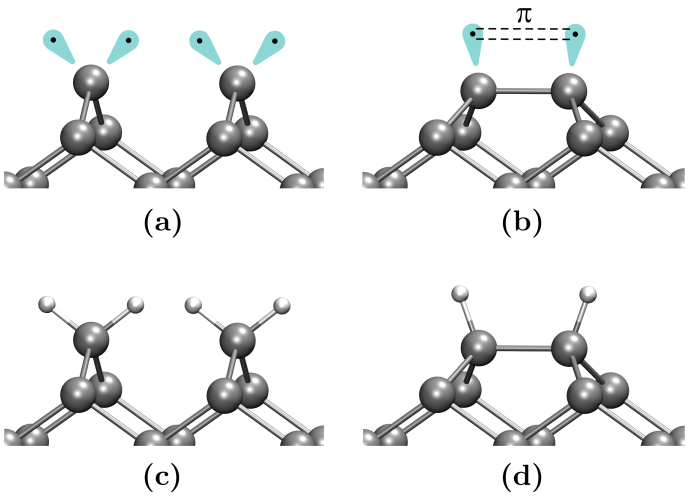

Figure 2.8: Dimerisation and hydrogen passivation of Si(100) surface. The side views of the top surface Si layers with 4 different types of terminations. **(a)** The bulk-terminated (1×1) and **(b)** the dimerised (2×1) structure of the non-passivated surface. Hydrogen passivation of these structures forms **(c)** the dihydride-terminated (1×1) and **(d)** the monohydride-terminated (2×1) surface, respectively. Turquoise-highlighted areas introduce dangling bond orbitals and black dots in them indicate immobilised radicals. Dashed lines denote the π-interaction between dangling bonds of the dimer.

In the case of Si(100), there can be either monohydride or dihydride-terminated surface or a mixture of both. The monohydride layer is formed on the reconstructed surface because each surface atom needs only one hydrogen atom to satisfy its valence (Fig. 2.8(d)). The dihydride layer is a part of the unreconstructed surface (Fig. 2.8(c)). Regarding the preparation of these surfaces, the two most common approaches are available, the details of which are described below.

The first approach is based on the adsorption of atomic hydrogen on the non-passivated Si(100) surface in an ultra-high vacuum. In addition, there is a hot tung-

sten filament through which H_2 flows and atomic hydrogen is formed. The surface temperature of the sample is decisive because it determines the final structure of the H-passivated product. Based on experimental[①] data, at above 600 K, the uniform monohydride-terminated (2×1) surface is observed [90, 91, 95]. When reduced to about 400 K, the mixture of monohydride and dihydride sites is formed [90, 91], indicating the ability of atomic hydrogen to cleave the Si-Si dimer bond. At room temperature, the dihydride-terminated (1×1) pattern is prevalent [90, 95].

Another and very traditional approach for the preparation of H-passivated Si(100) surfaces is a wet chemical etching. The conventional Si(100) wafer is immersed in a dilute HF (∼1 %) solution to remove the native SiO_2 layer. The passivated product is predominantly terminated by the dihydride layer [96, 97]. Compared to the substrates prepared in ultra-high vacuum, the conventional H-passivated Si(100) has facets (tilted planar surfaces) and microscopic asperities, potentially increasing the fraction of monohydride sites [96].

Regarding the stability in air, the H-passivated silicon does not give into any measurable degradation for up to tens of minutes [94]. Thus, the oxidation resistance of the substrate is sufficient between the removal of native SiO_2 layer and the subsequent oxide-free functionalisation process.

2.2.4 Dihydride-terminated Si(100) wafer

Our research on silicon substrates concerns only the dihydride-terminated Si(100) surface. It is the simplest case of silicon termination because each Si atom preserves its bulk-like position. At the same time, a number of complicated issues associated with the surface reconstruction are eliminated, especially those that could affect the molecule adsorption. This chosen surface is therefore a prototype system for our calculations.

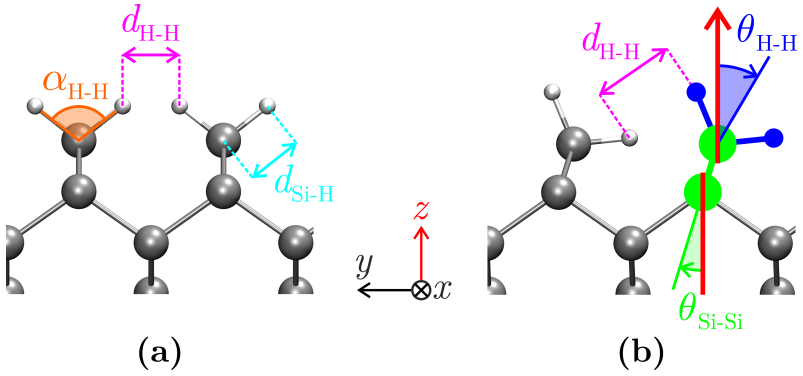

Figure 2.9: Dihydride-terminated Si(100) surface structures. The side view of **(a)** the straightened and **(b)** the canted phase of the dihydride-terminated Si(100) surface. The colour-coded quantities $\theta_{\text{H-H}}$, $\theta_{\text{Si-Si}}$, $\alpha_{\text{H-H}}$, $d_{\text{H-H}}$, and $d_{\text{Si-H}}$, are marked in blue, green, orange, magenta, and cyan, respectively, and are described in the main text. Red arrow indicates the surface-normal direction.

The dihydride-terminated Si(100) surface can be observed as the straightened or the canted structure [98][②]. The canted phase is more energetically favourable because it allows the hydrogen atoms to be further apart [99]. For the H-passivated silicon wafer, this means another important stage of surface stabilisation as strong repulsive

[①] These are mainly infrared spectroscopy and low-energy electron diffraction. Regarding the infrared data, the monohydride and dihydride sites have ν(Si–H) below and above 2100 cm^{-1}, respectively [90].

[②] The structures are distinguishable by analysis of depolarised Raman spectra of the chemically etched Si(100) surface.

interactions between adjacent dihydrides are lost.

From a geometric point of view (Fig. 2.9), the canted dihydride formation is triggered by a small rotation of the H_2 groups around an axis that passes through the topmost Si atoms. This is followed by a rotation of the entire terminal SiH_2 groups around an axis passing through the second layer Si atoms. For the final structures of this transformation, we define the canted angle of the H_2 groups, $\theta_{\text{H-H}}$, and of the top Si-Si bonds, $\theta_{\text{Si-Si}}$, with respect to the straightened phase geometry (Fig. 2.9(b)). Since $\theta_{\text{H-H}} > \theta_{\text{Si-Si}}$, the hydrogen-hydrogen spacing between adjacent SiH_2 units, $d_{\text{H-H}}$, increases significantly, namely by more than 0.5 $\AA$. This is accompanied by a slight elongation of the Si-H bond length, $d_{\text{Si-H}}$, and a small opening of the H-Si-H bond angle, $\alpha_{\text{H-H}}$, in the order of 10^{-2} $\AA$ and units of degrees, respectively [99].

The canted terminal SiH_2 units bring new stresses to the Si-Si bonds near the surface and therefore the necessary relaxation of several top Si layers occurs. The relaxing Si atoms lose their ideal bulk-like positions and thus partially offset the surface free energy drop caused by the loss of strong hydrogen-hydrogen repulsions. The balance between the reduction of these repulsions and the minimisation of emerging surface stresses is the driving force of the whole transformation from the straightened to the canted dihydride structure.

2.2.5 Dihydride-terminated Si(100) wafer: theoretical study

In this part, we deal with the theoretical study of geometric and electronic properties of the straightened and the canted dihydride structures of the H-passivated Si(100) wafer. We explore three important issues: (1) the straightened-dihydride layer optimisation, (2) the straightened to the canted-dihydride phase transformation, and (3) the electrostatic minimum wafer thickness.

Regarding the issue (1), we study the straightened-dihydride phase in which we optimise the dihydride layer on both sides of the wafer. In the next stage, we deal with the issue (2) where we investigate the geometry of transformation from the straightened to the canted-dihydride phase. This process is not spontaneous and must be initiated by a slight deformation of the upright structure. As a result, we can take the straightened structure as the metastable state and the canted structure as the ground state of the dihydride-terminated Si(100) surface.

In the end, we move on to the issue (3) where we examine the electrostatic properties of the straightened and the canted dihydride-terminated Si(100) surfaces at different wafer thicknesses. Within this issue, we first relax all the studied structures. Then, we determine the minimum thickness at which both wafer sides do not electronically affect each other. When this condition is met, for the electronic processes taking place on one side of the silicon slab, the other side is out of reach, making both sides electronically uncoupled. Therefore, we can employ the wafers of about 1 to 2 nm width which are much thinner and therefore much less computationally demanding than the real ones with a thickness of more than 100 μm.

In the following blue box, we describe the computational details of all the above-mentioned issues. Then, we report the resulting features of the optimised geometries both in terms of the structure and the electrostatic behaviour.

Computational details

In all calculations of the bare dihydride-terminated Si(100) surface, we characterise silicon and hydrogen atoms through a local-orbital SZP and DZP basis set, respectively, with a confinement energy shift of 0.01 Ry. We employ the PBE

implementation [59] of the GGA functional to describe exchange-correlation. We use a 250 Ry real-space cutoff. Regardless of wafer thickness, we introduce a vacuum gap of ∼12 $Å$ to remove interactions with the images in the vertical direction within the three-dimensional super-cell. For structural relaxation steps, we apply a tolerance of 0.02 $eV{\cdot}Å^{-1}$ below which the residual atomic forces must fall. Further computational details regarding each of the three issues are as follows:

Issue (1): We build the (1×1) unit cell of the straightened dihydride-terminated Si(100) wafer with a thickness of 8 Si layers. Thus, there are a total of 4 hydrogen and 8 silicon atoms. We sample the Brillouin zone in the parallel direction using a 8×8 Monkhorst–Pack k-point grid and relax only the coordinates of all hydrogen atoms; we set the fixed positions of silicon atoms.

Issue (2): We build the (4×4) unit cell of the straightened dihydride-passivated Si(100) wafer having 8 Si layers. Each Si layer and dihydride-passivation layer consists of 16 Si and 32 H atoms, respectively (Fig. 2.10(a)). We relax the positions of the topmost hydrogen atoms and the top three surface Si layers and sample the Brillouin zone in the direction parallel to the surface with a 2×2 Monkhorst–Pack k-point grid.

Issue (3): We assemble the straightened and the canted dihydride-terminated Si(100) wafers in the form of the (4×4) unit cells composed of 6, 8, 10, and 12 Si layers. So we have 8 different silicon wafers. We optimise their geometries via the same geometry-relaxation strategy as in the issue (2). The following are the calculations of the electrostatic potential energy of the relaxed (4×4) unit cells where we increase the reciprocal-space sampling density to a 6×6 k-point grid and introduce the slab dipole correction.

(1) Straightened-dihydride layer optimisation. To compile the initial geometry of the silicon wafer, we introduce the bond length $d_{\text{Si-H}} = 1.50$ $Å$ [99] and the bulk-like (tetrahedral) arrangement of all Si-H bonds with the angle $\alpha_{\text{H-H}} = \arccos(-1/3) \approx 109.47°$.

After the relaxation process, we get the top and the bottom straightened-dihydride layers with the optimised parameters: $d_{\text{H-H}} = 1.533$ $Å$, $\alpha_{\text{H-H}} = 104.063°$, and $d_{\text{Si-H}} = 1.493$ $Å$.

(2) Straightened to canted-dihydride phase transformation. We start with the geometry of the silicon wafer whose both sides are terminated by the upright SiH_2 units from the issue (1). On the top side of the wafer, we rotate each of the 16 upper H_2 groups by the canted angle $\theta_{\text{H-H}}$ between 0 and 30° in steps of 5°.

At the angle $\theta_{\text{H-H}} = 0°$, the straightened-dihydride phase is preserved during the structural relaxation step and the final structure has $d_{\text{H-H}} = 1.534$ $Å$, $\alpha_{\text{H-H}} = 103.902°$, and $d_{\text{Si-H}} = 1.494$ $Å$. These values are averaged over the relaxed top side of the (4×4) unit cell. The optimised geometry (Fig. 2.10(a)) is almost identical to the original one and represents the metastable state.

Using the angle $\theta_{\text{H-H}} > 0°$, we introduce artificial deformations on the surface which initially increase the total energy but allow the system to leave the metastable state during the relaxation and thus achieve the low-energy canted-dihydride phase. At the initial angle $\theta_{\text{H-H}} = 15°$, the canted phase acquires its lowest-energy conformation with

$d_{\text{H-H}} = 2.185$ $\mathring{A}$, $\alpha_{\text{H-H}} = 106.505°$, and $d_{\text{Si-H}}$ of 1.510 and 1.515 $\mathring{A}$ for the upper and the lower Si-H bond, respectively. This is consistent with the final canted angle $\theta_{\text{H-H}} = 30.840°$ and $\theta_{\text{Si-Si}} = 17.212°$. All these parameters are the averages over the relaxed top side of the (4×4) unit cell and we use them to rearrange the bottom side of the unit cell to obtain the centro-symmetric form of the canted dihydride-terminated Si(100) wafer (Fig. 2.10(c)).

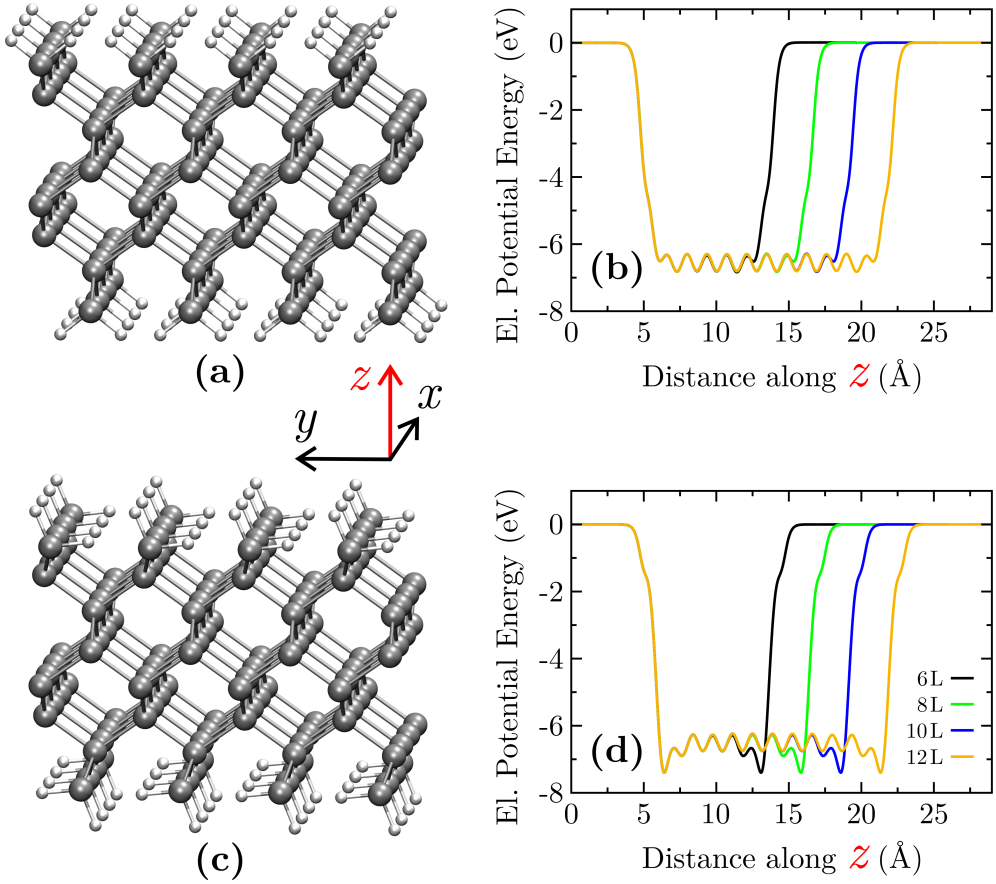

Figure 2.10: Study of dihydride-terminated Si(100) wafers. On the left-hand side, there are the side views of the (4×4) unit cells of **(a)** the straightened and **(c)** the canted dihydride-terminated Si(100) wafers composed of 8 Si layers. On the right-hand side, there are the plane-averaged electrostatic potential energies of **(b)** the straightened and **(d)** the canted dihydride-terminated wafers as the functions of the distance along the surface normal (z-axis). Black, green, blue, and yellow curves refer to the slabs consisted of 6, 8, 10, and 12 Si layers, respectively. The red arrow show the surface-normal direction.

(3) Electrostatic minimum wafer thickness. After the geometric characterisation of the straightened and the canted SiH_2 groups on the 8-layer silicon slabs, we get to the study of influences of these terminal units on the electrostatic properties of the wafers consisted of 6, 8, 10, and 12 Si layers. In this issue, at each slab thickness, we start with the initial structures of the dihydride-passivated Si(100) wafers in which the straightened arrangement of the terminal SiH_2 units follow the relaxed geometric parameters from the issue (1) and the complementary canted arrangement follow the relaxed parameters from the issue (2).

After the structural relaxation procedure of all assembled wafers, we calculate the electrostatic potential energy for each relaxed unit cell. We depict the plane-averaged potential energy curves of the straightened and the canted dihydride-terminated wafers in Fig. 2.10(b) and (d), respectively. To find the electrostatic minimum wafer thickness,

we determine for each potential energy profile the corresponding potential step as the difference between the asymptotic value to the left/right of the slab and the value in the middle of the slab[③].

In the case of the straightened-dihydride structures, the step is 6.58 eV for the 6-layer silicon slab (black curve) and 6.56 eV for the higher number of Si layers (other curves). The equivalent potential steps of the canted structures are 6.53 eV and 6.49 eV, respectively. So when moving from the 8-layer silicon wafer (green curve) to the thicker ones (blue and yellow curves), the height of the potential step changes only in the order of units of meV, which is even less than the usual strengths of London dispersion interactions in various non-polar systems. This means that the silicon wafer reaches the electrostatic minimum thickness when it consists of at least 8 Si layers.

Finally, we come to the summary of results of this part. Based on the issue (3), the Si(100) wafer composed of 8 Si layers is the best choice for both the straightened and the canted-dihydride phases because the corresponding potential energies in the centre of the slabs are sufficiently converged with respect to the bulk. Therefore, we stick to this wafer thickness for the rest of the thesis. When assembling the 8-layer wafer with the straightened terminal SiH_2 units, we employ the geometric features relaxed in the issue (1). To build the centro-symmetric wafer with the same thickness and the canted SiH_2 units, we use the structural quantities relaxed in the issue (2).

2.3 Carboranedithiol adsorbate

After the general characterisations of both types of substrates, we get to the study of the isolated *ortho*-carborane molecule (Fig. 2.11(a)) and particularly its two dithiolated derivatives with both unsaturated thiol linker groups (Fig. 2.11(b,c)). Both of these sulphur-functionalised positional isomers are able to interact with the wafer surface via thiol anchoring groups and form the adsorbed SAMs having the large surface dipole.

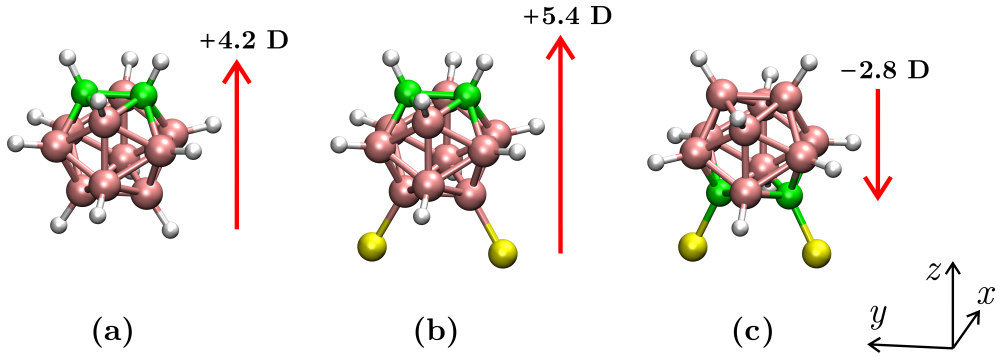

Figure 2.11: *Ortho*-carborane and its unsaturated dithiolated derivatives. The geometric representations of **(a)** 1,2-dicarba-*closo*-dodecaborane, **(b)** 9,12-S_2-1,2-dicarba-*closo*-dodecaborane, and **(c)** 1,2-S_2-1,2-dicarba-*closo*-dodecaborane. Red arrows represent the dipole moments of the respective molecules.

We divide this section into three parts in which we gradually investigate the geometric and the electrostatic features of the relevant molecules. In the first part, we are only interested in the *ortho*-carborane itself. Then, we describe in more detail the structures of the unsaturated dithiolated derivatives. The last part is devoted to the theoretical study of all three types of isolated molecules where we emphasise the monitoring of mutual electrostatic effects between adjacent molecular images within the super-cell.

[③] We read the value from the macro-averaged (nano-smoothed) potential energy profile.

2.3.1 Carborane

Dicarba-*closo*-dodecarboranes (carboranes, $C_2B_{10}H_{12}$) are cage-like structures exhibiting remarkable electronic properties, including large magnitudes of μ_{Mol}. The carborane molecule has an icosahedral geometry with 20 sides and 12 vertices, in which 2 carbon and 10 boron atoms are hexacoordinated and form a three-dimensional aromatic system [100, 101].

The different electronegativities of C and B backbone atoms result in a non-uniform electron density distribution in the carborane cage, which, depending on the position of backbone atoms, leads to various molecular dipoles. The carborane molecule has three different positional isomers that differ in the relative position of carbon atoms in the icosahedral skeleton and thus also in the magnitudes of μ_{Mol} ranging from zero to over 4 Debyes (D)[④] [102]. In this thesis, we consider only 1,2-dicarba-*closo*-dodecaborane (*ortho*-carborane, Fig. 2.11(a)), which is, next to 1,7- and 1,12-dicarba-*closo*-dodecaborane (*ortho*- and *para*-carborane), the positional isomer with the largest dipole magnitude [100–102].

Three-dimensional aromaticity. The icosahedral cage of carborane molecules excels in considerable thermal stability and high chemical resistance, which is not disturbed by the binding of functional groups [101, 103]. These advantages are a direct consequence of the three-dimensional aromaticity (σ-aromaticity) of the carborane cluster, which is different from the classical two-dimensional aromaticity (π-aromaticity) of planar, conjugated, cyclic hydrocarbons. In particular, the carborane cage is aromatic because: (1) it contains electron-deficient bonds causing the delocalisation of skeletal electrons over the icosahedral surface, and (2) it has a closed-shell electronic structure, thanks to which the cluster accepts functional groups only as a substitute for hydrogen and the delocalisation of its skeletal electrons is not disturbed [104, 105].

The hexacoordinated carbon and boron atoms need a total of 30 two-centre bonds to form the icosahedral structure. However, the valence sphere of the carborane backbone has only 26 skeletal valence electrons which, in the form of bonding electron pairs, have to delocalise over more than two backbone atoms and form electron-deficient bonds. These 26 skeletal electrons occupy 13 bonding molecular orbitals, 12 of which are formed by σ-interactions between pairs of p_x and p_y atomic orbitals that are tangential to the icosahedral surface. The thirteen unique molecular orbital inside the carborane cluster is created by the in-phase overlap of sp_z hybrid atomic orbitals oriented towards the centre of the backbone [104, 105].

Dipole moment. The distribution of charges in the carborane cage is controlled by the two fundamental electronic properties of the molecule: the σ-aromaticity of the carborane cluster and the electron-withdrawing character of the carbon atoms [100, 101].

First of all, it is good to realise that each boron and carbon atom introduces 2 and 3 skeletal electrons, respectively, into the valence sphere of the carborane molecule. Due to the extensive electron delocalisation over the icosahedral surface, the two "extra" electrons of the carbon atoms are no longer bound to the nuclei, leaving partial positive charges on the carbon atoms and partial negative charges on the boron atoms. This is the consequence of the σ-aromaticity of the cluster [100].

The magnitudes of charges on individual skeletal atoms are controlled by the inductive effect in which more electronegative carbon atoms withdraw a considerable electron density from the neighbouring boron atoms. But even so, the carbon atoms

[④] $1\ D \approx 3.336 \times 10^{-30}\ C \cdot m$

remain positively charged and the boron atoms furthest from them are the most negative [100, 101]. In the case of the *ortho*-carborane molecule, the differences in the cage charges are the most noticeable of all the carborane isomers, leading to the largest μ_{Mol} that points from the negative boron side to the positive carbon side (Fig. 2.11(a)).

2.3.2 Carboranedithiol

As mentioned above, in this thesis, we employ only two types of molecular adsorbates which are the two positional isomers of the dithiolated *ortho*-carborane molecule with both unsaturated thiol end groups. Specifically, we study 9,12-S_2-1,2-dicarba-*closo*-dodecaborane and 1,2-S_2-1,2-dicarba-*closo*-dodecaborane (see Fig. 2.11(b) and (c)) [31–34, 37]. Since sulphur atoms have the feature of anchoring groups during the adsorption, for the rest of the thesis, we name these isomers as the B-bonded and the C-bonded carboranedithiol, respectively.

The covalent bonding of the sulphur atom to any atom of the carborane backbone does not disturb the delocalisation of the skeletal electrons and thus also the aromaticity of the cluster. However, the charge rearrangement occurs because the sulphur atoms are similarly electronegative as the carbon atoms and thus withdraw the electron density from the cluster via the inductive effect. In this way, the changes in the magnitude of μ_{Mol} up to units of D can be expected.

The B-bonded carboranedithiol has the sulphur atoms covalently bonded to the boron side of the cage, resulting in the amplification of the negative charge on this side and the increase in the dipole magnitude (Fig. 2.11(b)). The opposite situation takes place for the C-bonded carboranedithiol (Fig. 2.11(c)).

2.3.3 Carborane and carboranedithiol: theoretical study

Our last theoretical study of this chapter is the investigation of the structural and the electronic features of the isolated *ortho*-carborane molecule and its two unsaturated dithiolated derivatives.

We first optimise the geometries of the listed molecules. Then, for each type of the relaxed structure, we investigate the corresponding dependence of μ_{Mol}[⑤] on the size of the unit cell in order to determine the minimum unit-cell dimension that creates a sufficient vacuum space around the molecule, making an adequate electrostatic isolation from adjacent images in all orthogonal directions. When these conditions are met, the corresponding value of μ_{Mol} belongs to the electrostatically isolated molecule.

In the following blue box, we provide the computational details related to this part. Then, we move on to the results of the study of the isolated carborane-based molecules.

Computational details

As the initial estimation of the geometry of each type of the isolated molecule, we employ the Cartesian coordinates from Schwartz et al. [106]. We use a local-orbital DZP basis set with a confinement energy shift of 0.01 *Ry* to characterise boron, carbon, hydrogen, and sulphur atoms. We describe exchange-correlation via the PBE implementation [59] of the GGA functional. We use a real-space cutoff of 250 *Ry* and sample the Brillouin zone at the Γ point.

During the structural relaxation step, we employ the automatic generation of the primitive translation vectors that create a vacuum space around the isolated molecule to eliminate interactions with the images. We optimise the coordinates

[⑤] In this section, the dipole μ_{Mol} coincides with the dipole of the unit cell μ_{unit}, so $\mu_{\text{Mol}} = \mu_{\text{unit}}$.

of all molecular atoms until residual forces fall below 0.02 $eV{\cdot}\mathring{A}^{-1}$.

After the geometry optimisation, we place the given type of the molecule in the centre of the cubic unit cell with the size from (11×11×11) to (60×60×60) $\mathring{A}^3$ in steps of (1×1×1) $\mathring{A}^3$. For each unit cell size, we perform the single-point calculation with and without the implementation of the slab dipole correction.

Geometry optimisation. We get the relaxed geometries of the *ortho*-carborane molecule and the B-bonded and the C-bonded *ortho*-carboranedithiol isomers in the automatically generated unit cells of a rectangular shape and side lengths of about 11.5 to 12.5 $\mathring{A}$.

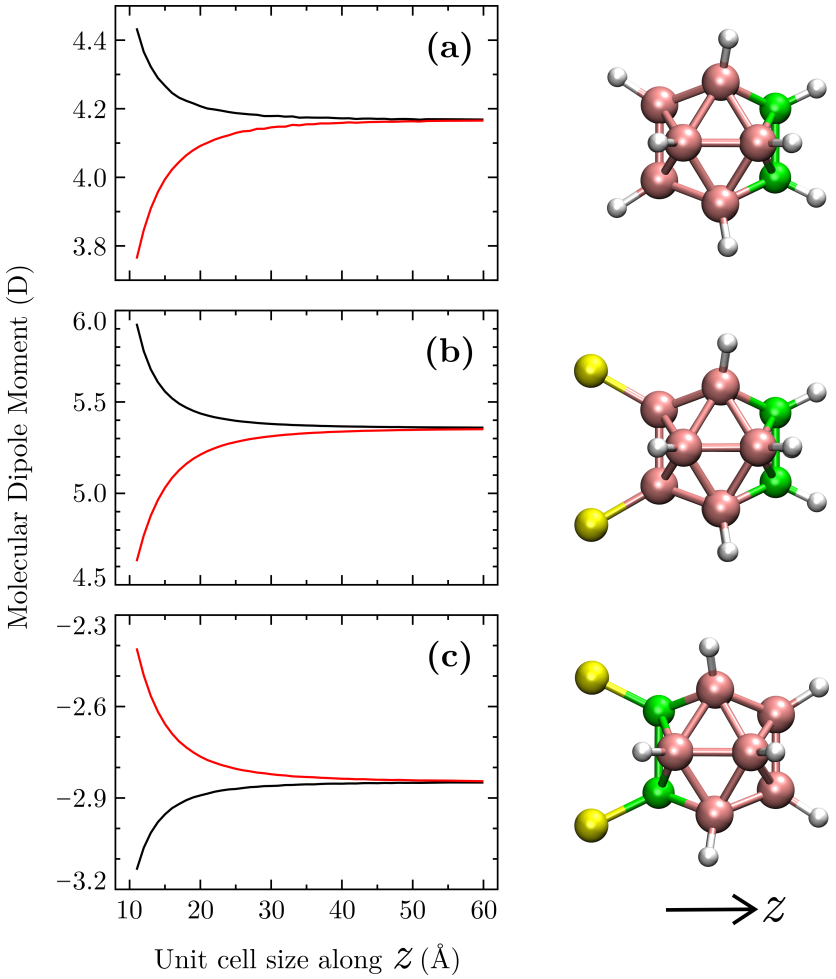

Figure 2.12: Dipole moments of isolated carborane-based molecules. Molecular dipole moment as a function of the unit cell size along the z-axis for **(a)** the *ortho*-carborane molecule, and for **(b)** the B-bonded and **(c)** the C-bonded *ortho*-carboranedithiol isomers with the unsaturated thiol groups. Red and black curves refer to data with and without the implementation of the slab dipole correction, respectively. To the right of each plot is the geometric representation of the corresponding molecule with the dipole μ_{Mol} aligned along the z-axis, so $\mu_{\text{Mol}} \parallel z$-axis.

Dipole moment of isolated molecules. For each type of the studied molecule, we plot the dependence of μ_{Mol} ($\mu_{\text{Mol}} \parallel z$-axis)[6] on the size of the unit cell along the

[6] As we mention in Sec. iii, only the z-component of the dipole is relevant for the interfacial charge transfer, so $\mu_{\text{Mol}} \parallel z$-axis.

z-axis, as shown in Fig. 2.12. With the increasing size of the unit cell, we observe a clear convergence of the dipole to the asymptotic value corresponding to the situation in which the molecule is electrostatically isolated from its adjacent images. The asymptote of the *ortho*-carborane molecule is $\mu_{\mathrm{Mol}} = +4.17\ D$ (Fig. 2.12(a)). Its unsaturated dithiolated positional isomers with the B-bonded and the C-bonded sulphur atoms acquire μ_{Mol} of $+5.36$ and $-2.84\ D$ (Fig. 2.12(b) and (c)), respectively, under the same conditions.

On the left sides of the plots, i.e. in the region of unit cells approximately smaller than $(20{\times}20{\times}20)\ \mathring{A}^3$, the magnitude of μ_{Mol} of each system varies very sharply with the unit cell size. This is because the electrostatic effects of adjacent replicas are significant, making the resulting dipole very sensitive to changes in the thickness of the vacuum layer between the nearest molecular images.

Regarding the data without the slab dipole correction (black curves), we see the dipole magnitudes decrease with the growing cell size because their values on the left-hand side of each plot are quite overestimated relative to the corresponding asymptotes on the right. The reason for this trend is that in each unit cell, the course of the electrostatic potential energy along the z-axis has a potential step across the molecule (see Eq. 3), but within the super-cell, the potential-energy course also has to meet the PBCs. Therefore, the potential energy in the vacuum layer between the images does not proceed as a flat function but reveals a linear slope, giving rise to a "spurious" electric field which, via the electric-field induced polarisation, increases the magnitude of μ_{Mol} [107]. According to the courses of the black curves, we see the most effective way to eliminate the spurious field is to expand the vacuum space between the individual dipoles, i.e. increase the volume of the unit cell.

To remove the spurious polarisation, we can also employ the slab dipole correction which offsets the linear slope of the electrostatic potential energy by a sawtooth-like function placed in the middle of the vacuum layer. However, the respective dependences of μ_{Mol} on the unit cell size (red curves) suggest that the compensating effect of the dipole correction is somewhat out of proportion, leading to excessive depolarisation of all studied molecules in the region of small cell sizes. Therefore, on the left-hand side of each plot, the red curves reveal the underestimated values of the dipole magnitudes with respect to the asymptotes on the right. The probable main cause may be the insufficient spatial homogeneity of the potential energy within the lateral xy-area [108] in which, unlike wafers or slabs, the molecules themselves are non-periodic systems. As the unit cell volume increases, the depolarisation influence of the dipole correction weakens and the increasing magnitudes of μ_{Mol} converge to the same asymptotic values as the black curves.

3. Gold-molecule junctions

In this chapter, we present a way to tune the gold work function by means of cage-like molecules with a large intrinsic dipole moment. For this purpose, we study the structural and the electronic properties of the *ortho*-caboranedithiols chemisorbed on Au(111) surfaces. We consider two positional isomers of these adsorbates, with thiol linker groups attached to either carbon or boron backbone atoms, such that when adsorbed on the Au substrate, the molecular dipole points towards the metal surface or away from it. We investigate a large number of junction geometries and find the caboranedithiol adsorption can induce significant changes in the work function of the Au substrate, namely in the range of 1 eV. These changes depend strongly on the interface geometry at the atomistic level. From the analysis of these junction structures, we provide a picture of the driving mechanisms that determine adsorption geometries, and relate them to interface electronic structure and resulting work function modification. In particular, our results highlight the important role played in these interface quantities by distortions in the Au surface layer induced by the caboranedithiol adsorption. We also focus on the effects of natural surface roughness influencing the properties of metal-organic interfaces at the atomistic level.

3.1 Preface

The high stability against heating and chemical influences and the ability to form almost defect-free monolayer structures are essential properties of the rigid cage-like molecules, thanks to which they have attracted a lot of attention among SAMs created on various metal surfaces [33, 34, 37], especially gold [31, 32, 38, 41, 42, 44, 45, 48, 49]. In general, gold is the preferred substrate for its inert character, as mentioned in Sec. 2.1, leading to easier preparations of functional interfaces for a plenty of gold-molecule junctions.

Sulphur atoms, or thiol functional groups, as structural components of molecular adsorbates are very important linkers between the monolayer and the metal surface. A well-known standard in this field are SAMs of alkanethiols on gold, which have had an enormous impact on surface studies, materials science, biology, molecular electronics, and others [16, 17, 43, 46]. In this thesis, we explore the gold surface modified with the cage-like molecules of *ortho*-carboranedithiols (Fig. 3.1), which excel in their unique electronic properties (see Sec. 2.3) and, compared to many alkanethiol counterparts, possess a more pronounced intrinsic dipole moments [31, 32, 38, 49]. Specifically, we employ the B-bonded and the C-bonded *ortho*-carboranedithiol positional isomers with unsaturated thiol anchoring groups (see Fig. 2.11(a) and (b), respectively, and the top and the bottom panel of Fig. 3.1(a), respectively).

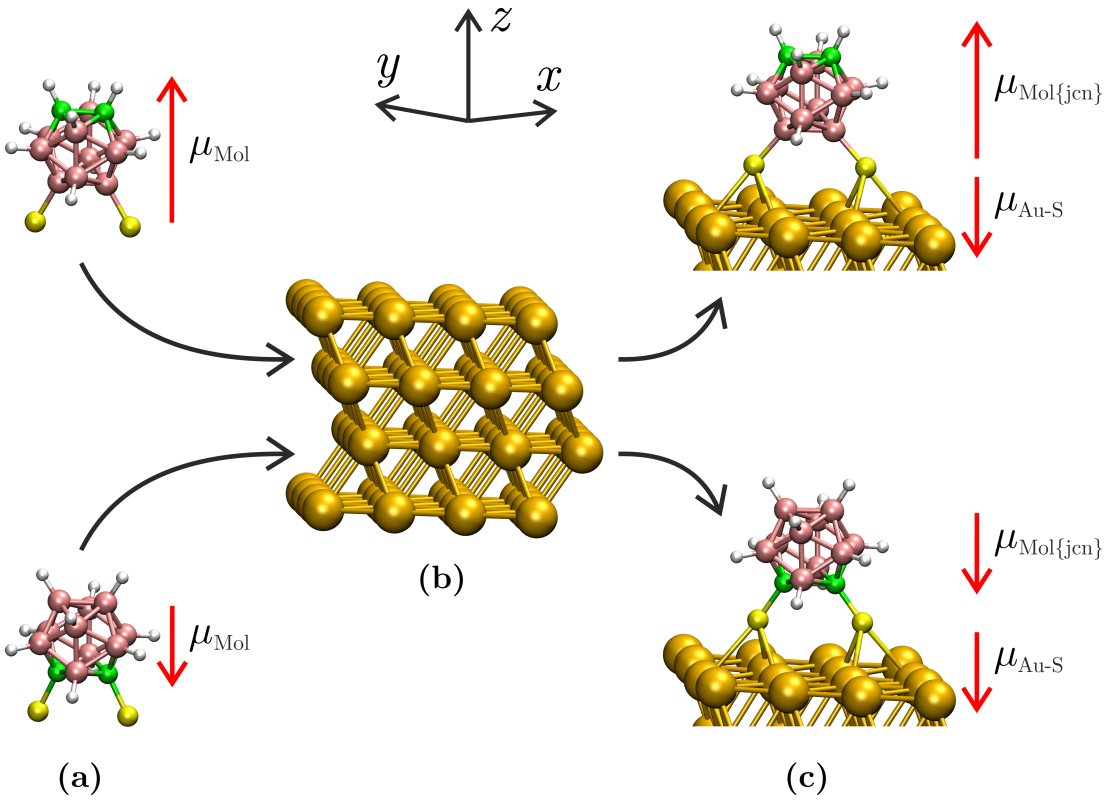

Figure 3.1: Adsorption of *ortho*-carboranedithiols on Au(111). The geometric representations of **(a)** two positional isomers of the unsaturated *ortho*-carboranedithiol molecule, **(b)** the unit cell of the Au(111) wafer composed of 4 Au layers, and **(c)** the two resulting structures of the gold-carboranedithiol junction. Red arrows indicate the dipole moments of the depicted structures, namely μ_{Mol}, $\mu_{\mathrm{Mol\{jcn\}}}$, and $\mu_{\mathrm{Au\text{-}S}}$ which are described in the main text. The top and the bottom panels of **(a)** and **(c)** refer to the B-bonded and the C-bonded carboranedithiol-based geometries, respectively.

When the *ortho*-carboranedithiols are adsorbed on the metal surface (Fig. 3.1(c)),

the geometry of the chemisorbed molecule and the details of the gold-molecule interface have a dominant effect on the resulting electronic properties, especially on the dipole moment of the gold-molecule junction, $\mu_{\text{Au-Mol}}$, which corresponds to the sum:

$$\mu_{\text{Au-Mol}} = \mu_{\text{Mol}\{\text{jcn}\}} + \mu_{\text{Au}\{\text{jcn}\}} + \mu_{\text{Au-S}} \tag{3.1}$$

where $\mu_{\text{Mol}\{\text{jcn}\}}$ and $\mu_{\text{Au}\{\text{jcn}\}}$ are the dipole moments of the isolated molecular adsorbate and the bare Au substrate, both of which in the junction basis-set and the geometry they adopt in the junction structure; $\mu_{\text{Au-S}}$ is the dipole moment of the gold-molecule interface where the Au-S bonds are formed. During the adsorption of the molecule, all charge transfers between the substrate and the adsorbate take place in the surface-normal direction, i.e. along the z-axis, and therefore each quantity in Eq. 3.1 is the z-component of the respective μ.

According to Fig. 3.1(c), $\mu_{\text{mol}\{\text{jcn}\}}$ can point either towards the surface or away from it, depending on whether the C-bonded (bottom panel) or the B-bonded carboranedithiol (top panel), respectively, is chemisorbed on the gold. However, $\mu_{\text{Au-S}}$ always goes to the surface because the sulphur atoms represent the more electronegative side of each Au-S bond. In cooperation with the substrate, both of these dipole contributions mediate the interfacial charge transfer between the gold and the molecule. As we show in this chapter, metal–molecule hybridisation and the resulting charge transfer and rearrangement strongly affect the interface electronic structure, allowing us to change the work function of the metal surface by more than 1 *eV*.

3.2 Chapter overview

We perform the theoretical study of the gold-carboranedithiol junctions in three stages, introducing one section for each stage. In the first stage (Sec. 3.3), we explore various adsorption geometries of both the B-bonded and the C-bonded carboranedithiol isomers on the Au(111) surface. After the structural relaxation of all geometries, we select two prominent structures, i.e. one for each isomer, with the greatest influence on the electronic properties of the substrate. We subject these structures to other stages of the study of the gold-molecule junctions.

In the second stage (Sec. 3.4), we explore the charge density and the electrostatic potential energy of the selected structures and the changes of the relevant quantities associated with the formation of the gold-molecule interface. One of the important results of this section is the work function change of the gold substrate, $\Delta\Phi_{\text{Au}}$, caused by the adsorption of the carboranedithiol molecule.

In the following blue box, we summarise the computational details of all mentioned stages of the study of the gold-molecule junctions.

Computational details

For the geometry relaxations and the subsequent electronic structure calculations, we characterise gold and molecular atoms via a local-orbital SZP and DZP basis set, respectively, with the largest (shell-dependent) values for the radial confinement radii (*Bohr*): 6.459 (boron), 5.205 (hydrogen), 5.519 (carbon), 5.487 (sulphur), 6.723 and 10.544 (gold). We use the larger cutoff radii for the gold atoms of the top surface Au layer and Au adatoms to provide a better description of the wave function decay into the vacuum. We describe exchange–correlation, including van der Waals interactions, using the vdW-DF functional of Dion et al. [64] in the implementation of Román-Pérez and Soler [109]. Further details on the calculations of the gold-molecule junctions are as

follows:

First stage (Sec. 3.3)**:** We build the unit cell containing the *ortho*-carborane-dithiol molecule positioned above the (4×4) slab of the Au(111) wafer with a thickness of 4 Au layers. Thus, each Au layer consists of 16 gold atoms[①]. We introduce a vacuum gap of ∼10 $\AA$ to remove interactions with the images in the surface-normal direction. To obtain stable gold-molecule junctions, we relax the coordinates of the molecule, the top surface Au layer and, in the presence of surface asperities, also Au adatom(s) until residual forces fall below 0.02 $eV \cdot \AA^{-1}$.

Second stage (Sec. 3.4)**:** We assemble the unit cells of the isolated molecule and the bare Au(111) wafer from the unit cell of the relaxed gold-molecule junction. In this procedure, we preserve the atomic arrangement, the unit cell size, and the extent of the basis set[②]. Under frozen-geometry conditions and the slab dipole correction, for each of the mentioned structures, we calculate the distributions of the electron and the ionic-charge density.

Then, we calculate the distributions of the electrostatic and the neutral-atom potential energies for the relaxed gold-molecule junction and for the bare Au(111) wafer with the optimised top surface Au layer. As with charge-density calculations, we describe each of these systems in the unit cell size of the junction, but this time in their own basis sets (without ghost orbitals).

In addition, in all calculations of the junction, we use a 250 *Ry* real-space cutoff and sample the reciprocal space in the direction parallel to the surface with a 6×6 Monkhorst–Pack k-point grid [110]. We prove the sufficient convergence at this k-point sampling level in Sec. 3.5.

[①] With this lateral size, the effect of adjacent unit-cell images on the molecular geometry is small. We check this by optimising the geometry in larger unit cells containing the (5×5) and the (6×6) slab. Going from the 16- to the 36-atom-per-layer cell, i.e. from the surface area $\Omega = \sim 122$ to ~ 275 $\AA^2$, the position of each atom in the *ortho*-carboranedithiol molecule changes by only 0.0004 $\AA$ on average.

[②] We calculate the isolated molecule and the bare Au substrate in the unit cell and the basis set of the corresponding junction. Specifically, under such conditions, the molecular atoms "borrow" the empty basis set of the Au substrate, and the Au atoms of the substrate borrow the empty basis set of the molecule. The functions of the empty basis set consist of "ghost" orbitals, i.e. orbitals that are not filled with electrons. So when describing the electronic structure of the molecule, Au ghost orbitals are used and *vice versa*. By using ghost orbitals, we introduce corrections to basis-set superposition errors.

3.3 Adsorption of carboranedithiol on Au(111)

In this section, we examine the geometry of the carboranedithiol adsorption on the gold surface and the structural characteristics of the newly formed interface. In order to properly sample the adsorption structures, we systematically investigate a large number of initial geometries of the molecule above the substrate by probing the molecular azimuthal angle, φ_{Mol}, with respect to Au rows (Fig. 3.2(a)) as well as the molecular tilt angle, θ_{Mol}, with respect to the surface normal (Fig. 3.2(b)).

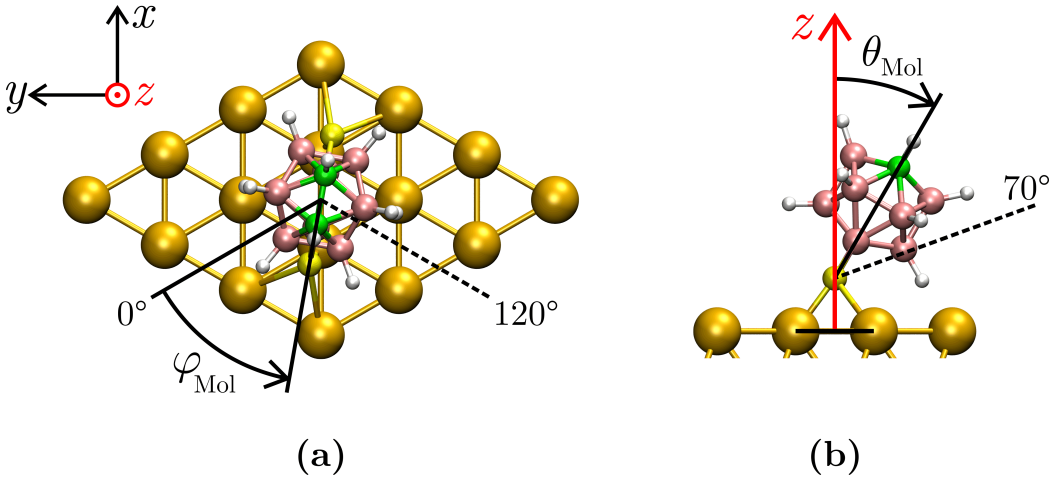

Figure 3.2: Initial geometries of gold-molecule junctions. Generation of initial geometries of the carboranedithiol molecule above the (4×4) slab of the Au(111) wafer. **(a)** The top view of the junction with probing of the azimuthal angle φ_{Mol} between 0 and 120°. **(b)** The side view of the junction with probing of the tilt angle θ_{Mol} between 0 and 70°. The quantities are described in the main text. Red arrow indicates the surface-normal direction (z-axis).

We divide this section into three parts, the first and the second of which concerns the study of the azimuthal and the polar orientation of the molecular adsorbate, respectively, on the flat gold surface. In the last part, we investigate the effect of surface asperities on the interface geometry.

3.3.1 Azimuthal orientation

We generate initial geometries of each of the two carboranedithiol isomers by placing the centre of their carborane cage above the Au-Au bond. For these conformations, we define the azimuthal angle φ_{Mol} as the angle between the line connecting both S atoms and the row of surface Au atoms (Fig. 3.2(a)). We change the angle φ_{Mol} by rotating the molecule around its main rotation axis[③] in steps of 10° between 0 and 120°. In this way, for each isomer, we obtain 13 initial structures (a total of 26 structures) where the molecule is adsorbed vertically on Au, i.e. the main rotation axis is parallel to the surface normal. We subject each of these conformations to the relaxation process.

Simulations indicate that structures of the metal-molecule junction are driven by the binding of the S atoms and influenced by the molecular tilt angle. In particular, the final geometries consistently show the S atoms adsorbed near hollow sites on the Au surface. In most of these conformations, the molecule remains in its almost vertical orientation ($\theta_{\text{Mol}} < 3°$) during the relaxation and its angle φ_{Mol} converges close to

[③] The main rotation axis of the carboranedithiol molecule passes through the centre of the C-C bond, the centre of the carborane cage, and the centre of the line connecting both S atoms.

either 10 or 110° (see Fig. 3.3(a) or (b), respectively), which are mutually equivalent by mirror symmetry.

At the initial angle $\varphi_{\mathrm{Mol}} = 60°$, none of the isomers form vertically adsorbed structures in Fig. 3.3, and due to the strong steric repulsions between the carborane cage and the top gold atoms, the molecule tilts considerably ($\theta_{\mathrm{Mol}} \sim 30°$). This is associated with a more advanced relaxation of the gold surface leading to lower total energy of the system. We investigate the role of the angle θ_{Mol} in more detail below.

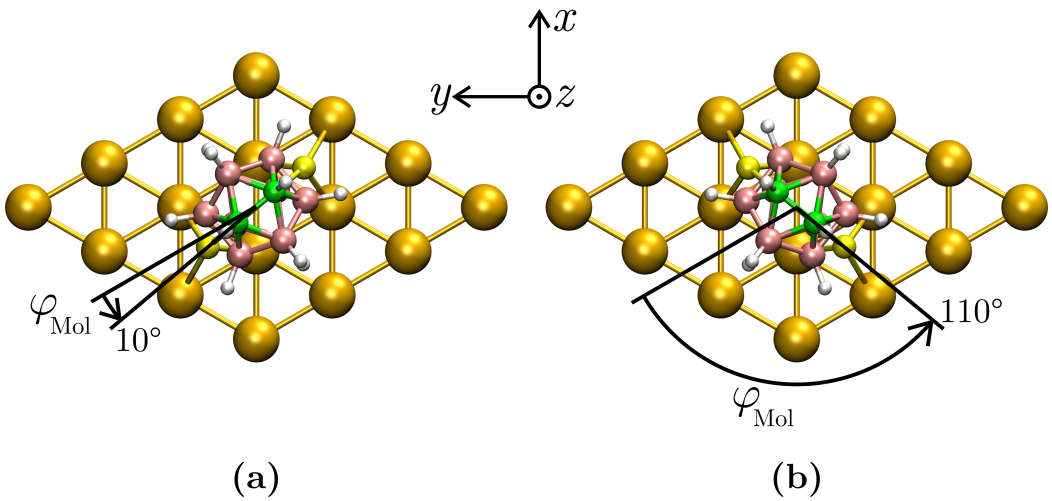

Figure 3.3: Azimuthal characteristics of relaxed gold-molecule junctions. The top views of the optimised geometries of the gold-carboranedithiol junctions with the converged azimuthal angle φ_{Mol} close to **(a)** 10° and **(b)** 110°.

3.3.2 Polar orientation

In this part, we deal with the influence of the polar orientation of the adsorbed molecule on the final junction geometries. We define the polar (tilt) angle θ_{Mol} as the angle between the main rotation axis of the molecule and the axis of the surface normal (Fig. 3.2(b)). For each of the 26 relaxed structures optimised in the part 3.3.1, we tilt the respective molecule around the line connecting both S atoms to achieve the angle θ_{Mol} in the range of 0 to 70° in steps of 10°. As a result, we generate 104 initial conformations (13 azimuthal × 8 polar orientations) for both the B-bonded and the C-bonded isomer (a total of 208 conformations) which we subject to further structural relaxation.

The vertically adsorbed structures of carboranedithiols on the Au surface are local minima in the geometry relaxations, but when we tilt the molecule, we find other and more stable junction geometries. As we already mention at the beginning of Sec. iii, the tilting of the molecular dipoles to the surface is one way to enhance the stability of the substrate-molecule junction [22, 24]. This also applies to our slab super-cell calculations in which, due to the PBCs in the x and the y directions, the resulting dipole layer composed of covalently bonded carboranedithiol building blocks is destabilised by the intermolecular dipole-dipole interactions, i.e. the electrostatic repulsion interactions between the dipole of the unit cell and that of the adjacent images. Therefore, the monolayer of vertically oriented molecules representing a two-dimensional arrangement of parallel dipoles aligned along the surface normal is the most unfavourable interface structure from an energy standpoint. By converting the molecular orientations to horizontal positions in which the dipole moments of the carboranedithiols are parallel to the Au surface, the intensity of the dipole-dipole repulsions is minimised, making the resulting dipole array the most stable coverage of the substrate. This geometry of the similar type of SAM is considered in a computational study of carboranethiols on

the Au(111) wafer reported by Mete et al. [80].

Relaxed junction geometries. Intuitively, as the angle θ_{Mol} increases from the vertical orientation, one can expect the total energy to decrease at first due to the attenuation of the dipole-dipole repulsion interactions. Eventually, for sufficiently high polar angles, the Au atoms repel the carborane cage when it comes too close to the metal surface and the resulting gold-molecule junction approaches its energy minimum. We confirm this overall picture by atomistic simulations, although with two important caveats. First, simulations show that the angle θ_{Mol} is a rather soft degree of freedom: there are stable configurations with polar angles between $\theta_{\text{Mol}} \sim 40$ to $\sim 60°$ within the energy range of ~ 0.2 eV (see Fig. 3.4(B) and (C)). Second, the tilting of carboranedithiols is accompanied in many cases with significant deformation of the top surface Au layer (see Fig. 3.4(B_{min}) and (C_{min})). For large tilt angles, Au surface atoms bonded to the S linker atoms are pulled out of the top surface layer during the geometry relaxation. As we discuss below, these distortions of the Au layer strongly affect the total energy and the dipole of the junction.

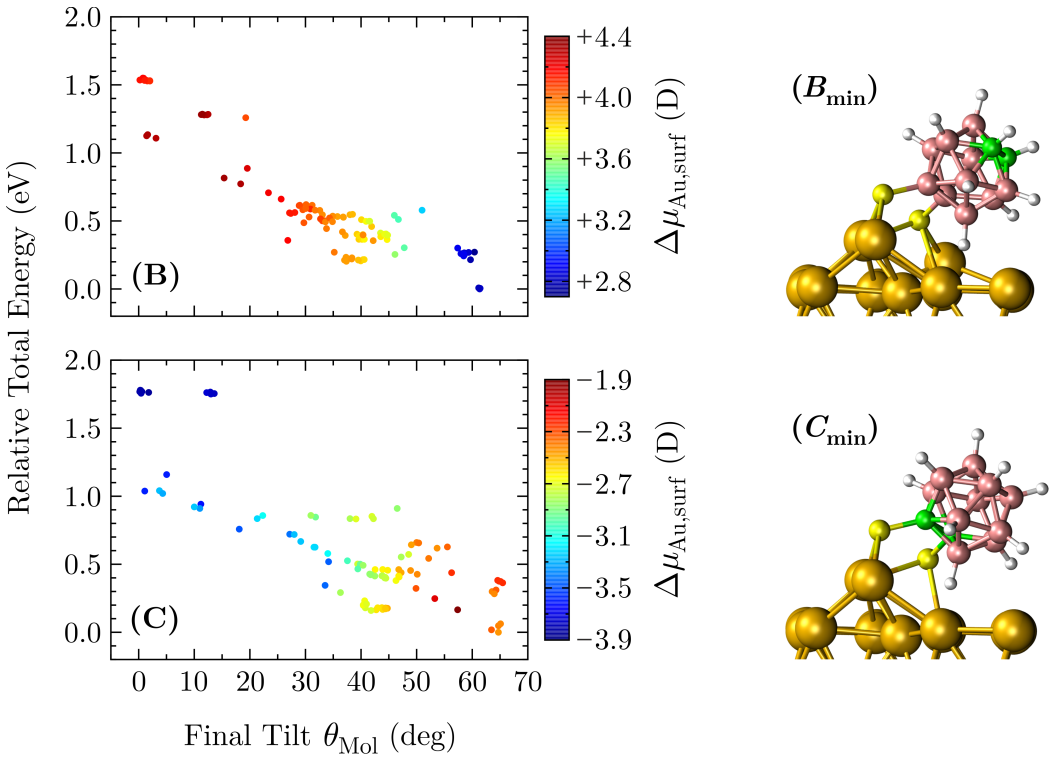

Figure 3.4: Polar characteristics of relaxed gold-molecule junctions. Relative total energy of the relaxed geometries and change of the dipole moment of the Au(111) slab as functions of the final molecular tilt angle for a series of conformations of **(B)** the B-bonded and **(C)** the C-bonded junctions. Total energies of data points: **(B)** $E_{\text{Au-Mol}} - E_{\text{Au-Mol}}(B_{\text{min}})$, and **(C)** $E_{\text{Au-Mol}} - E_{\text{Au-Mol}}(C_{\text{min}})$. To the right of each set of points is the side view of the most stable conformation of **(B_{min})** the B-bonded and **(C_{min})** the C-bonded junctions.

In Fig. 3.4, we summarise the calculated total energies and dipole moments of the gold-carboranedithiol junctions composed of the B-bonded (top (B) panel) and the C-bonded adsorbates (bottom (C) panel). Each data point corresponds to the relaxed structure obtained by the sampling of φ_{Mol} and θ_{Mol}. On the horizontal axis, we show the relaxed values of θ_{Mol}. On the vertical axis, for both the set of B-bonded and the set of C-bonded junctions, we express the total energy of each final geometry ($E_{\text{Au-Mol}}$)

with respect to the energy of the corresponding most stable conformation. We denote these conformations as B_{min} and C_{min}, respectively, and depict their structures on the respective panels of Fig. 3.4. In addition, in each data set, we use the colour bar to introduce the results of the dipole moment change of the gold surface, $\Delta\mu_{\text{Au,surf}}$, caused by the carboranedithiol adsorption. We define $\Delta\mu_{\text{Au,surf}}$ as the difference between the junction dipole $\mu_{\text{Au-Mol}}$ and the dipole of the bare Au surface, μ_{Au}:

$$\Delta\mu_{\text{Au,surf}} = \mu_{\text{Au-Mol}} - \mu_{\text{Au}}\,, \tag{3.2}$$

where use $\mu_{\text{Au}} = -4.722\ D$, calculated for the relaxed slab of the Au(111) wafer. From the number of generated initial conformations (see above), we know that each panel contains 104 data points.

The results of Fig. 3.4 show that junctions with the carboranedithiol adsorbate grafted onto the Au surface more or less vertically ($\theta_{\text{Mol}} < 20°$) are more energy demanding geometries than those with larger tilt angles. Regarding the colour scale, the effect of the adsorbed molecule on the dipole of the optimised junction follows the expected behaviour. Specifically, when the angle θ_{Mol} is larger, the magnitude of $\mu_{\text{Mol\{jcn\}}}$ is smaller (remember that we are interested in the vertical component, which is the only relevant component for us, so $\mu_{\text{Mol\{jcn\}}} \parallel z$-axis), leading to a decrease in the magnitude of $\Delta\mu_{\text{Au,surf}}$ ($\Delta\mu_{\text{Au,surf}} \propto \mu_{\text{Mol\{jcn\}}}$). Moreover, since the orientation of $\mu_{\text{Mol\{jcn\}}}$ is opposite for the B- and the C-functionalised carborane cages, their contributions to the total dipole $\mu_{\text{Au-Mol}}$ as a function of the molecular tilt go in opposite directions [111].

In terms of the specific orientations of the intrinsic molecular dipoles relative to the substrate, the dipoles of the B-bonded and the C-bonded carboranedithiol adsorbates point away from the Au surface ($\mu_{\text{Mol\{jcn\}}} > 0$) and towards it ($\mu_{\text{Mol\{jcn\}}} < 0$), respectively. Thus, as the final angle θ_{Mol} increases in Fig. 3.4, the values of $\Delta\mu_{\text{Au,surf}}$ are less positive for the B-bonded junctions (top (B) panel) or less negative for the C-bonded junctions (top (C) panel).

Atomic rearrangement of top gold layer. In addition to the chemisorption of the S atoms near hollow sites on the Au slab and the larger tilting of the chemisorbed molecules, the atomic rearrangement of the top surface Au layer also contributes to the path to more stable junction geometries. In many simulations, as mentioned above, we observe the extraction of Au surface atoms due to the bonding interactions with the sulphur anchoring groups, especially for high values of θ_{Mol}. It is well known that unsaturated thiol groups interact strongly with Au and can induce important structural changes in the Au surface [70, 71]. Our simulations show instances where one, two or even three Au atoms bonded to molecular S groups are lifted during the geometry relaxations by $\sim$1.0 $\AA$ or more above the metal surface. These atomic rearrangements stabilise the junction, resulting in a lowering of the total energy. Concurrently, regardless of the type of the adsorbed carboranedithiol isomer, the extraction of Au surface atoms always shifts the junction dipole $\mu_{\text{Au-Mol}}$ towards more positive values. With respect to Eq. 3.1, these geometric changes reflect in the resulting dipole $\mu_{\text{Au-Mol}}$ via the interfacial term $\mu_{\text{Au-S}}$ because they occur at the gold-molecule interface. Their effect can be enhanced or attenuated by the molecular dipole $\mu_{\text{mol\{jcn\}}}$ depending on whether the B-bonded or the C-bonded isomer, respectively, is adsorbed.

3.3.3 Au surface asperities

For a deeper study of impacts of surface roughness on the interface properties, we investigate the adsorption of the B-bonded carboranedithiol molecule on the Au(111)

slab which has surface asperities in the form of adsorbed adatom(s). We consider either one or three Au adatoms adsorbed on fcc or hcp hollow sites of the top surface Au layer (see Fig. 3.5(a) or (b), respectively) as structural components of the gold-molecule junctions. We prepare the initial geometries by placing the B-bonded carboranedithiol molecule partially above the Au adatom(s). In particular, we place one S atom above the Au adatom(s) and the other one above the Au(111) surface (Fig. 3.6(a) and (b)), giving the initial angle $\theta_{\mathrm{Mol}} = 38.45°$. We rotate the molecule around the centre of the Au adatom or the Au trimer in the range of φ_{Mol} from 0 to 120° in steps of 10° (see Fig. 3.5(c) or (d), respectively). In this way, for each type of the Au adsorbate geometry, we generate 13 initial conformations on hcp and another 13 on fcc sites, which we subject to the structural relaxation process.

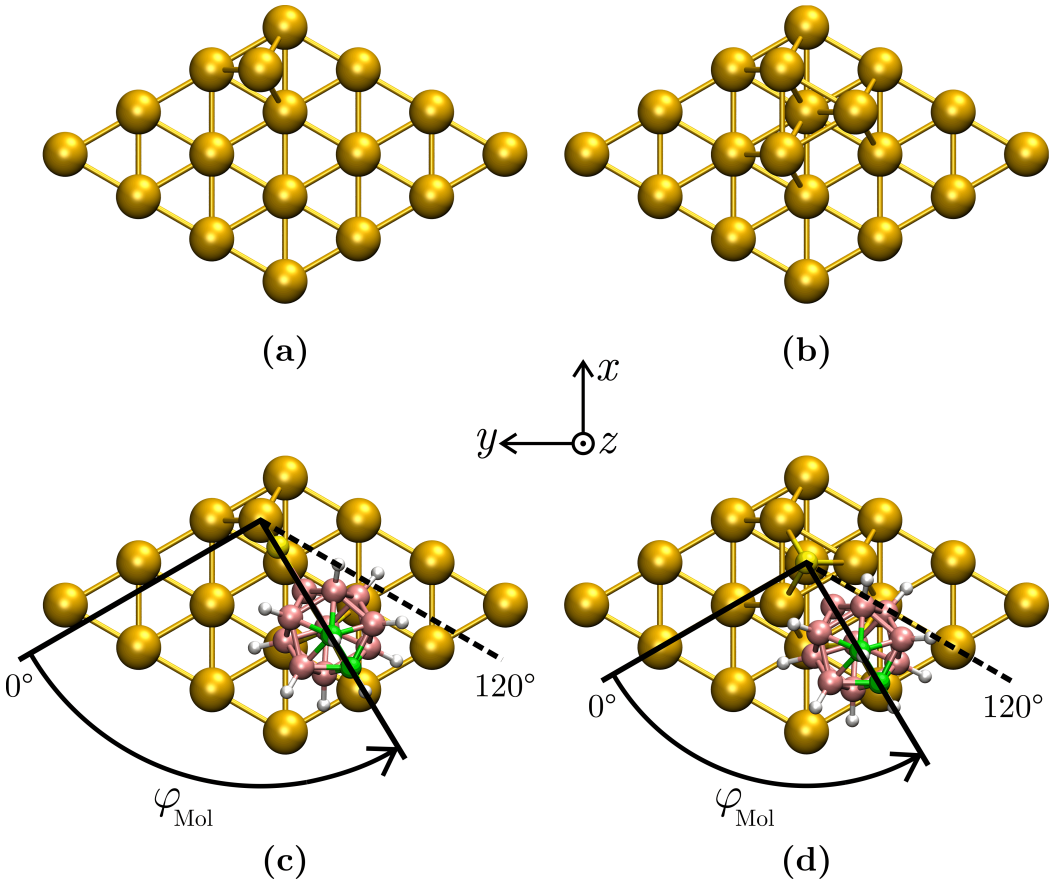

Figure 3.5: Au surface asperities and initial azimuthal orientations on them. The top views of the top surface Au layer of the (4×4) slab of the Au(111) wafer. On fcc hollow sites of the wafer, the Au adsorbate geometries in the form of **(a)** the Au adatom or **(b)** the Au trimer are located. By sampling the azimuthal angle φ_{Mol} between 0 and 120° around the centre of **(c)** the Au adatom or **(d)** the Au trimer, the initial geometries of the junction between the B-bonded carboranedithiol isomer and the gold are generated.

Simulations of the gold-molecule interfaces involving Au adsorbates are in line with the findings on the flat (111) surface. In particular, the substantial initial tilt of the carboranedithiol molecule causes the structural relaxation of the junction to be accompanied by the substantial atomic rearrangement of the top surface Au layer and the lowering of the total energy. Moreover, as on the flat gold surface, the geometry of the interface is controlled by Au–S interactions in which the S atom closer to the (111) surface tends to adsorb close to the hollow site. However, the final geometries and the total energies of the relaxed junctions are strongly influenced by the coordination of

the other S atom which is located above the Au adatom or the Au trimer before the start of the simulation.

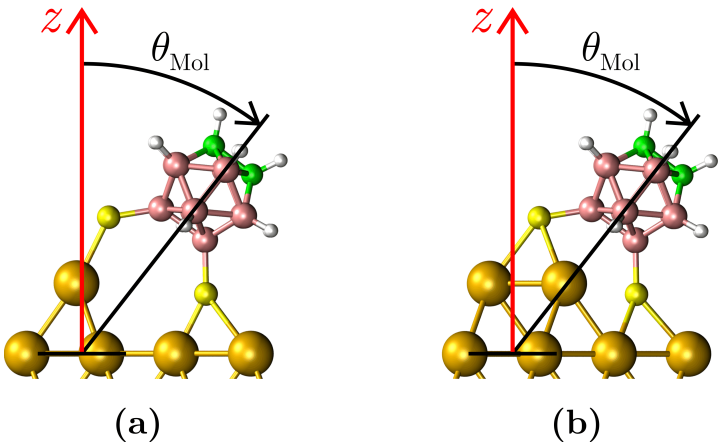

Figure 3.6: Initial polar orientations on Au surface asperities. The side views of the initial geometries of the B-bonded junction with **(a)** the Au adatom or **(b)** the Au trimer, both of which provide the initial tilt angle $\theta_{\mathrm{Mol}} = 38.45°$.

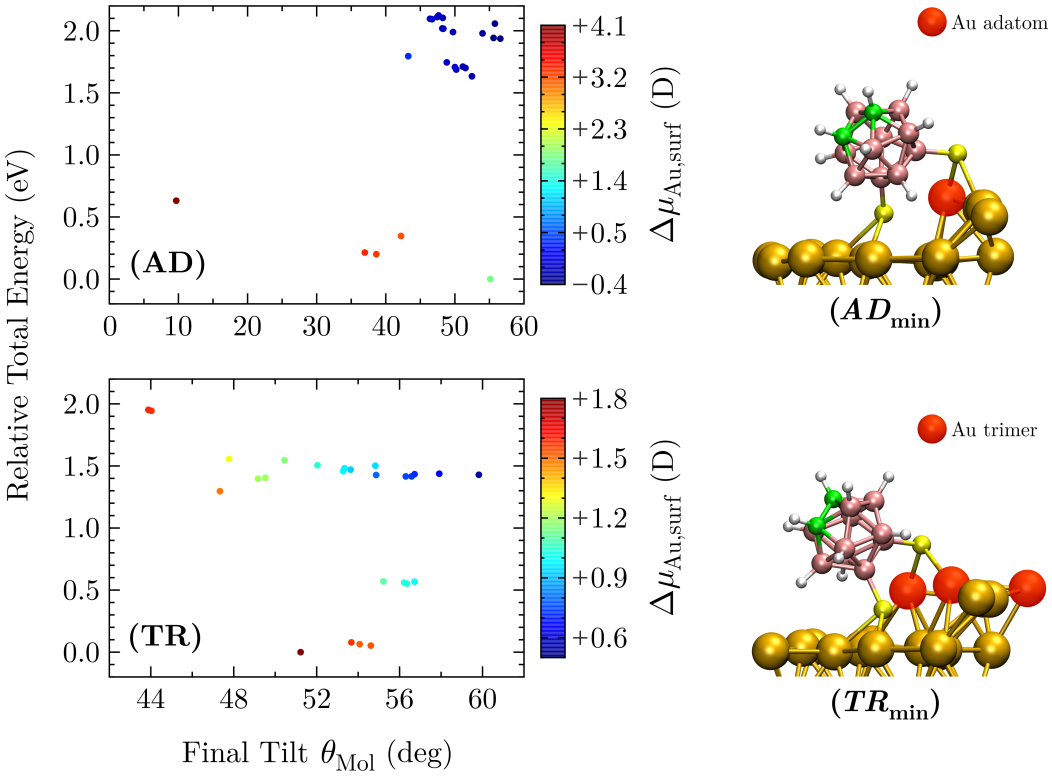

Figure 3.7: Relaxed polar characteristics with Au surface asperities. Relative total energy of the relaxed B-bonded junctions and change of the dipole moment of the Au(111) slab with Au adstructures plotted as functions of the final molecular tilt angle. The quantities relate to a series of conformations with **(AD)** the Au adatom and **(TR)** the Au trimer. Total energies of data points: **(AD)** $E_{\text{Au-Mol}} - E_{\text{Au-Mol}}(AD_{\text{min}})$, and **(TR)** $E_{\text{Au-Mol}} - E_{\text{Au-Mol}}(TR_{\text{min}})$. To the right of each set of points is the side view of the most stable B-bonded junction with $\boldsymbol{(AD_{\text{min}})}$ the Au adatom and $\boldsymbol{(TR_{\text{min}})}$ the Au trimer.

In Fig. 3.7(AD) and (TR), we summarise the calculated properties of the B-bonded junctions in which the carboranedithiol molecule is adsorbed above the Au adatom or the Au trimer, respectively. For both scatter plots, we express the total energy of

each relaxed junction in the same way as in the above part 3.3.2, i.e. with respect to the total energy of the corresponding most stable conformation. For the series of junctions with the Au adatom or the Au trimer, we label the most energy-favourable conformations as AD_{min} or TR_{min}, respectively, and depict their patterns to the right of the relevant plots. Regardless of whether the Au adsorbates are consisted of one or three adatoms, the lowest-energy structures have the S atom bonded to two Au surface atoms in a bridge-like configuration. On the contrary, whenever the S atom is bonded to one Au atom only, the energy of the final geometry is significantly higher. As for the Au trimer-based structures only, we do not find any geometries in which the S atom is bonded on the hollow site above the Au adsorbate. During the relaxation, there is considerable steric repulsion between the substrate and the carborane cage, leading to the trimer deformation and extraction of metal atoms from the Au surface layer. From the point of view of all junctions, we do not observe any differences between the adsorption of the Au adstructures on hcp or fcc sites.

3.4 Electronic properties

For the rest of this chapter, we are interested in two gold-molecule junctions composed of the vertically adsorbed molecules, one for the B-bonded and the other for the C-bonded isomer. For these conformations, we expect the greatest changes in the electronic structure of the substrate because the molecular dipole is parallel to the surface normal. In this section, we investigate the influence of the molecular dipole on the charge density distribution at the interface (part 3.4.1) and on the electrostatic potential energy above the Au surface (part 3.4.3). The last mentioned quantity is related to the work function change of gold, the value of which is the main indicator of the ability of the adsorbate to modify the electrostatic features of the metal.

3.4.1 Charge density

When adsorbing the S-functionalised carborane cage with the upright geometry, we observe only slight structural relaxations of both the molecule and the top surface Au layer. However, the formation of Au-S bonds between these subsystems has a significant impact on the charge density in the interface region. To investigate the details of the charge density rearrangement upon the carboranedithiol adsorption, we define the plane-averaged charge density difference, $\rho_{\text{diff}}(z)$, which reads:

$$\rho_{\text{diff}}(z) = \rho_{\text{Au-Mol}}(z) - \left[\rho_{\text{Mol}\{\text{jcn}\}}(z) + \rho_{\text{Au}\{\text{jcn}\}}(z)\right] . \tag{3.3}$$

Here, on the right-hand side, $\rho_{\text{Au-Mol}}(z)$, $\rho_{\text{Mol}\{\text{jcn}\}}(z)$, and $\rho_{\text{Au}\{\text{jcn}\}}(z)$, are the charge densities of the gold–molecule junction, the isolated molecule, and the bare Au surface, respectively, in the basis set and the atomic arrangement of the junction. All quantities in Eq. 3.3 are averaged over the x and the y components in the unit cell [112–114].

In Fig. 3.8, we show the calculated profiles of $\rho_{\text{diff}}(z)$ for the B-bonded (panel (a), blue curve) and the C-bonded junctions (panel (b), red curve). Positive and negative values of $\rho_{\text{diff}}(z)$ correspond to electron accumulation and electron depletion, respectively, upon the carboranedithiol adsorption. This is because we calculate each type of charge density, $\rho(z)$, as the difference between the corresponding types of the electron, $\rho_{\text{el}}(z)$, and the ionic charge density, $\rho_{\text{ion}}(z)$. We use the SIESTA sign convention in which $\rho_{\text{el}}(z)$ is positive and $\rho_{\text{ion}}(z)$ is negative, so $\rho(z) = \rho_{\text{el}}(z) - \rho_{\text{ion}}(z)$.

As expected, the $\rho_{\text{diff}}(z)$ profile integrates to zero. Fig. 3.8 shows oscillations around zero with the highest amplitudes in the Au-S region. In particular, electrons are accumulated in the S atoms (at the surface-normal distance of $\sim$14 $\AA$), while the region

close to the Au surface (at the distance of ∼12 *Å*) is depleted. These rearrangements are consistent with the changes in Mulliken populations. Specifically, upon the B-bonded carboranedithiol adsorption, the orbital population of each S atom increases by ∼0.27 $|e|$, whereas the sum of orbital populations of each triplet of contact Au atoms bonded to S atoms decrease by ∼0.26 $|e|$. The corresponding sum over all Au atoms of the right (top) surface layer gives the population decrease of ∼0.56 $|e|$. Regarding the adsorption of the C-bonded isomer, the orbital populations of each S atom and the top surface Au layer change by ∼+0.30 and ∼−0.60 $|e|$, respectively; the sum over each triplet of contact Au atoms decrease by ∼0.21 $|e|$.

The total increase in the orbital populations of the both S atoms of ∼0.54 and ∼0.60 $|e|$ upon the B-bonded and the C-bonded junction formations, respectively, coincides with the higher positive oscillation of the red curve at the location of the thiol linker groups compared to the blue one. On the other hand, in the immediate vicinity of the top Au layer (∼12 *Å*), the orbital-population decrease of this layer predicts the more negative oscillation of the red curve with respect to the blue one. However, the total decrease in the Mulliken populations of the both contact Au triplets of ∼0.52 and ∼0.42 $|e|$, respectively, tell us that electrons are depleted mainly from the contact Au atoms when the B-bonded molecule is adsorbed, while in the formation of the C-bonded junction, the electron depletion is spread more over the top surface Au layer.

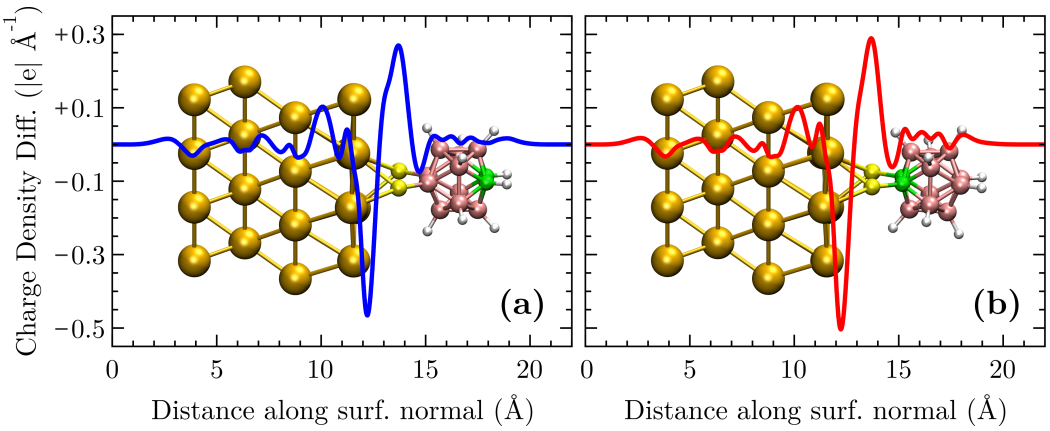

Figure 3.8: Charge density difference of gold-molecule junctions. Plane-averaged charge density difference profiles upon the adsorption of **(a)** the B-bonded and **(b)** the C-bonded carboranedithiol molecules on the Au(111) surface. Blue and red curves correspond to the respective adsorptions, respectively. In each panel, the inset behind the curve introduce the side view of the final relaxed junction.

The charge rearrangement between the molecule and the substrate gives rise to the interfacial dipole $\mu_{\text{Au-S}}$. We numerically calculate the dipole $\mu_{\text{Au-S}}$ according to the relation:

$$\mu_{\text{Au-S}} = -\int_0^{z_{\text{unit}}} \rho_{\text{diff}}(z) z \, \mathrm{d}z \tag{3.4}$$

where z_{unit} is the unit cell size along the z-axis. We introduce the minus sign before the integral due to the SIESTA sign convention included in the density. For the B-bonded and the C-bonded interfaces, we obtain $\mu_{\text{Au-S}} = -2.288$ and -2.455 D, respectively.

In the sense of Eq. 3.4, we can calculate the corresponding dipole moments from the other charge density profiles contained in Eq. 3.3. In Tab. 3.1, we list the values of all dipole moment quantities related to the gold-molecule interface in the B-bonded and the C-bonded junctions. The values satisfy Eq. 3.1.

Table 3.1: Dipole moment quantities related to gold-molecule interface. Calculated values of the dipole moment quantities related to the gold-molecule interface in the B-bonded and the C-bonded junctions: the dipole moment of the gold-molecule junction, $\mu_{\text{Au-Mol}}$, the dipole moments of the molecular adsorbate, $\mu_{\text{Mol\{jcn\}}}$, and the Au substrate in the basis set of the junction, $\mu_{\text{Au\{jcn\}}}$, and the dipole moment of the gold-molecule interface, $\mu_{\text{Au-S}}$.

junction	$\mu_{\text{Au-Mol}}$ (D)	$\mu_{\text{Mol\{jcn\}}}$ (D)	$\mu_{\text{Au\{jcn\}}}$ (D)	$\mu_{\text{Au-S}}$ (D)
B-bonded	-0.557	$+6.134$	-4.403	-2.288
C-bonded	-8.569	-1.705	-4.409	-2.455

3.4.2 Theoretical note: Fermi and vacuum levels in SIESTA

In Eq. 1.27, the second term, $\sum_\alpha \hat{V}^\alpha_{\text{loc}}(\mathbf{r})$, and the fourth term, $\mathcal{V}_{\text{H}}(\mathbf{r})$, represent the valence-ionic and the valence-electronic potential contributions, respectively, together forming the total valence electrostatic potential, $\mathcal{V}_{\text{El}}(\mathbf{r})$. Because of the PBCs, there is a need to screen the long-range effect of $\hat{V}_{\text{loc}}(\mathbf{r})$, namely by introducing the atomic electronic potential, $\mathcal{V}_{\text{at}}(\mathbf{r})$, created by the atomic electron density, $\rho_{\text{at}}(\mathbf{r})$, i.e. the sum of the valence electron densities: $\sum_\alpha \rho^\alpha_{\text{at}}(\mathbf{r})$, occupying the atom-centred basis functions according to the valence atomic charges. In this way, one gets the screened "neutral-atom" potential: $\mathcal{V}_{\text{NA}}(\mathbf{r}) = \sum_\alpha(\hat{V}^\alpha_{\text{loc}}(\mathbf{r}) + \mathcal{V}^\alpha_{\text{at}}(\mathbf{r}))$, as the total valence electrostatic potential which is zero at $r \geq r_{\text{C}}$ and describes, for example, a solid in the form of undistorted bulk or a molecule without chemical bonds. In terms of the screened potential, $\mathcal{V}_{\text{El}}(\mathbf{r}) = \mathcal{V}_{\text{NA}}(\mathbf{r}) + \delta\mathcal{V}_{\text{H}}(\mathbf{r})$, where $\delta\mathcal{V}_{\text{H}}(\mathbf{r})$ is the Hartree deformation potential stemming from the deformation electron density, $\delta\rho(\mathbf{r}) = \rho(\mathbf{r}) - \rho_{\text{at}}(\mathbf{r})$, i.e. the distorted density induced by the bond formation or the surface formation [39, 115, 116].

Since $\hat{V}_{\text{loc}}(\mathbf{r}) = \mathcal{V}_{\text{loc}}(\mathbf{r})\hat{I}$, the total electrostatic potential energy, $V_{\text{El}}(\mathbf{r})$, is the explicit functional of the electron density: $V_{\text{El}}(\mathbf{r}) = \int \mathcal{V}_{\text{El}}(\mathbf{r})\,\rho(\mathbf{r})\,\mathrm{d}\mathbf{r}$. The same holds for the neutral-atom potential energy, $V_{\text{NA}}(\mathbf{r})$, and for the distorted potential energy, $\delta V_{\text{H}}(\mathbf{r})$. For the study of wafers, substrate-adsorbate junctions, and other structures with the xy-plane periodicity, one employs the plane-averaged potential energy profiles: $V_{\text{El}}(z)$, $V_{\text{NA}}(z)$, $\delta V_{\text{H}}(z)$, as functions of z-coordinates. However, these profiles include microscopic oscillations caused by the atomic structure along the surface normal. To smooth out these oscillations without affecting the potential-energy steps across the interface, one introduces the nano-smoothing procedure that filters out the oscillations with a Fourier transform corresponding to the interlayer distance (to filter out that periodicity), resulting in the macro-averaged profiles [117] with the values in two well distinguished regions, namely in the vacuum: $\langle V_{\text{El}}\rangle_{\text{vac}}$, $\langle V_{\text{NA}}\rangle_{\text{vac}}$, $\langle \delta V_{\text{H}}\rangle_{\text{vac}}$, and in the middle of the slab: $\langle V_{\text{El}}\rangle_{\text{slab}}$, $\langle V_{\text{NA}}\rangle_{\text{slab}}$, $\langle \delta V_{\text{H}}\rangle_{\text{slab}}$. Due to the cutoff radius, $\langle V_{\text{NA}}\rangle_{\text{vac}} = 0$, and inside a sufficiently thick slab, $\langle V_{\text{NA}}\rangle_{\text{slab}} = \langle V_{\text{El}}\rangle_{\text{bulk}}$, where $\langle V_{\text{El}}\rangle_{\text{bulk}}$ is the electrostatic potential energy of the bulk [116]. In SIESTA, the unit-cell average of $\delta V_{\text{H}}(z)$, denoted as $\langle \delta V_{\text{H}}\rangle_{\text{unit}}$, is zero, defining the zero-energy reference with respect to which all the KS eigenvalues are related [115].

A prominent feature of metal and semiconductor wafers is the line-up term, $\Delta\langle \delta V_{\text{H}}\rangle$:

$$\Delta\langle \delta V_{\text{H}}\rangle = \underbrace{\left(\langle V_{\text{El}}\rangle_{\text{vac}} - \langle V_{\text{NA}}\rangle_{\text{vac}}\right)}_{=\langle \delta V_{\text{H}}\rangle_{\text{vac}}} - \underbrace{\left(\langle V_{\text{El}}\rangle_{\text{slab}} - \langle V_{\text{NA}}\rangle_{\text{slab}}\right)}_{=\langle \delta V_{\text{H}}\rangle_{\text{slab}}}, \tag{3.5}$$

which accounts for the interfacial charge transfer and the stabilisation of the surface-dipole layer. In the case of bare surfaces, $\Delta\langle \delta V_{\text{H}}\rangle > 0$, making the line-up term a certain energy barrier for the "flow out" of electrons from the wafer. Going from the

SIESTA reference to the bulk reference, i.e. from $\langle \delta V_{\mathrm{H}} \rangle_{\mathrm{unit}} \equiv 0$ to $\langle V_{\mathrm{El}} \rangle_{\mathrm{bulk}} \equiv 0$, one gets the vacuum level and the Fermi level of the xy-plane periodic system:

$$E_{\mathrm{vac}} = \Delta \langle \delta V_{\mathrm{H}} \rangle - \langle V_{\mathrm{El}} \rangle_{\mathrm{bulk}} \tag{3.6}$$

$$E_{\mathrm{F}} = E_{\mathrm{F}}^{\mathrm{SIESTA}} - \langle V_{\mathrm{El}} \rangle_{\mathrm{bulk}} \tag{3.7}$$

where $E_{\mathrm{F}}^{\mathrm{SIESTA}}$ is the Fermi level with respect to the SIESTA reference.

3.4.3 Electrostatic potential energy

To investigate the effect of the molecular dipole on the electrostatic features of the surface, in Fig. 3.9(a) and (c), we plot the plane-averaged profiles of the electrostatic potential energy across the bare Au(111) wafer (green curve) and across the B-bonded (panel (a), blue curve) and the C-bonded junctions (panel (c), red curve) as the functions of the distance along the surface normal. In both of these panels, the green curve is the same. When going from the electrostatic to the distorted potential energy (defined in Sec. 1.6), the deep wells around the gold nuclei are eliminated, making the relative differences between the green and the blue/red curves more visible (see Fig. 3.9(b)/(d)).

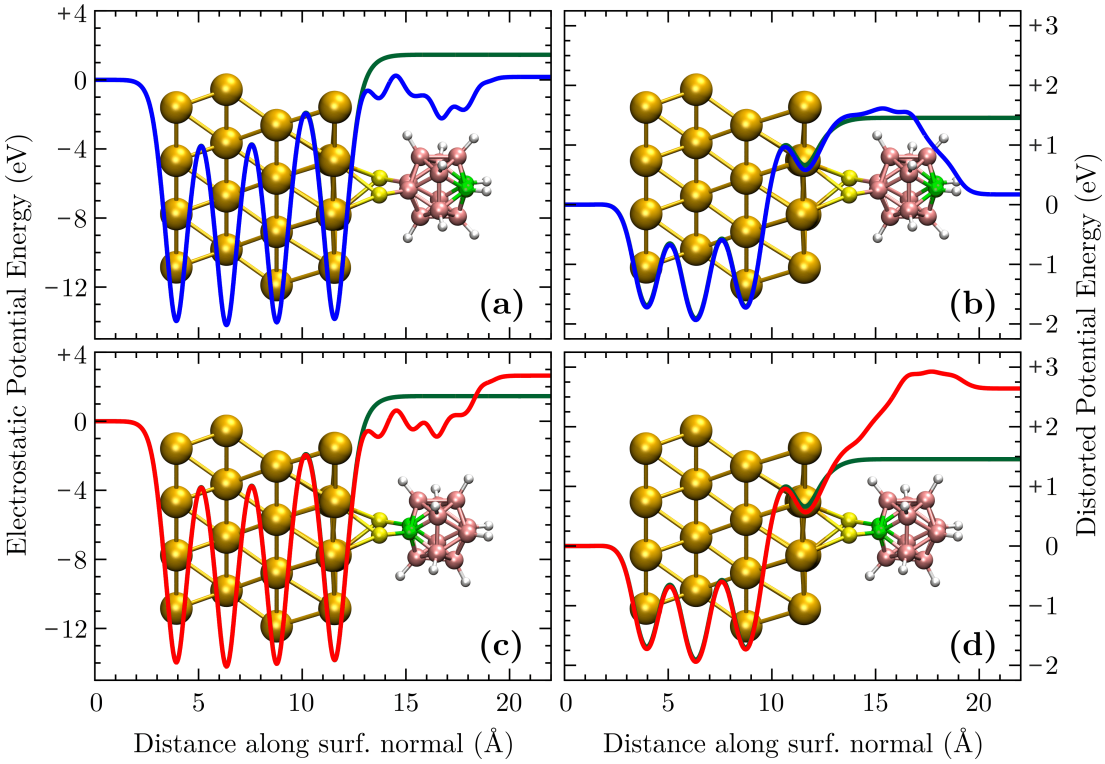

Figure 3.9: Electrostatic potential energy of gold-molecule junctions. On the left-hand side, there are the plane-averaged electrostatic potential energy profiles across **(a)** the B-bonded and **(c)** the C-bonded junctions. On the right-hand side, there are the plane-averaged distorted potential energies across **(b)** the B-bonded and **(d)** the C-bonded junctions. Green, blue, and red curves belong to the bare Au(111) slab, the B-bonded, and the C-bonded junctions, respectively. In each panel, the inset behind the curve introduce the side view of the final relaxed junction.

In each panel of Fig. 3.9, we can clearly distinguish four main regions along the surface-normal direction. Up to the surface-normal distance of ∼2 *Å*, there is the left

(bottom) vacuum region where all potential profiles acquire the reference asymptotic zero value. Since the Au surface adjacent to this vacuum layer is not perturbed by the carboranedithiol adsorption, the potential-energy curves quickly converge away from the wafer. In the second region from ∼4 to ∼9 *Å*, the oscillations in the potential energies are regular, giving the curves the bulk-like behaviour. Then, from ∼10 to ∼14 *Å* for the clean Au wafer and from ∼10 to ∼19 *Å* for the gold-molecule junctions, the potential-energy curves pass through the interface region with significant variations caused by the relaxation of the right (top) surface Au layer and the formation of the gold-molecule interface. Finally, beyond ∼14 *Å* for the bare gold and beyond ∼19 *Å* for the junctions, there is the right (top) vacuum region where each potential profile converges to its own asymptotic value.

Deep inside the metal, the electronic structure is not affected by the surface or the interface effects, making all three potential profiles coincident. In the interface region (with the onset at ∼10 *Å*), the potential differences start to appear between the carboranedithiol-terminated junctions and the clean surface, as well as between both junction structures. To the right of (above) the surface, the three potential profiles level out to different plateaus, illustrating the effect of the carboranedithiol-based dipole layer on the proceeding of the electrostatic potential energy. The distance between the outer right plateaus of the blue/red and the green curves characterises the Au-surface potential-energy step, $\Delta U_{\mathrm{Au,surf}}$, across the carboranedithiol layer:

$$\Delta U_{\mathrm{Au,surf}} = \langle V_{\mathrm{El}} \rangle_{\mathrm{vac}}^{\mathrm{jcn}} - \langle V_{\mathrm{El}} \rangle_{\mathrm{vac}}^{\mathrm{Au}} = \langle \delta V_{\mathrm{H}} \rangle_{\mathrm{vac}}^{\mathrm{jcn}} - \langle \delta V_{\mathrm{H}} \rangle_{\mathrm{vac}}^{\mathrm{Au}} = -\frac{e\,(\Delta\mu_{\mathrm{Au,surf}})}{\epsilon_0\,(\Omega_{\mathrm{Au}})}\,. \tag{3.8}$$

Here, after the first equal sign, there are the nano-smoothed electrostatic potential energies in the top vacuum layer for the junction and for the bare Au wafer; after the second equal sign, there are the corresponding nano-smoothed distorted potential energies; the term on the right-hand side is the analogy of Eq. 3 where $\Omega_{\mathrm{Au}} = \sim 122$ $Å^2$ corresponds the size of the Au surface taken by one carboranedithiol molecule and $\Delta\mu_{\mathrm{Au,surf}}$ is the dipole change defined by Eq. 3.2.

Since the Au(111) slab is the metal, its band structure is not affected by the dipole layer adsorption, making $\Delta U_{\mathrm{Au,surf}} = \Delta\Phi_{\mathrm{Au}}$, where $\Delta\Phi_{\mathrm{Au}}$ is the work function change of the gold surface (compare with Eq. 4). By means of Eq. 3.5, 3.6, 3.7, and 2, we obtain the line-up term, $\Delta\langle\delta V_{\mathrm{H}}\rangle$, the vacuum level, E_{vac}, the Fermi level, E_{F}, and the work function, Φ, respectively, for the bare Au(111) wafer, the B-bonded and the C-bonded gold-carboranedithiol junctions. In Tab. 3.2, we list the calculated values of all these quantities with respect to the bulk reference, i.e. $\langle V_{\mathrm{El}} \rangle_{\mathrm{bulk}} \equiv 0$.

Table 3.2: Electrostatic-potential features accompanying adsorption on gold. Calculated values of the electrostatic-potential quantities with respect to the bulk reference describing the bare Au(111) wafer, the B-bonded and the C-bonded junctions: the line-up term, $\Delta\langle\delta V_{\mathrm{H}}\rangle$ (eV), the vacuum level, E_{vac} (eV), the Fermi level, E_{F} (eV), the surface work function, Φ (eV), and the work function change of the gold substrate, $\Delta\Phi_{\mathrm{Au}}$ (eV). We employ $\langle V_{\mathrm{El}} \rangle_{\mathrm{bulk}} = -7.328\ eV$.

	$\Delta\langle\delta V_{\mathrm{H}}\rangle$	E_{vac}	E_{F}	Φ	$\Delta\Phi_{\mathrm{Au}}$
Au(111)	+2.651	9.979	5.180	4.798	/
B-bonded	+1.367	8.695	5.180	3.515	−1.284
C-bonded	+3.837	11.164	5.180	5.984	+1.186

Depending on which chemical species in the cage-like backbone the S linkers are attached to, the work function of the substrate can be shifted by ∼1 *eV* in either

direction compared to the clean surface. Specifically, the B-bonded isomer reduces the work function of the Au(111) wafer by 1.284 eV, while the C-bonded isomer increases it by 1.186 eV. Therefore, upon the carboranedithiol adsorption, the range of changes in the electrostatic potential energy above the Au surface is almost 2.5 eV. These results are consistent with the experimental values obtained by Kelvin Probe Force Microscopy measurements of the same S-functionalised carborane-based isomers adsorbed on gold [32] or silver [33, 37]. When using $\mu_{\mathrm{Au}} = -4.722\ D$ for the relaxed surface of the bare Au(111) wafer and $\mu_{\mathrm{Au\text{-}Mol}} = -0.557$ or $-8.569\ D$ for the B-bonded or the C-bonded junction, respectively, we get $\Delta\mu_{\mathrm{Au,surf}} = +4.164$ or $-3.847\ D$, respectively, according to Eq. 3.2. These surface-dipole changes meet Eq. 3.8, leading to the values of $\Delta\Phi_{\mathrm{Au}}$ listed in Tab. 3.2.

3.5 Convergence test with respect to *k*-point sampling

When studying bulk crystals, bare or surface-modified wafers, and other related issues, we deal with systems that are infinite but periodic in the respective dimensions. Based on Bloch's theorem, the electronic-structure calculation of an infinitely large system in the real space can be converted to the electronic-structure calculation of a finite system in the first Brillouin zone of the reciprocal space composed of an infinite number of k-points. In principle, if we know the eigenvalues and the eigenfunctions of the Hamiltonian at all the k-points in the first Brillouin zone, we can accurately calculate various properties of the periodic system, such as the charge density or the total energy. However, one cannot construct an infinitely dense k-point grid spanning the first Brillouin zone, so a practically available one has to consist of a finite number of k-points. The choice of a sufficiently dense k-point mesh is crucial for the convergence of our results and we discuss it in this section.

To achieve the satisfactory convergence of the junction properties, we calculate the projected density of states (PDOS) of the molecular atomic species (Fig. 3.10) and the plane-averaged profile of the charge density difference (Fig. 3.11) at various densities of the Monkhorst–Pack k-point grid in the direction parallel to the surface.

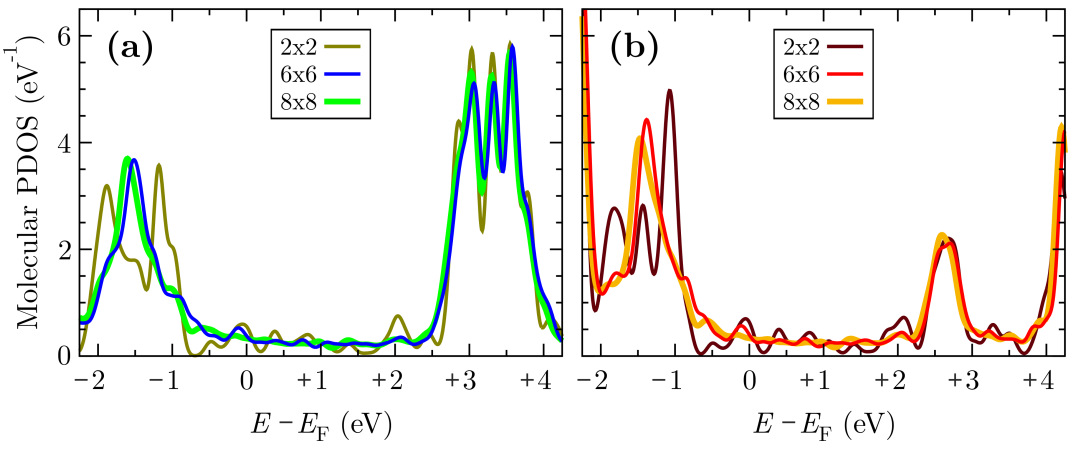

Figure 3.10: Dependence of molecular PDOS on *k*-point density. Comparison of molecular projected densities of states around the HOMO-LUMO gap of **(a)** the B-bonded and **(b)** the C-bonded gold-molecule junctions calculated with different Monkhorst–Pack k-point grids in the direction parallel to the surface. In (a) panel, olive, blue, and green curves are computed with the 2×2, the 6×6, and the 8×8 k-point meshes, respectively. In (b) panel, brown, red, and yellow curves correspond to these meshes, respectively.

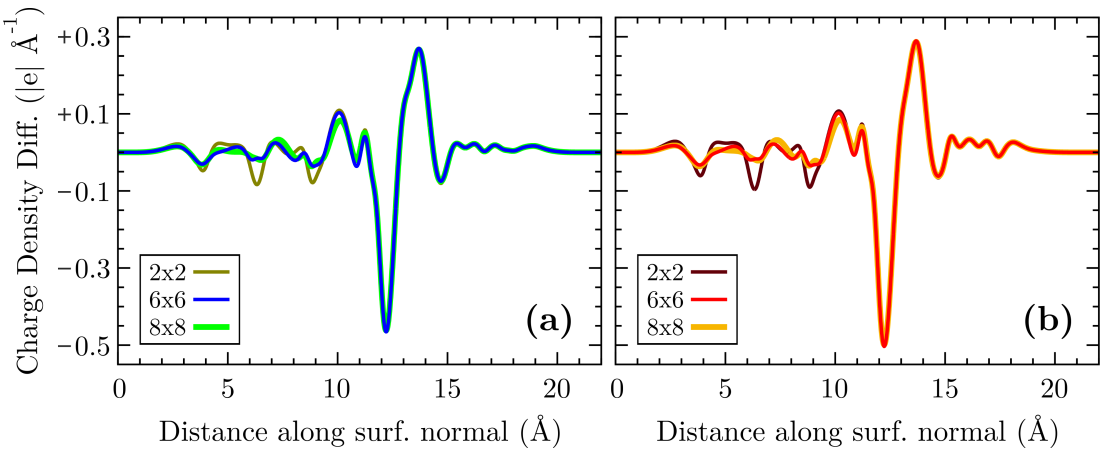

Figure 3.11: Dependence of charge density difference on *k*-point density. Comparison of plane-averaged charge density difference profiles upon the adsorption of **(a)** the B-bonded and **(b)** the C-bonded carboranedithiol molecules on the Au surface calculated with different in-plane k-point grids. In (a) panel, olive, blue, and green curves are computed with the 2×2, the 6×6, and the 8×8 k-point meshes, respectively. In (b) panel, brown, red, and yellow curves correspond to these meshes, respectively.

Regarding Fig. 3.10, we see the HOMO and the LUMO peaks of the molecular PDOS calculated with the 6×6 k-point mesh practically coincide with the same-type peaks obtained at the higher k-point density. The poorer 2×2 k-point grid produces a noticeably different shape of the HOMO peak and a much less smooth profile across the HOMO-LUMO gap. In the case of Fig. 3.11, we can make almost the same conclusion. Specifically, as we increase the density of the k-point grid, the amplitudes of oscillations in the charge density difference profiles inside the Au wafer decrease, while when using the 6×6 grid, this decreasing trend is practically negligible.

In addition, we verify the satisfactory convergence of the electronic structure at the 6×6 k-point density by means of the relative comparisons of the important junction characteristics listed in Tab. 3.3. In particular, we compare the values of the interface dipole $\mu_{\text{Au-S}}$, the binding energy of the junction including corrections to basis-set superposition errors, $E_{\text{B\{jcn\}}}$, and the dipole change $\Delta\mu_{\text{Au,surf}}$. When going from the 6×6 to the 8×8 k-point density, the corresponding quantities change by about 1 to 2 %.

Table 3.3: Convergence of selected junction features with *k*-point density. Calculated values of the selected properties of the B-bonded and the C-bonded gold-molecule junctions with respect to the 2×2, the 6×6, and the 8×8 k-point sampling in the direction parallel to the surface. Specifically, there are the dipole moment of the gold-molecule interface, $\mu_{\text{Au-S}}$ (D), the binding energy of the junction including corrections to basis-set superposition errors, $E_{\text{B\{jcn\}}}$ (eV), and the dipole moment change of the Au surface, $\Delta\mu_{\text{Au,surf}}$ (D).

junction	k-point grid	$\mu_{\text{Au-S}}$	$E_{\text{B\{jcn\}}}$	$\Delta\mu_{\text{Au,surf}}$
B-bonded	2×2	−2.187	−3.564	+4.273
	6×6	−2.288	−3.684	+4.164
	8×8	−2.257	−3.732	+4.199
C-bonded	2×2	−2.334	−3.271	−3.713
	6×6	−2.455	−3.413	−3.847
	8×8	−2.416	−3.469	−3.807

4. Silicon-molecule junctions

In this chapter, we present a new and promising avenue to non-destructively dope silicon, namely through the adsorption of carborane-based molecules possessing a large permanent dipole. As in the third chapter, we consider two positional isomers of the *ortho*-caboranedithiol. We find these S-functionalised carborane cages can either physisorb or chemisorb on the substrate. Chemisorbed structures arise when a S atom of the molecular linker group replaces a surface H atom. We sample a large number of possible adsorption configurations, logically choosing the most representative ones with lowest total energies for further studies. We examine in more detail the formation of selected conformations, we study their mechanical and electronic properties and the band characteristics of their substrate. We find the caboranedithiol adsorption provides a range of changes in electrostatic potential energies above the surface greater than 1 eV. In addition, the adsorption is also reflected in the electronic band states of the silicon substrate itself. Specifically, the large molecular dipole shifts Si features either upwards or downwards, changing the position of the Fermi level in the band gap. Therefore, we achieve a certain level of doping of semiconductor substrate in a non-destructive way, representing a promising new strategy for productions of photovoltaic usable materials.

4.1 Preface

The B-bonded and the C-bonded *ortho*-carboranedithiol molecules with both unsaturated thiol linker groups are, due to their large intrinsic dipoles and possible orientations with respect to the substrate surface, suitable mediators of electron-donating and electron-withdrawing SAMs, respectively, that are capable of non-invasive doping of the semiconductor material via the STD strategy. Each of the two positional isomers can be chemisorbed on the surface of the hydrogen-passivated silicon by a single Si-S bond while the other sulphur atom is saturated with one hydrogen from the top passivation layer (see top right panel of Fig. 4.1 and right panel of Fig. 4.2). However, this means that no final conformation of the silicon-molecule junction achieves the vertical orientation of the carborane cage with respect to the surface. Therefore, in the case of silicon, the range of achievable changes in the surface dipole moment induced by the carboranedithiol adsorption is narrower than in the case of gold. The same, of course, applies to the work function change.

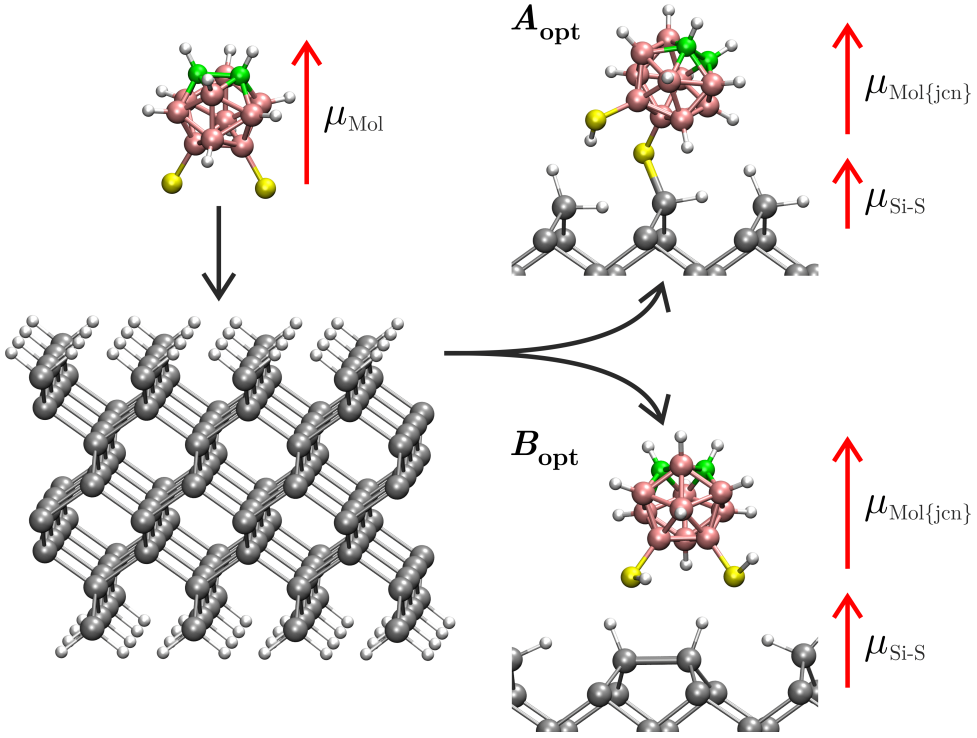

Figure 4.1: Adsorption of B-bonded carboranedithiol on Si(100). The geometric depiction of the adsorption of the unsaturated B-bonded *ortho*-carboranedithiol isomer (top left panel) on the straightened dihydride-terminated Si(100) wafer composed of 8 Si layers (bottom left panel) leading to the formation of the chemisorbed (top right panel) or the physisorbed silicon-molecule junctions (bottom right panel). When achieving the most stable conformations, the final junctions are referred to as A_{opt} or B_{opt}, respectively. Red arrows indicate the dipole moments of the respective structures, namely μ_{Mol}, $\mu_{\mathrm{Mol\{jcn\}}}$, and $\mu_{\mathrm{Si\text{-}S}}$ which are described in the main text.

Regarding the B-bonded isomer only, we also observe the physisorbed junction formations where each S atom is saturated with hydrogen from the passivation layer. In this way, two unsaturated Si atoms per molecule are formed in the top surface Si layer which are adjacent to each other. To achieve a stable conformation, these undesirable valences, or dangling bonds, are removed by dimerisation (see bottom right panel of Fig. 4.1).

In the same pattern in which we express the junction dipole $\mu_{\mathrm{Au\text{-}Mol}}$ in Eq. 3.1, we

also describe the dipole moment of the silicon-molecule junction, $\mu_{\text{Si-Mol}}$, which reads:

$$\mu_{\text{Si-Mol}} = \mu_{\text{Mol}\{\text{jcn}\}} + \mu_{\text{Si}\{\text{jcn}\}} + \mu_{\text{Si-S}} \tag{4.1}$$

where $\mu_{\text{Si}\{\text{jcn}\}}$ is the dipole moment of the bare dihydride-terminated Si substrate in the junction basis-set and the geometry it adopts in the junction structure; $\mu_{\text{Si-S}}$ the dipole moment of the silicon-molecule interface. The interface dipole $\mu_{\text{Si-S}}$ is positive and, in the case of chemisorbed junctions, is therefore opposite to the polarity of the Si-S bond. The reason is the rearrangement of hydrogen atoms from the passivation layer towards the S atoms of the molecule, leading to the removal of free radicals from the originally unsaturated thiol linker groups and the subsequent formation of dangling bonds on the top surface Si layer.

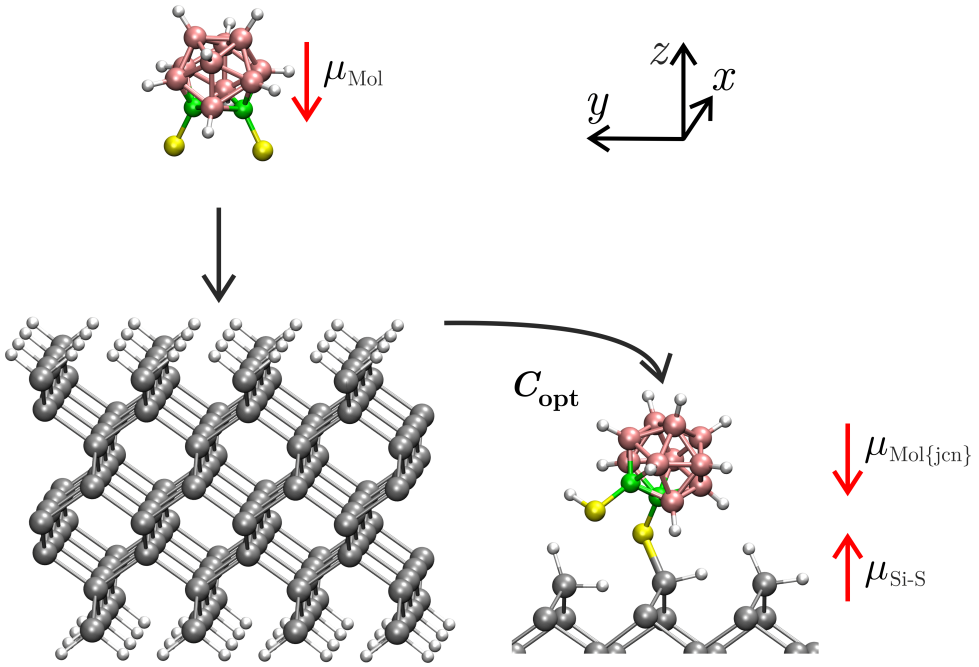

Figure 4.2: Adsorption of C-bonded carboranedithiol on Si(100). The geometric depiction of the adsorption of the unsaturated C-bonded *ortho*-carboranedithiol isomer (top left panel) on the straightened dihydride-terminated Si(100) wafer composed of 8 Si layers (bottom left panel) leading to the formation of the chemisorbed silicon-molecule junction (right panel). When reaching the most stable conformation, the final junction is referred to as C_{opt}. Red arrows indicate the dipole moment quantities which are described in the main text.

When only one hydrogen atom per molecule is rearranged, the bonding interaction occurs between the free radical located on the other unsaturated thiol group and the dangling bond on the top Si layer (see top right panel of Fig. 4.1 and right panel of Fig. 4.2). Thus, the monovalent chemisorption between the carboranedithiol molecule and the dihydride-terminated silicon proceeds by a radical mechanism [118]. With regard to the physisorption between the relevant subsystems, the interaction occurs when two hydrogen atoms per molecule are transferred. In this way, the molecule is fully hydrogen-saturated and the adjacent dangling bonds together form the Si-Si dimer (Fig. 4.1, bottom right panel).

Therefore, in order to monitor the interaction between the organodithiol molecule and the hydrogen-passivated silicon, we need one of the subsystems to carry the unpaired electron [118]. For this reason, we employ the carborane cage functionalised with the unsaturated thiol groups, or the sulphur radicals.

Unlike the gold-molecule interface, the charge transfer between the molecule and the silicon takes place in a somewhat more complex process, namely the surface transfer doping [13, 15, 22, 24–26]. Specifically, not only the surface dipole change, which gives rise to the surface potential-energy step, but also the band bending inside the subsurface space-charge layer of the semiconductor contribute to the change of the silicon work function. In this chapter, we observe the Si band bending, or the shift in the Si band structure, of a few tenths of an eV induced by the carboranedithiol adsorption. This is accompanied by the modification of electron and hole injection barriers between the substrate and the adsorbate.

4.2 Chapter overview

We divide the theoretical study of the silicon-molecule junctions into four stages, or four sections. In the first stage (Sec. 4.3), we calculate stable junction conformations of the B-bonded and the C-bonded carboranedithiol molecules on the dihydride-terminated Si(100) surface in a similar way as in Sec. 3.3, i.e. by a systematic investigation of possible adsorption geometries and their subsequent structural relaxation. Then, we select the most stable junction structures which we deal with in other stages of the theoretical study.

In the second stage (Sec. 4.4), we examine the electronic properties of the lowest-energy geometries in terms of the charge density and the electrostatic potential energy. As in Sec. 3.4, we also observe the changes in these quantities caused by the molecule adsorption, in particular the work function change of the dihydride-terminated silicon surface $\Delta\Phi_{\mathrm{Si}}$. In the third stage (Sec. 4.5), we deal with the mechanical properties of the most stable conformations upon their stretching to explore the stiffness and the stability of the Si–S bond.

Finally, in the last forth stage (Sec. 4.6), we analyse the silicon band structures of the selected conformations and observe shifts in Si features triggered by the formation of the silicon-molecule interface.

In the blue box below, we describe the computational details of all the stages of the theoretical study of the silicon-molecule junctions.

Computational details

For the structural relaxations and the subsequent calculations of electronic, mechanical, and band properties, we characterise silicon and other atoms via a local-orbital SZP and DZP basis set, respectively, with the largest (shell-dependent) values for the radial confinement radii (*Bohr*): 6.459 (boron), 5.205 (hydrogen), 5.519 (carbon), 5.487 (sulphur), 6.930 (silicon). We use the vdW-DF functional of Dion et al. [64] in the implementation of Román-Pérez and Soler [109] to describe exchange–correlation, including van der Waals interactions. We use a real-space cutoff of 250 *Ry*. Further computational details regarding the study of the silicon-molecule junctions are as follows:

First stage (Sec. 4.3)**:** We build the unit cell containing the *ortho*-carboranedithiol molecule positioned above the (4×4) slab of the dihydride-terminated Si(100) wafer with a thickness of 8 Si layers. Each Si layer and dihydride-passivation layer consists of 16 Si and 32 H atoms, respectively. We introduce a vacuum gap of ∼12 *Å* to remove interactions with the images in the surface-normal direction. To obtain stable junction geometries, we relax the coordinates of the molecule, the topmost dihydride layer, and the top three surface Si layers

until residual forces fall below 0.02 $eV \cdot \mathring{A}^{-1}$. We sample the Brillouin zone in the direction parallel to the surface with a 2×2 Monkhorst–Pack k-point grid.

Second stage (Sec. 4.4)**:** We assemble the unit cells of the isolated molecule and the bare dihydride-terminated Si(100) wafer from the unit cell of the relaxed silicon-molecule junction. As in Sec. 3.4, we preserve the atomic arrangement, the unit cell size, and the extent of the basis set. Using the slab dipole correction and the frozen-geometry conditions, for each of the assembled structures, we calculate the distributions of the electron and the ionic-charge density. We use a 6×6 k-point grid for the in-plane k-point sampling.

Then, we calculate the distributions of the electrostatic and the neutral-atom potential energies for the relaxed silicon-molecule junction and the relaxed bare dihydride-terminated Si(100) wafer. We describe the junction and the bare silicon in the unit cell size of the junction and the basis sets without ghost orbitals. Here, we again introduce the conditions of the single-point calculation, i.e. a 6×6 k-point grid and the slab dipole correction.

Third stage (Sec. 4.5)**:** We take the unit cell of the relaxed silicon-molecule junction and stretch its geometry by gradual pulling of the molecule from the surface. For each displacement of the molecule, we correspondingly enlarge the unit cell in the surface-normal direction to maintain the vacuum gap of ∼12 $\mathring{A}$ between the images. With the frozen z-coordinate of the topmost atom of the carborane cage, we stabilise each of the stretched junctions by means of the same geometry-relaxation strategy as in the first stage. Then, for each stable junction, we compute the total energy by means of the single-point calculation (see above).

Forth stage (Sec. 4.6)**:** For the stable bare dihydride-terminated Si(100) wafer and the stable silicon-molecule junction, both in the unit cell size of the junction, we calculate band structure under the conditions of the single-point calculation. We choose the **k**-point path: $\Gamma \rightarrow \mathrm{J_{y4}} \rightarrow \mathrm{K_{44}} \rightarrow \mathrm{J_{x4}} \rightarrow \Gamma$.

4.3 Adsorption of carboranedithiol on Si(100)

In this section, we search for and investigate stable adsorption geometries of each of the two carboranedithiol isomers on the silicon substrate. To generate initial junction conformations, we employ the straightened phase of the dihydride-terminated Si(100) wafer (see bottom left panels of Fig. 4.1 and 4.2) because it provides more adsorption sites for the molecule than the surface composed of canted dihydrides.

We separate this section into four parts. In the first two, we pay attention to the initial orientations of the molecule above the surface before the geometry relaxation. Then, we characterise a plenty of relaxed structures and select the most stable ones. In the last part, for the most favourable conformations, we study in detail the mechanism of their formations.

4.3.1 Lateral orientation

We build many initial geometries of the molecule above the silicon substrate. First, we place the centre of the vertically oriented carborane cage above the silicon at two horizontal positions (Fig. 4.3(b)), i.e. the sites that we design to be out of the high-symmetry points of the surface. Specifically, we shift the first horizontal position (red diamond) by $\Delta x_1 = -0.7$ Å and $\Delta y_1 = \Delta x_1$, and the second position (violet diamond) by $\Delta x_2 = (-(1/(2\sqrt{2}))\, a_{\mathrm{Si}} + 0.7$ Å) and $\Delta y_2 = \Delta x_2$, respectively, with respect to the point exactly between two adjacent SiH_2 units (black diamond).

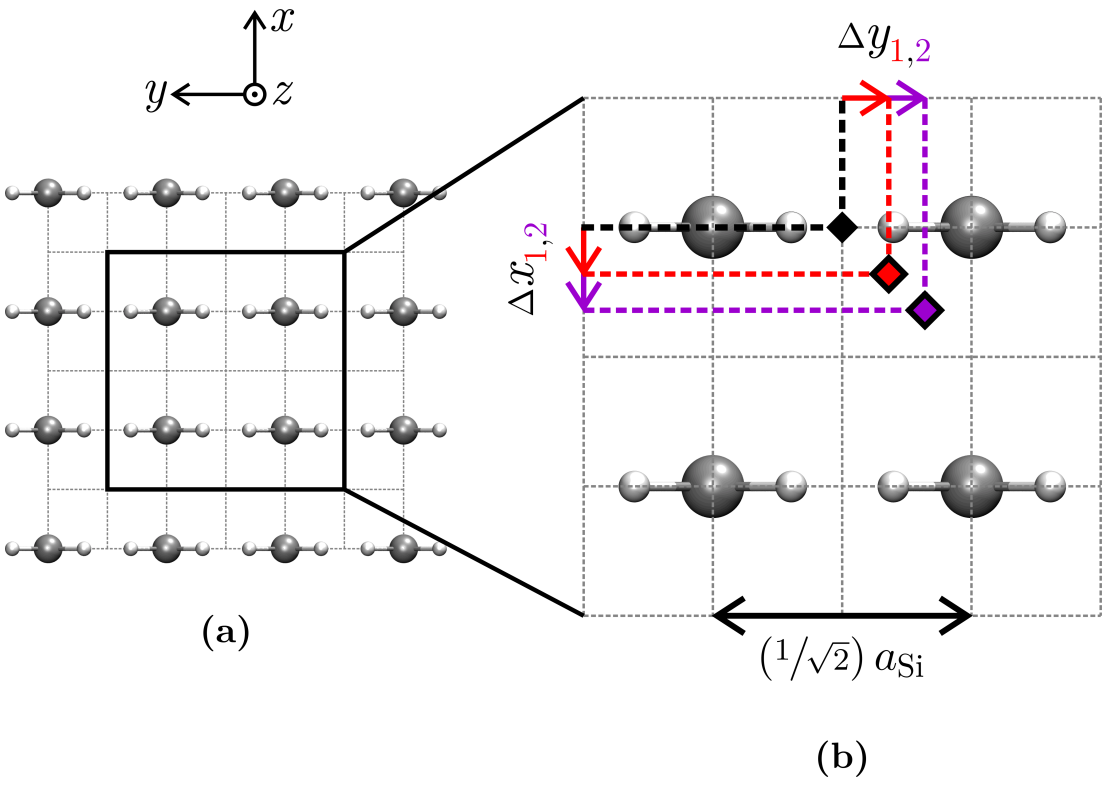

Figure 4.3: Initial lateral positions for molecule above Si(100). The top view of the top surface Si layer of the straightened dihydride-terminated Si(100) wafer in the form of **(a)** the (4×4) slab and **(b)** its zoomed inner part with the marked positions for the initial lateral placement of the molecule. The black diamond represent the high-symmetry point. The red and the violet diamonds refer to the first and the second lateral positions, respectively, for the initial placement of the carboranedithiol molecule.

4.3.2 Spherical orientation

We define the azimuthal angle φ_{Mol} as the angle between the line connecting both S atoms and the row of surface Si atoms (Fig. 4.4(a)). In each of the two lateral positions, we probe the angle φ_{Mol} from 0 to 90° in steps of 10°. In this way, for each of the two isomers, we get 20 initial geometries with the vertically oriented carborane cage. In addition to these structures, we produce the same series with the molecule tilted by $\theta_{\text{Mol}} = 30°$ around the line connecting both S atoms (Fig. 4.4(b)). Thus, we generate 40 initial conformations (2 lateral × 10 azimuthal × 2 polar orientations) for the B-bonded and the C-bonded carboranedithiol adsorbate (a total of 80 conformations) which we subject to the geometry optimisation step.

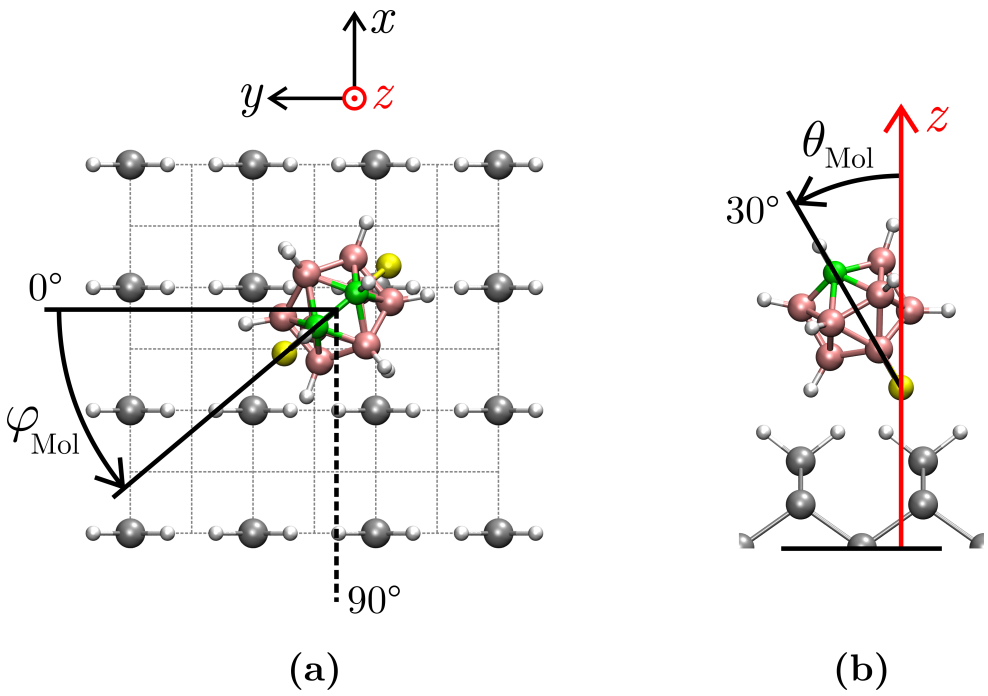

Figure 4.4: Initial geometries of silicon-molecule junctions. Generation of initial geometries of the carboranedithiol molecule above the (4×4) slab of the straightened dihydride-terminated Si(100) wafer. **(a)** The top view of the junction with probing of the azimuthal angle φ_{Mol} between 0 and 90°. **(b)** The side view of the junction with the tilt angle $\theta_{\text{Mol}} = 30°$. The quantities are described in the main text. Red arrow indicates the surface-normal direction (z-axis).

4.3.3 Relaxed junctions

In Fig. 4.5, we summarise the calculated total energies and structural characteristics of the 80 relaxed geometries of the silicon-carboranedithiol junctions, one half of which contains the B-bonded adsorbate (left panel) and the other half the C-bonded adsorbate (right panel). On the vertical axis, for each panel, we express the total energy of the optimised geometry ($E_{\text{Si-Mol}}$) with respect to the corresponding global energy minimum, i.e. the energy of the most stable structure for a given set of data points. For the set of B-bonded and the set of C-bonded geometries, we highlight these structures by a black circle in group A and C, respectively, and denote as A_{opt} and C_{opt}, respectively. On the horizontal axis, we depict the shortest Si-S distance in the structure. Since the carboranedithiol molecule is not hydrogen-saturated, whether it forms bond(s) to the substrate or not strongly influence the energy of the silicon-molecule interface.

We colour-code the data points in Fig. 4.5 according to the number of Si-S bonds

between the molecule and the silicon surface in the relaxed geometry: no bonds and the physisorbed molecule (light blue (B-bonded), blue (C-bonded)), one bond (orange (B-bonded), blue-green (C-bonded)), and two bonds (green (B-bonded), red (C-bonded)). In the left panel, we can clearly separate the data points into four groups: group A contains structures with one Si-S bond per molecule whose relative energies are up to 0.6 eV above the energy of A_{opt}; group B consists of geometries within in the same energy range with no Si-S bonds; group D involves geometries having Si-S bond(s) which are more than 1.2 eV less favourable than A_{opt}; group E describes structures lacking Si-S bonds whose energies are at least 1.2 eV higher than the total energy of A_{opt}. As for the data points in the right panel, we divide them into only three groups: group C consists of geometries having Si-S bond(s) whose energies are at most 0.6 eV less favourable than C_{opt}; groups F and G contains structures with one or no Si-S bond, respectively, whose energies are at least 1.2 eV above the total energy of C_{opt}.

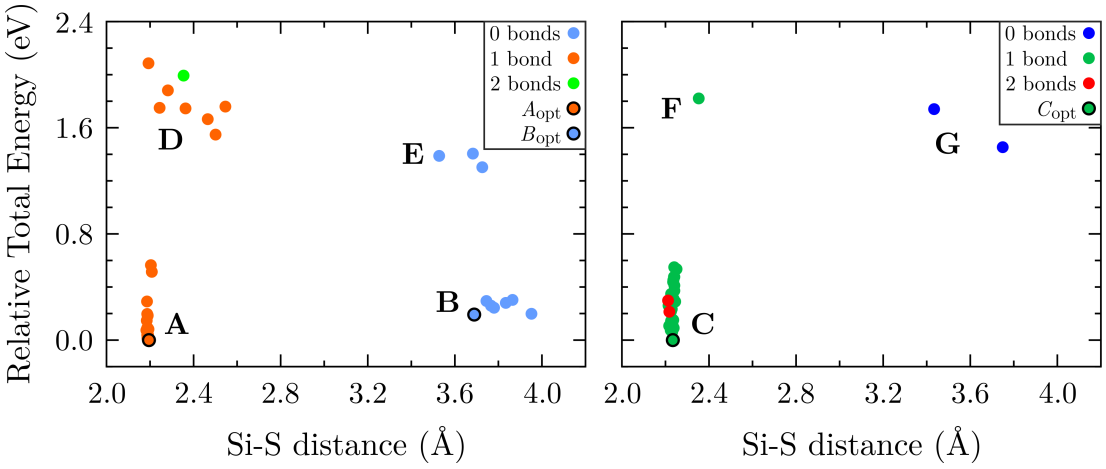

Figure 4.5: Relaxed characteristics of silicon-molecule junctions. Relative total energy of the relaxed geometries as a function of the final sulphur-silicon distance for a series of conformations of the B-bonded (left panel) and the C-bonded junctions (right panel). Group **A**: $E_{\text{Si-Mol}} - E_{\text{Si-Mol}}(A_{\text{opt}}) < 0.6\ eV$ and at least one Si-S bond; group **B**: $E_{\text{Si-Mol}} - E_{\text{Si-Mol}}(A_{\text{opt}}) < 0.6\ eV$ and no Si-S bonds; group **C**: $E_{\text{Si-Mol}} - E_{\text{Si-Mol}}(C_{\text{opt}}) < 0.6\ eV$ and at least one Si-S bond; group **D**: $E_{\text{Si-Mol}} - E_{\text{Si-Mol}}(A_{\text{opt}}) > 1.2\ eV$ and at least one Si-S bond; group **E**: $E_{\text{Si-Mol}} - E_{\text{Si-Mol}}(A_{\text{opt}}) > 1.2\ eV$ and no Si-S bonds; group **F**: $E_{\text{Si-Mol}} - E_{\text{Si-Mol}}(C_{\text{opt}}) > 1.2\ eV$ and at least one Si-S bond; group **G**: $E_{\text{Si-Mol}} - E_{\text{Si-Mol}}(C_{\text{opt}}) > 1.2\ eV$ and no Si-S bonds. The legend in each panel shows the number of the Si-S bonds in the junction and the lowest-energy conformations A_{opt}, B_{opt}, and C_{opt}, which are highlighted by a black circle in group **A**, **B**, and **C**, respectively.

Low-energy conformations. Groups A and C in Fig. 4.5 include the chemisorbed products of the carboranedithiol adsorption, the typical geometries of which are shown in top right panel of Fig. 4.1 and right panel of Fig. 4.2, respectively. These are the junctions with one Si-S bond while the other S atom is hydrogen-saturated. Their formation takes place in two steps: first, one S atom pulls one H atom out of the top passivation layer, resulting in one saturated thiol group and one dangling bond on the top Si layer; then, the free radical on the other unsaturated S atom recombines with the dangling bond on the surface to create the Si-S bond.

Of the 40 initial B-bonded and the 40 initial C-bonded geometries, 22 converge to category A and 37 to category C. The hybridisation state of the Si atom participating in the Si-S bond is unchanged, still having four tetrahedral bonds (two to Si neighbours, one to H, and one new bond to S). The lowest-energy data point of the left panel of Fig. 4.5, i.e. A_{opt} circled at the bottom of group A, belongs to the junction conformation

with the carborane cage tilted by $\theta_{\text{Mol}} \sim 43°$ and the Si-S bond length of $d_{\text{Si-S}} = 2.20$ $\mathring{A}$. Regarding the right panel, the data point with the lowest total energy, i.e. C_{opt} circled at the bottom of group C, characterises the junction with the molecule tilted by $\theta_{\text{Mol}} \sim 39°$ and the Si-S bond of $d_{\text{Si-S}} = 2.23$ $\mathring{A}$. We depict the atomic structures of A_{opt} and C_{opt} in top right panel of Fig. 4.1 and right panel of Fig. 4.2, respectively.

Of the 37 geometries in group C, we observe 2 junctions with two Si-S bonds per molecule (Fig. 4.6(C_2)). In the formation of such geometries, both S atoms covalently bond to the same surface Si atom, leading to the rupture of the adjacent Si-Si bond and the subsequent transfer of one H atom to the neighbouring Si atom. The tetragonal hybridisation of all surface Si atoms is preserved, making the junctions the members of the low-energy group C.

The remaining 7 low-energy data points belong to group B where the respective total energies are comparable to those in group A. Specifically, group B is composed of the physisorbed junctions with no Si-S bonds and one Si-Si dimer per molecule. In bottom right panel of Fig. 4.1, we show the atomic structure of these types of junctions, namely the structure of the most stable conformation of group B. We denote it as B_{opt} and highlight by a black circle at the bottom of the group. The total energy of B_{opt} is 0.19 eV higher than the energy of A_{opt}. The mechanism of formation of physisorbed junctions proceeds in two steps: first, each of the two S atoms pulls one H atom out of the top passivation layer, creating the fully hydrogen-saturated carboranedithiol molecule and two dangling bonds on two adjacent surface Si atoms; then, the neighbouring dangling bonds recombine with each other to form the Si-Si dimer. The fully saturated molecule is physisorbed above the reconstructed surface, with the shortest Si-S distance being in the range from $d_{\text{Si-S}} \sim 3.6$ to 4.0 $\mathring{A}$.

High-energy conformations. Groups D, E, F and G in Fig. 4.5 represent unfavourable junction geometries, i.e. local minima whose total energies exceed the energies of the corresponding global minima by more than 1.2 eV. During the formation of high-energy conformations, some atoms in the region of the silicon-molecule interface end up in sub-optimal valence states, namely a dangling bond remaining on the surface Si atom or an unpaired electron on the S atom.

Group D and F include high-energy chemisorbed junctions in which the carboranedithiol adsorbate is covalently bonded to the substrate via one Si-S bond, only in one case via two Si-S bonds. The eight initial B-bonded geometries converge to category D while the only one initial C-bonded arrangement to category F. Concerning group D, seven data points belong to conformations with one Si-S bond per molecule, the last eighth point to the junction with two Si-S bonds. Examples of these structures are shown in Fig. 4.6(D_1) and (D_2), respectively, where we employ coloured rings to highlight atoms in the sub-optimal valence states. In particular, we point out to these atoms that do not meet the octet rule, i.e. they do not have 8 electrons in their valence sphere and therefore carry an unpaired electron, making the silicon-molecule junction less stable. These unfavourableWe color-cpode the data points of Fig. 4.5 according to the numner of S-Si bonds states always concern the S atoms and the surface Si atoms directly involved in the adsorption mechanism. In Fig. 4.6(F_1), we depict the atomic structure of the C-bonded junction which itself forms category F.

The last groups E and G in Fig. 4.5 composed of three and two data points, respectively, introduce high-energy physisorbed junctions with the B-bonded and the C-bonded carboranedithiol isomers, respectively. The fully hydrogen-saturated molecule is located above the surface of the Si substrate with the shortest Si-S distance from $d_{\text{Si-S}} \sim 3.4$ to 3.8 $\mathring{A}$. One of the conformations concerning groups E and G are shown in Fig. 4.6(E_0) and (G_0), respectively. On each of these geometric representations, we

use a cyan-coloured ring to highlight the surface Si atom that lacks two H atoms. This atom has two dangling bonds that cannot recombine with each other by any surface reconstruction, leading to an increase in the total energy of the junction.

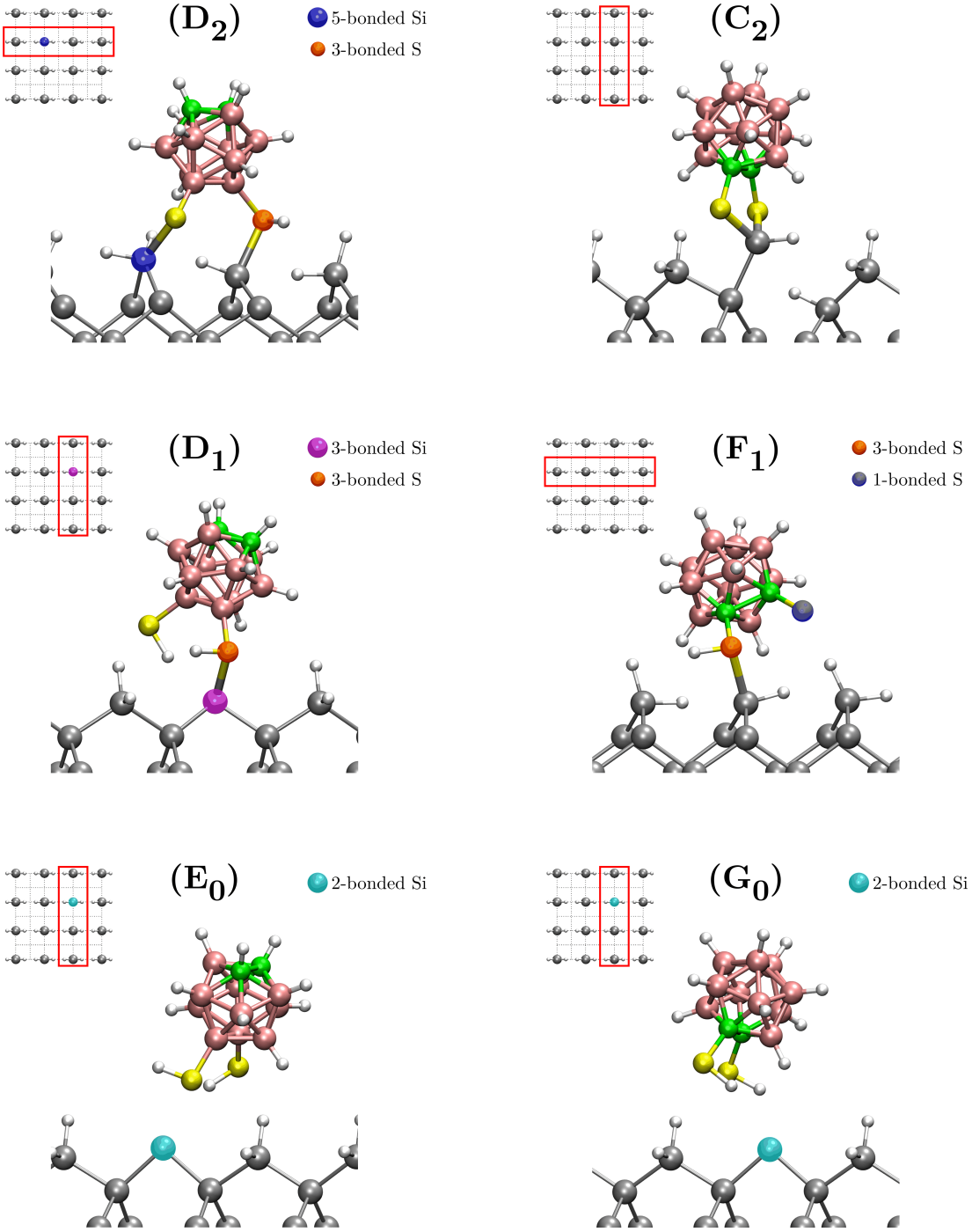

Figure 4.6: Artefactual relaxed silicon-molecule junctions. The side views of the artefactual geometries of the relaxed silicon-carboranedithiol junctions named according to the group in Fig. 4.5; the subscript coincides with the number of Si-S bonds in the junction. For each geometry, the inset depicts the position of the corresponding cut out structure in the (4×4) unit cell. The legends show prominent elements with sub-optimal valence states that lead to higher total energies.

Summary. While all 80 structures contained in Fig. 4.5 are local minima, we expect those in groups A, B and C are representative examples of the experimental situation.

We anticipate that the geometries in groups D, E, F and G would be unstable under perturbation and would relax to more stable conformations, releasing the excess energy from the system.

According to our description of chemisorption and physisorption accompanied by surface dimerisation, it is clear that the interaction between the molecule and the substrate occurs when one of these subsystems has a reactive site with an unpaired electron. Therefore, we functionalise the carborane cage with unsaturated thiol groups, or sulphur radicals, to achieve a variety of silicon-molecule junctions. When investigating the interaction between the fully hydrogen-saturated carboranedithiol molecule and the dihydride-terminated silicon surface, we do not observe any signs of covalent adsorption or surface reconstruction. There is only ordinary physisorption without any structural modifications of the subsystems. The corresponding shortest Si-S distance is $d_{\text{Si-S}} \sim 3.6$ *Å*, which is similar to those in groups B, E and G.

Across all simulations in this section, we get the physical-chemical insight, which we summarise in the following findings:

- S binds to Si more readily than H. As a consequence, S always replaces H in the passivation layer on the Si surface.
- H readily binds to S, thus saturating the molecular thiol linker group which does not participate in the Si-S bond.
- Saturated carboranedithiol does not chemisorb on the hydrogen-passivated Si substrate. Only unsaturated thiol groups carrying unpaired electrons form Si-S bonds to the substrate.
- The formation of covalent Si-S bonds does not induce the reconstruction of the Si surface. This is because S substitutes H, allowing the bonding Si atom to retain its hybridisation state and bond angles.
- The presence of the molecule is a certain type of perturbation for the straightened dihydride-terminated Si(100) surface. As a result, during the simulation, the Si substrate leaves this metastable state and transforms into the canted-dihydride phase with lower total energy.

4.3.4 Energy path of adsorption

In this part and the following Sec. 4.4, 4.5, and 4.6, we deal only with A_{opt}, B_{opt}, and C_{opt} conformations. After all our calculations in the previous part 4.3.3, the bottom side of each relaxed unit cell remains in the straightened-dihydride phase. For this reason, for all three conformations, we purposefully rearrange the bottommost hydrogen atoms and the bottom three surface Si layers of the unit cell to the canted-dihydride phase, making the dihydride-terminated Si substrate the centro-symmetric slab.

In this part, we are interested in the energy path of adsorption of the unsaturated carboranedithiol molecule on the dihydride-terminated Si surface to form A_{opt}, B_{opt}, or C_{opt} junctions. In particular, we calculate the binding energy, E_{B}, of the selected conformations (see Tab. 4.1) as the total energy of the resulting junction, $E_{\text{Si-Mol}}$, with respect to the total energy of the reference system, i.e. the system consisting of the isolated unsaturated carboranedithiol molecule, E_{Mol}, and the bare dihydride-terminated Si slab, E_{Si}:

$$E_{\text{B}} = E_{\text{Si-Mol}} - (E_{\text{Si}} + E_{\text{Mol}}) \tag{4.2}$$

The binding energy, or the adsorption energy, of any silicon-molecule junction is the sum of individual energy contributions associated with the formation and the breakdown of certain chemical bonds that are directly involved in the molecule adsorption. During the chemisorption of one carboranedithiol molecule, one Si–H bond is broken and one S–H bond and one Si-S bond are formed at the silicon-molecule interface. Therefore, the binding energy of the A_{opt} and the C_{opt} conformations reads:

$$E_{\mathrm{B}}(A_{\mathrm{opt}}, C_{\mathrm{opt}}) = E_{\text{Si-H}} + E_{\text{S-H}} + E_{\text{Si-S}} \tag{4.3}$$

where $E_{\text{Si-H}}$ is the energy cost of breaking the Si–H bond, $E_{\text{S-H}}$ and $E_{\text{Si-S}}$ are the energies released due to the S-H bond and the Si-S bond formation, respectively. The sequence of these quantities in Eq. 4.3 corresponds chronologically to the adsorption pathway, making the chemisorption the three-step radical reaction. Therefore, the reaction steps read:

$$E_{\text{Si-H}} = (\ E_{\text{Si,rad}} \ + \ E_{\text{H,rad}}\ ) - E_{\text{Si}} \quad , \tag{4.4}$$

$$E_{\text{S-H}} = \ E_{\text{Mol+H}} - (\ E_{\text{Mol}} \ + E_{\text{H,rad}}\ ) , \tag{4.5}$$

$$E_{\text{Si-S}} = \ E_{\text{Si-Mol}} - (\ E_{\text{Mol+H}} \ + E_{\text{Si,rad}}\ ) . \tag{4.6}$$

Here, in the first line, $E_{\text{Si,rad}}$ and $E_{\text{H,rad}}$ are the total energies of the silicon surface with one dangling bond and the hydrogen radical, respectively, i.e. the products of the endergonic breaking of the Si-H bond. This step is triggered by the influence of a free radical on the anchoring S atom of the molecule because $E_{\text{Si-H}} < -E_{\text{S-H}}$. In the second line, $E_{\text{Mol+H}}$ is the total energy of the molecule with one H-saturated thiol group, the second S linker atom carries a free radical. The S-H bond of this molecule results from elimination of the free radical on the first S linker atom by the hydrogen radical. The last line describes the removal of the dangling bond on the top Si layer by the radical of the second S linker atom, giving rise to the Si-S bond. We calculate all the energy quantities on the right-hand sides of Eq. 4.4, 4.5, and 4.6 in the unit cell of the A_{opt} or the C_{opt} junctions.

In Tab. 4.1, we list the calculated values of all quantities contained in Eq. 4.3. In particular, we see the A_{opt} structure has the higher (more negative) binding energy than the C_{opt} structure, namely -4.305 eV compared to -3.829 eV, respectively. This is because the covalent adsorption of the B-bonded isomer releases more energy caused by the Si-S bonding of the carborane cage and the hydrogen saturation of the other S atom than the equivalent adsorption of the C-bonded one. Regarding the Si-S bond formation only, we obtain the respective energy values of $E_{\text{Si-S}} = -3.895$ and -3.714 eV for the A_{opt} and the C_{opt} junctions, respectively, which are very similar to the DFT-based value of -3.82 eV reported by Peiris et al. [118] for alkanethiols on Si(111). In terms of experimental approaches, Huang et al. [119] deposited the SAM of 1-octadecanethiols on the oxide-free surface of the n-type Si(111) wafer with the Si-S bond energy of 3.04 eV, i.e. with apparently lower energy than in our calculations. The same value is reported in Huheey et al. [120]. As for the other Si-H and S-H bonds, they are 3.30 and 3.76 eV, respectively [120]. For comparison, we also present the reported energies of some covalent bonds having one identical atomic species with the S-Si, namely 2.30 eV for the Si-Si, 3.30 eV for the Si-C, and 2.34 eV for the S-S [120][①].

During the physisorption of one B-bonded isomer, two Si-H bonds are broken, two S-H bonds are formed, and below the fully saturated molecule, the Si surface reconstruction associated with the formation of one Si-Si dimer occurs. Thus, the corresponding binding energy of the B_{opt} conformation is the sum:

[①] Energies in [120] are reported in more experimentally accessible enthalpies of dissociation.

$$E_{\mathrm{B}}(B_{\mathrm{opt}}) = E_{\text{Si-H}} + E_{\text{S-H}} + E_{\mathrm{rec}} \tag{4.7}$$

where E_{rec} is the energy released due to the Si surface reconstruction. As in the case of the chemisorption, we can divide the physisorption into three radical reaction steps:

$$E_{\text{Si-H}} = (\ E_{\mathrm{Si,2rad}} \ + \ 2E_{\mathrm{H,rad}}\ ) - E_{\mathrm{Si}} \quad , \tag{4.8}$$

$$E_{\text{S-H}} \ = \ E_{\mathrm{Mol+2H}} - (\ E_{\mathrm{Mol}} \ + 2E_{\mathrm{H,rad}}\ ) , \tag{4.9}$$

$$E_{\mathrm{rec}} \ = \ E_{\text{Si-Mol}} \ - (\ E_{\mathrm{Mol+2H}} \ + E_{\mathrm{Si,2rad}}\ ) . \tag{4.10}$$

Here, in the first line, $E_{\mathrm{Si,2rad}}$ is the total energy of the silicon surface with two dangling bonds, each on one of the adjacent top Si atoms. This is the product of the radical-induced breaking of two Si-H bonds on the corresponding two neighbouring Si atoms, with the driving force being again the energy balance: $E_{\text{Si-H}} < -E_{\text{S-H}}$. The second line describes the full saturation of both thiol groups of the molecule with two hydrogen radicals, giving the product with the energy of $E_{\mathrm{Mol+2H}}$. The last line describes the release of energy caused by the mutual elimination of both dangling bonds, the Si-Si dimer formation, and the stabilisation of the final configuration with the molecule.

We summarise the final values of all energy quantities from Eq. 4.7 in Tab. 4.1. The energies $E_{\text{Si-H}}$ and $E_{\text{S-H}}$ related to the B_{opt} structure are approximately double the equivalent energies of the chemisorbed junctions, which is clear from the different mechanisms of the chemisorption and the physisorption processes. The binding energy of the B_{opt} junction is $-4.114\ eV$.

Table 4.1: Energy quantities associated with junction formation. Calculated values of the energy quantities related to the formation of A_{opt}, B_{opt}, and C_{opt} junctions: the binding energy of the junction, E_{B}, the energy absorbed in breaking the Si-H bond(s), $E_{\text{Si-H}}$, the energy released in forming the S-H bond(s), $E_{\text{S-H}}$, and the Si-S bond, $E_{\text{Si-S}}$, and the energy released during the Si surface reconstruction, E_{rec}.

	$E_{\mathrm{B}}\ (eV)$	$E_{\text{Si-H}}\ (eV)$	$E_{\text{S-H}}\ (eV)$	$E_{\text{Si-S}}\ (eV)$	$E_{\mathrm{rec}}\ (eV)$
A_{opt}	-4.305	$+3.625$	-4.034	-3.895	/
C_{opt}	-3.829	$+3.629$	-3.743	-3.714	/
B_{opt}	-4.114	$+7.664$	-7.933	/	-3.845

4.4 Electronic properties

In this section, we go through the electronic properties of A_{opt}, B_{opt}, and C_{opt} conformations. In particular, as in Sec. 3.4, we examine the effect of the carboranedithiol adsorption on the charge density distribution across the silicon-molecule interface (part 4.4.1) and on the electrostatic potential energy above the dihydride-terminated Si surface (part 4.4.2).

4.4.1 Charge density

To describe the charge density rearrangement upon the silicon-molecule interface formation, we compute the corresponding plane-averaged charge density difference:

$$\rho_{\mathrm{diff}}(z) = \rho_{\text{Si-Mol}}(z) - \left[\rho_{\mathrm{Mol\{jcn\}}}(z) + \rho_{\mathrm{Si\{jcn\}}}(z)\right] . \tag{4.11}$$

where, $\rho_{\text{Si-Mol}}(z)$, $\rho_{\text{Mol}\{\text{jcn}\}}(z)$, and $\rho_{\text{Si}\{\text{jcn}\}}(z)$, are the plane-averaged charge densities of the silicon-molecule junction, the isolated molecule, and the bare Si surface, respectively, in the basis set and the atomic arrangement of the junction.

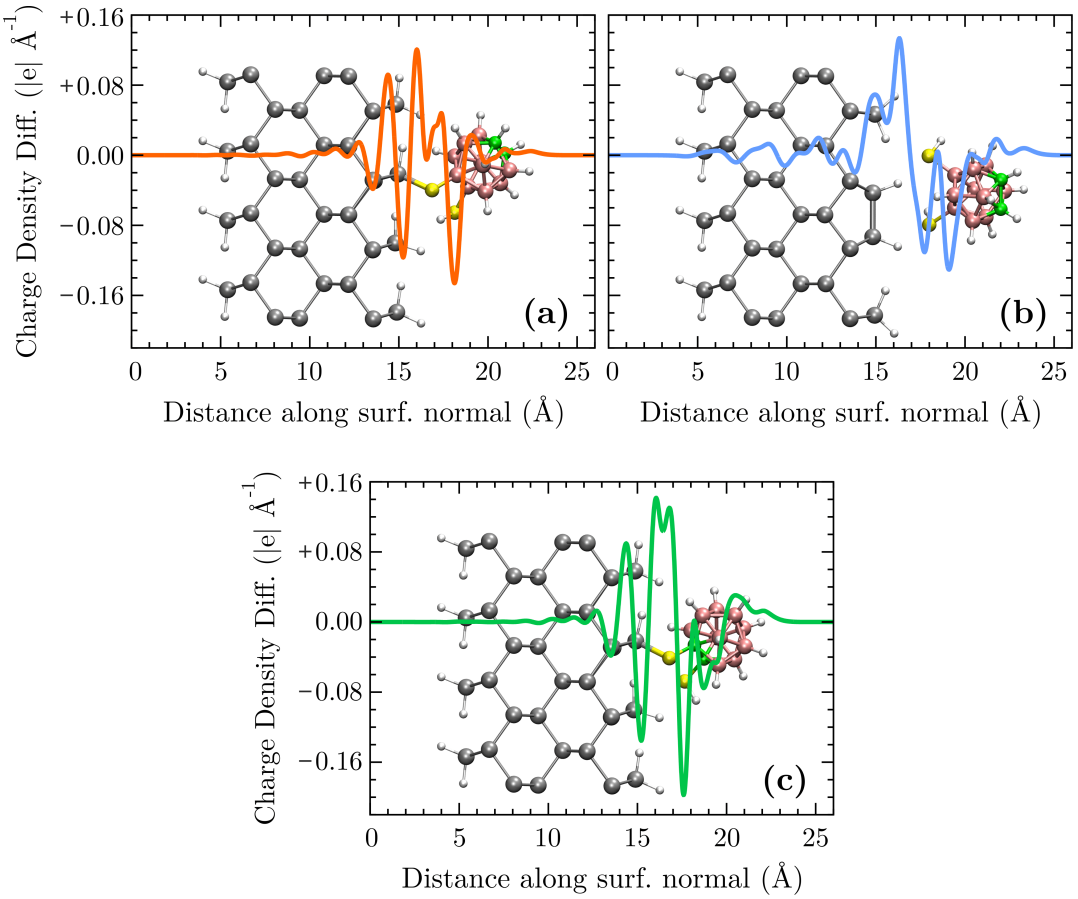

Figure 4.7: Charge density difference of silicon-molecule junctions. Plane-averaged charge density difference profiles across **(a)** the A_{opt}, **(b)** the B_{opt}, and **(c)** the C_{opt} conformations. Orange, blue and green curves belong to the respective conformations, respectively. In each panel, the inset behind the curve introduces the side view of the final relaxed junction.

In Fig. 4.7, we depict the calculated $\rho_{\text{diff}}(z)$ profiles for the A_{opt} (panel (a), orange curve), the B_{opt} (panel (b), blue curve), and the B_{opt} conformations (panel (c), green curve). As in Sec. 3.4.1, the $\rho_{\text{diff}}(z)$ curve meets the fundamental properties, namely it integrates to zero and its positive or negative values characterise electron accumulation or depletion, respectively, upon the adsorption. However, compared to the gold-molecule junctions, the charge rearrangement in the silicon-molecule interface is more complicated, making the interpretation of the respective curves more difficult.

In Fig. 4.7, the $\rho_{\text{diff}}(z)$ profiles show a noticeable bunch of oscillations from the zero value in the range from the second topmost Si layer to the half of the carborane backbone, i.e. at the surface-normal distance from ∼13 to ∼19 *Å* for the chemisorbed geometries and from ∼13 to ∼20 *Å* for the B_{opt}. Upon the A_{opt} (Fig. 4.7(a)) and the C_{opt} formations (Fig. 4.7(c)), electrons are particularly accumulated at ∼14, ∼16, and ∼17 *Å* due to the increases in the Mulliken populations of the right (top) surface Si layer, the right (top) out-of-plane hydrogen passivation layer, and the chemisorbing S atom, respectively. The electron depletions are apparent mainly at ∼15 and ∼18 *Å* because of the decreases in the orbital populations of the right (top) in-plane hydrogen passivation layer and the hydrogen-saturated S atom, respectively. Regarding the

sulphur-saturating hydrogen at ∼17 Å in the A_{opt} and at ∼18.5 Å in the C_{opt}, it reveals the decrease in the Mulliken population, making the oscillation at ∼17 Å more positive in the case of the green curve compared to the orange one. In Tab. 4.2, we list the specific values of the orbital-population changes that, with some exceptions[②], predict well the sign and the magnitude of the mentioned deviations in the respective $\rho_{\text{diff}}(z)$ profiles of the chemisorbed geometries.

Table 4.2: Mulliken population changes associated with junction formation. Calculated changes in the Mulliken populations upon the formation of A_{opt} and C_{opt} junctions. Specifically, there are population changes of the top surface Si layer, Si_{surf} ($|e|$), the chemisorbing Si atom, Si_{ch} ($|e|$), the top in-plane hydrogen layer, H_{in} ($|e|$), the top out-of-plane hydrogen layer, H_{out} ($|e|$), the sulphur-saturating H atom, H_{S} ($|e|$), the chemisorbing S atom, S_{ch} ($|e|$), the hydrogen-saturated S atom, S_{H} ($|e|$).

	Si_{surf}	Si_{ch}	H_{in}	H_{out}	H_{S}	S_{ch}	S_{H}
A_{opt}	+0.19	+0.14	−0.03	+0.07	−0.07	+0.03	−0.03
C_{opt}	+0.16	+0.12	−0.05	+0.02	−0.08	+0.04	−0.12

Table 4.3: Dipole moment quantities related to silicon-molecule interface. Calculated values of the dipole moment quantities related to the silicon-molecule interface in the A_{opt}, the B_{opt}, and the C_{opt} conformations: the dipole moment of the silicon-molecule junction, $\mu_{\text{Si-Mol}}$, the dipole moments of the molecular adsorbate, $\mu_{\text{Mol\{jcn\}}}$, and the dihydride-terminated Si substrate in the basis set of the junction, $\mu_{\text{Si\{jcn\}}}$, and the dipole moment of the silicon-molecule interface, $\mu_{\text{Si-S}}$. The presented quantities read: $\mu_{\text{Si-Mol}} = \mu_{\text{Mol\{jcn\}}} + \mu_{\text{Si\{jcn\}}} + \mu_{\text{Si-S}}$ (see Eq. 4.1).

junction	$\mu_{\text{Si-Mol}}$ (D)	$\mu_{\text{Mol\{jcn\}}}$ (D)	$\mu_{\text{Si\{jcn\}}}$ (D)	$\mu_{\text{Si-S}}$ (D)
A_{opt}	+3.928	+4.881	−1.665	+0.712
B_{opt}	+5.354	+5.722	−2.939	+2.572
C_{opt}	−3.002	−1.290	−2.239	+0.527

As in Sec. 3.4.1, we numerically calculate the interfacial dipole $\mu_{\text{Si-S}}$ according to the relation:

$$\mu_{\text{Si-S}} = -\int_{0}^{z_{\text{unit}}} \rho_{\text{diff}}(z) z \, \mathrm{d}z \,, \tag{4.12}$$

by means of which we get the resulting values summarised in Tab. 4.3. In the pattern of this equation, we compute the corresponding dipole moments from the other charge density profiles contained in Eq. 4.11 and list them also in Tab. 4.3. All the presented dipole values meet Eq. 4.1.

The largest interfacial dipole $\mu_{\text{Si-S}}$ accompanies the formation of the B_{opt} junction, as can be seen from the simple visual comparison of all three curves in Fig. 4.7. Specifically, in Fig. 4.7(b), the blue curve has large positive and large negative deviations oriented more towards the surface and more towards the molecule, respectively, while in Fig. 4.7(a) and (c), the orange and the green curves, respectively, undergo more frequent changes in the sign of deflections along the surface-normal direction, making

[②] There is a mismatch between the larger increase in the Mulliken populations of the out-of-plane H layer of the A_{opt} and the higher positive oscillation in $\rho_{\text{diff}}(z)$ of the C_{opt} at ∼16 Å. The reason is probably the visible overlap of this oscillation peak with the neighbouring one at ∼17 Å in Fig. 4.7(c).

the resulting interfacial dipole smaller in the magnitude. The largest $\mu_{\text{Si-S}}$ for the B_{opt} junction is apparently caused by twice the number of transferred H atoms from the surface compared to the chemisorbed structures. In addition, in the chemisorbed geometries, the more electronegative S atom gives rise to the negative dipole of the emerging Si-S bond, reducing the final $\mu_{\text{Si-S}}$.

4.4.2 Electrostatic potential energy

To observe the molecular-dipole influence on the electrostatic changes above the surface, we employ the same strategy as in part 3.4.3. Specifically, in Fig. 4.8(a), (c) and (e), we plot the plane-averaged profiles of the electrostatic potential energy across the bare dihydride-terminated Si(100) wafer (dark-blue curve) and across the A_{opt} (panel (a), orange curve), the B_{opt} (panel (c), blue curve), and the B_{opt} junctions (panel (e), green curve), as the functions of the surface-normal distance. Obviously, the dark-blue curve is the same in all these panels. On the right-hand side of Fig. 4.8, we plot the plane-averaged distorted potential energies[③], to highlight the differences between the dark-blue curve and the orange, the blue, or the green curves in the vacuum (see panel (b), (d), or (f), respectively).

Each panel in Fig. 4.8 has five distinguishable regions along the surface-normal direction. For distances smaller than ∼3 *Å*, there is the left (bottom) vacuum region surrounding the Si surface which is unperturbed by the molecular adsorption. From the wafer surface towards this vacuum layer, all potential profiles rapidly converge to the reference asymptote at zero value. Towards the right in each plot, the potential-energy profiles pass through the left (bottom) dihydride layer (second region) between ∼3 and ∼6 *Å* and enter the inside of the Si wafer (third region) where all the curves show regular oscillations, characterising the bulk-like nature of the inner Si layers. Up to ∼13 *Å*, all the electrostatic-potential profiles or all the distorted-potential profiles coincide. In the fourth region, i.e. the interfacial region from ∼13 to ∼18 *Å* for the bare dihydride-terminated Si wafer and from ∼13 to ∼23.5 *Å* for the chemisorbed (A_{opt}, C_{opt}) or to ∼24.5 *Å* for the physisorbed junctions (B_{opt}), the profiles gradually diverge from each other due to the silicon-molecule interface formation and the relaxation of the right (top) dihydride layer and the right (top) three surface Si layers. Crossing the interface, all the potential profiles end in the right (top) vacuum region where they level out to their final asymptotic plateaus.

As in part 3.4.3, also here, we define the Si-surface potential-energy step, $\Delta U_{\text{Si,surf}}$, across the carboranedithiol layer, i.e. the distance between the outer right plateaus of the curve of the junction and the curve of the bare silicon:

$$\Delta U_{\text{Si,surf}} = \langle V_{\text{El}} \rangle_{\text{vac}}^{\text{jcn}} - \langle V_{\text{El}} \rangle_{\text{vac}}^{\text{Si}} = \langle \delta V_{\text{H}} \rangle_{\text{vac}}^{\text{jcn}} - \langle \delta V_{\text{H}} \rangle_{\text{vac}}^{\text{Si}} = -\frac{e\,(\Delta\mu_{\text{Si,surf}})}{\epsilon_0\,(\Omega_{\text{Si}})}\,. \tag{4.13}$$

Here, after the first equal sign, there are the nano-smoothed electrostatic potential energies in the top vacuum layer for the junction and for the bare Si wafer; after the second equal sign, there are the corresponding nano-smoothed distorted potential energies; the term after the last equal sign represent the relation between the potential step and the dipole moment change of the silicon surface, $\Delta\mu_{\text{Si,surf}}$, caused by the carboranedithiol adsorption, which is divided by the size of the Si surface taken by one carboranedithiol molecule, $\Omega_{\text{Si}} = \sim 242\ \text{Å}^2$. The dipole change reads: $\Delta\mu_{\text{Si,surf}} = \mu_{\text{Si-Mol}}$

[③] As mentioned is Sec. 3.4.2, the distorted potential energy is defined as the difference between the electrostatic and the neutral-atom potential energies: $\delta V_{\text{H}}(\mathbf{r}) = V_{\text{El}}(\mathbf{r}) - V_{\text{NA}}(\mathbf{r})$.

$-\ \mu_{\mathrm{Si}}$, where μ_{Si} is the dipole moment of the relaxed slab of the dihydride-terminated Si(100) wafer in the unit cell of the corresponding junction[④].

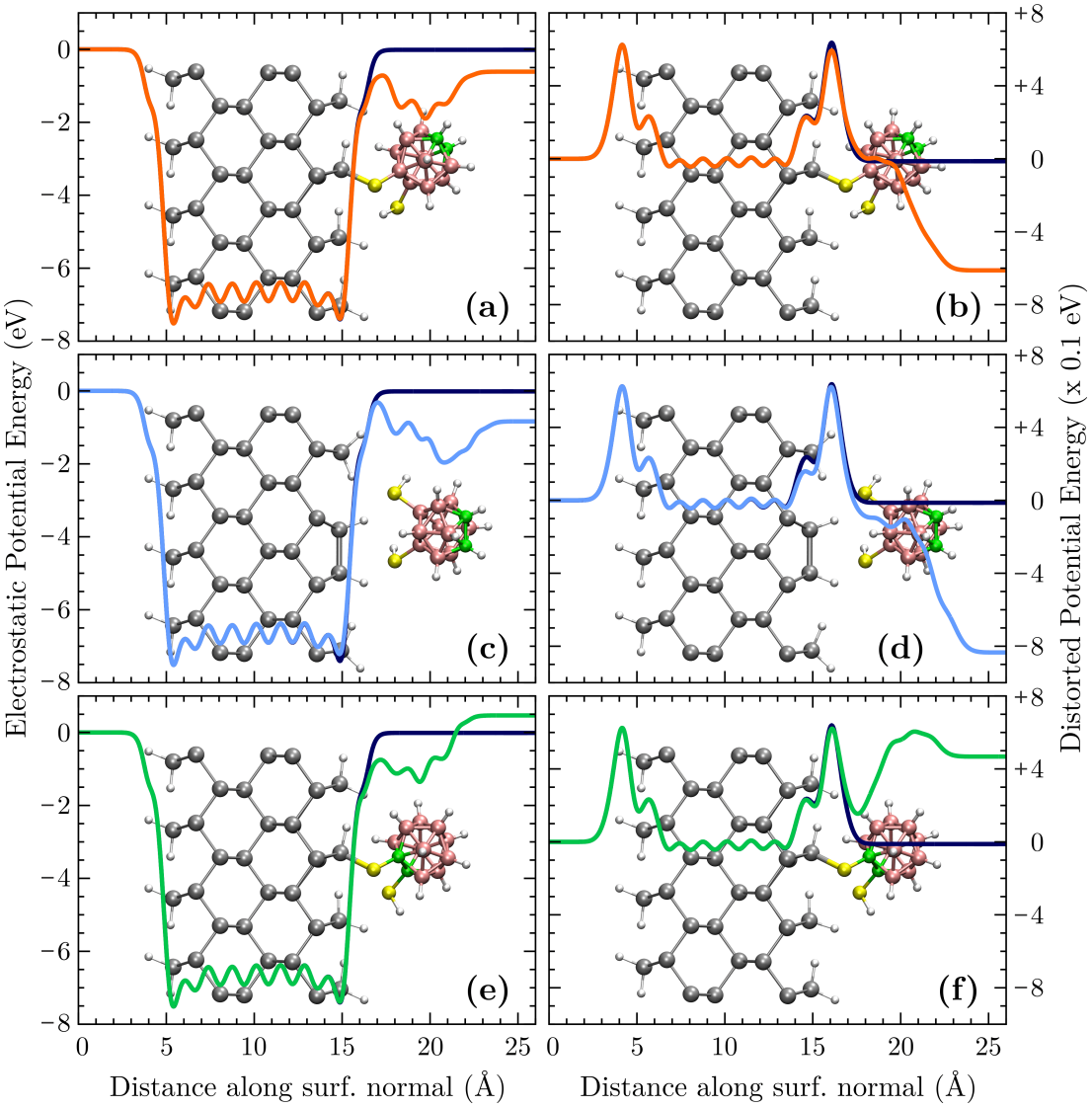

Figure 4.8: Electrostatic potential energy of silicon-molecule junctions. On the left-hand side, there are the plane-averaged electrostatic potential energy profiles across **(a)** the A_{opt}, **(c)** the B_{opt}, and **(e)** the C_{opt}. On the right-hand side, there are the plane-averaged distorted potential energies across **(b)** the A_{opt}, **(d)** the B_{opt}, and **(f)** the C_{opt}. Dark-blue, orange, blue, and green curves belong to the bare dihydride-terminated Si(100) slab, the A_{opt}, the B_{opt}, and the C_{opt} conformations, respectively. In each panel, the inset behind the curve introduce the side view of the final relaxed junction.

In Tab. 4.4, we list the final values of the dipole moment quantities describing the surface dipole changes induced by the molecule adsorption and the equivalent potential energy steps across the adsorbate layer, which we calculate by means of Eq. 4.13. The positive dipole of the B-bonded isomer lowers the electrostatic potential energy above the silicon surface, while the negative dipole of the C-bonded isomer increases it. The more negative $\Delta U_{\mathrm{Si,surf}}$ of the B_{opt} junction is probably a consequence of twice the number of pulled H atoms from the surface compared to the A_{opt} one. Unlike

[④]For each junction conformation, the height of the unit cell is different in order to preserve the thickness of the vacuum layer of ∼12 *Å* at different molecular coordinates.

gold, $\Delta U_{\text{Si,surf}} \neq \Delta\Phi_{\text{Si}}$, as the potential step is only one of two contributions to $\Delta\Phi_{\text{Si}}$ (see Eq. 4). In Sec. 4.6, we find the second contribution, namely the band bending, when studying the silicon band structure shifts induced by the stabilisation of the carboranedithiol-based dipole layer.

Table 4.4: Dipole and potential changes upon adsorption on silicon. Calculated electrostatic features and their changes upon the A_{opt}, the B_{opt}, and the C_{opt} formation: the dipole moment of the silicon-molecule junction, $\mu_{\text{Si-Mol}}$, and the clean dihydride-terminated Si(100) wafer in the unit cell of the junction, μ_{Si}, the dipole moment change of the Si surface upon the carboranedithiol adsorption, $\Delta\mu_{\text{Si,surf}}$, and the Si-surface potential-energy step across the carboranedithiol layer, $\Delta U_{\text{Si,surf}}$. The presented dipole quantities read: $\Delta\mu_{\text{Si,surf}} = \mu_{\text{Si-Mol}} - \mu_{\text{Si}}$. From the third column, we calculate the fourth column according to the relation: $\Delta U_{\text{Si,surf}} = -e(\Delta\mu_{\text{Si,surf}})/(\epsilon_0(\Omega_{\text{Si}}))$ (see 4.13), where $\Omega_{\text{Si}} \approx 241.769\ \mathring{A}^2$.

	$\mu_{\text{Si-Mol}}\ (D)$	$\mu_{\text{Si}}\ (D)$	$\Delta\mu_{\text{Si,surf}}\ (D)$	$\Delta U_{\text{Si,surf}}\ (eV)$
A_{opt}	+3.928	+0.087	+3.841	−0.599
B_{opt}	+5.354	+0.084	+5.270	−0.821
C_{opt}	−3.002	+0.075	−3.077	+0.480

In this section, without studying the silicon band structure, we get the total $\Delta\Phi_{\text{Si}}$ through the calculation of the line-up term, $\Delta\langle\delta V_{\text{H}}\rangle$ (Eq. 3.5), the vacuum level, E_{vac} (Eq. 3.6), and the Fermi level, E_{F} (Eq. 3.7). In Tab. 4.5, we present all the mentioned quantities with respect to the bulk reference, i.e. $\langle V_{\text{El}}\rangle_{\text{bulk}} \equiv 0$. The chemisorbed ($A_{\text{opt}}$) and the physisorbed B-bonded isomers (B_{opt}) reduce the work function of the H_2-passivated Si(100) wafer by 0.446 and 0.922 eV, respectively, while the chemisorbed C-bonded isomer (C_{opt}) increases it by 0.723 eV. Therefore, the range of changes is more than 1.6 eV, making it smaller by more than 0.8 eV compared to the gold-molecule junctions (see part 3.4.3) where the molecular dipoles are straightened along the surface normal and more densely occupy the surface ($\Omega_{\text{Au}} < \Omega_{\text{Si}}$). On the other hand, compared to experimental data on another semiconductor substrates [121], our range on silicon is noticeably larger.

Table 4.5: Electrostatic-potential features accompanying adsorption on silicon. Calculated values of the electrostatic-potential quantities with respect to the bulk reference describing the A_{opt}, the B_{opt}, and the C_{opt} conformations, and the bare dihydride-terminated Si(100) wafer in the unit cell of one of the junctions: the line-up term, $\Delta\langle\delta V_{\text{H}}\rangle$ (eV), the vacuum level, E_{vac} (eV), the Fermi level, E_{F} (eV), the surface work function, Φ (eV), and the work function change of the silicon substrate, $\Delta\Phi_{\text{Si}}$ (eV). We employ $\langle V_{\text{El}}\rangle_{\text{bulk}} = -6.737\ eV$.

	$\Delta\langle\delta V_{\text{H}}\rangle$	E_{vac}	E_{F}	Φ	$\Delta\Phi_{\text{Si}}$
A_{opt}(Si)	+0.006	6.743	2.228	4.514	/
A_{opt}(jcn)	−0.593	6.144	2.076	4.069	−0.446
B_{opt}(Si)	+0.006	6.743	2.228	4.515	/
B_{opt}(jcn)	−0.815	5.922	2.329	3.593	−0.922
C_{opt}(Si)	+0.008	6.745	2.228	4.516	/
C_{opt}(jcn)	+0.487	7.224	1.985	5.240	+0.723

4.5 Mechanical properties

In this section, we examine the mechanical properties of the chemisorbed junctions upon their stretching to characterise the forces acting between the molecule and the Si surface (part 4.5.1) and the Si-S bond strength of each carboranedithiol isomer (part 4.5.2).

4.5.1 Chemisorbed junction stretching

We take the stable geometries of the A_{opt} and the C_{opt} junctions and then gradually pull the molecule away from the silicon surface. Specifically, in each step, we shift the molecular atoms and the H atom bonded to the S atom away from the Si surface along the direction of the Si-S connector by 0.1 *Å*. After each incremental shift, we stabilise the junction structure by means of the geometry-relaxation procedure (see Sec. 4.2). To avoid having the molecule snap back to its original geometry, we constrain the z-coordinate of the topmost atom of the carborane cage, namely the higher C atom of the B-bonded isomer and the highest B atom of the C-bonded isomer. In this way, we obtain a series of local minima as a function of the junction elongation which we plot in top left panels of Fig. 4.9 and 4.10 for the B-bonded and the C-bonded junctions, respectively. In these plots, we express each local minimum in terms of the total energy of the given structure with respect to the energy of the A_{opt} and the C_{opt} junctions, respectively.

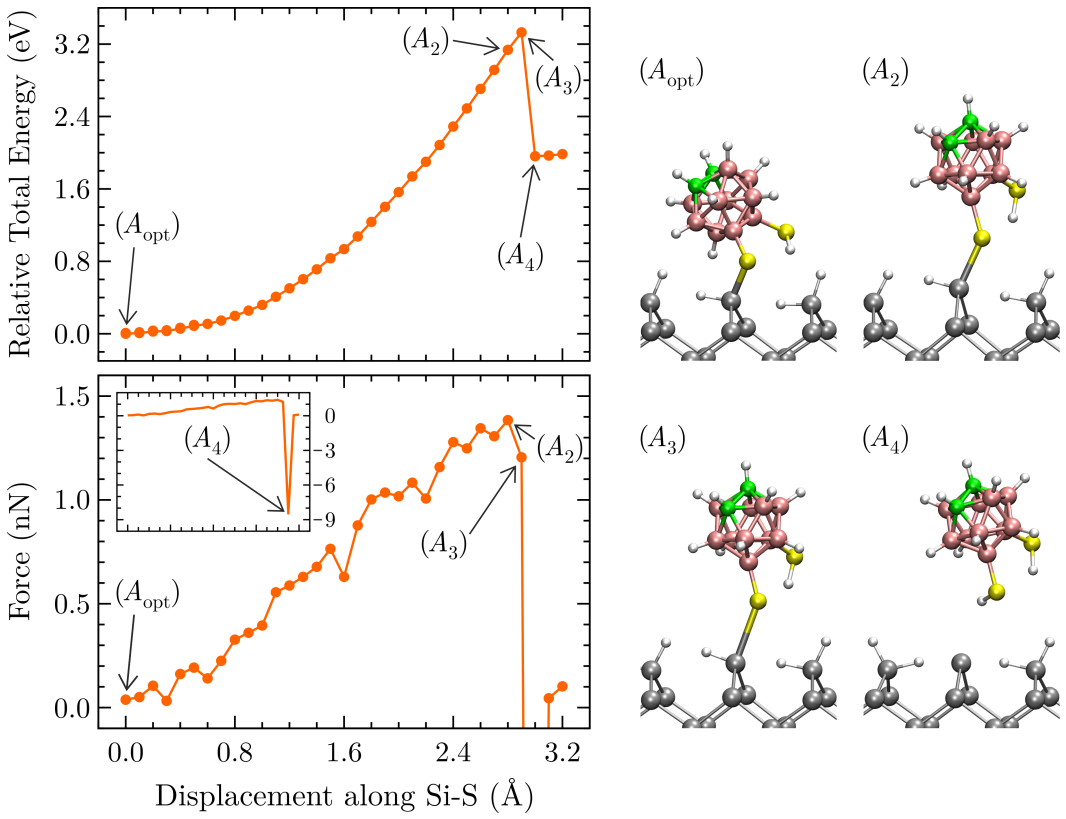

Figure 4.9: Mechanical stretching of A_{opt} junction. Mechanical pulling of the chemisorbed B-bonded carboranedithiol isomer from the silicon surface. On the left-hand side, there are (top left panel) the relative total energy of the junction as a function of the displacement of the carborane cage along the Si-S connector direction, and (bottom left panel) the associated force acting between the substrate and the adsorbate. On the right-hand side, there are the snapshots of the pulling path of the molecule at the displacements of: (A_{opt}) 0.0, (A_2) 2.8, (A_3) 2.9, and (A_4) 3.0 *Å*.

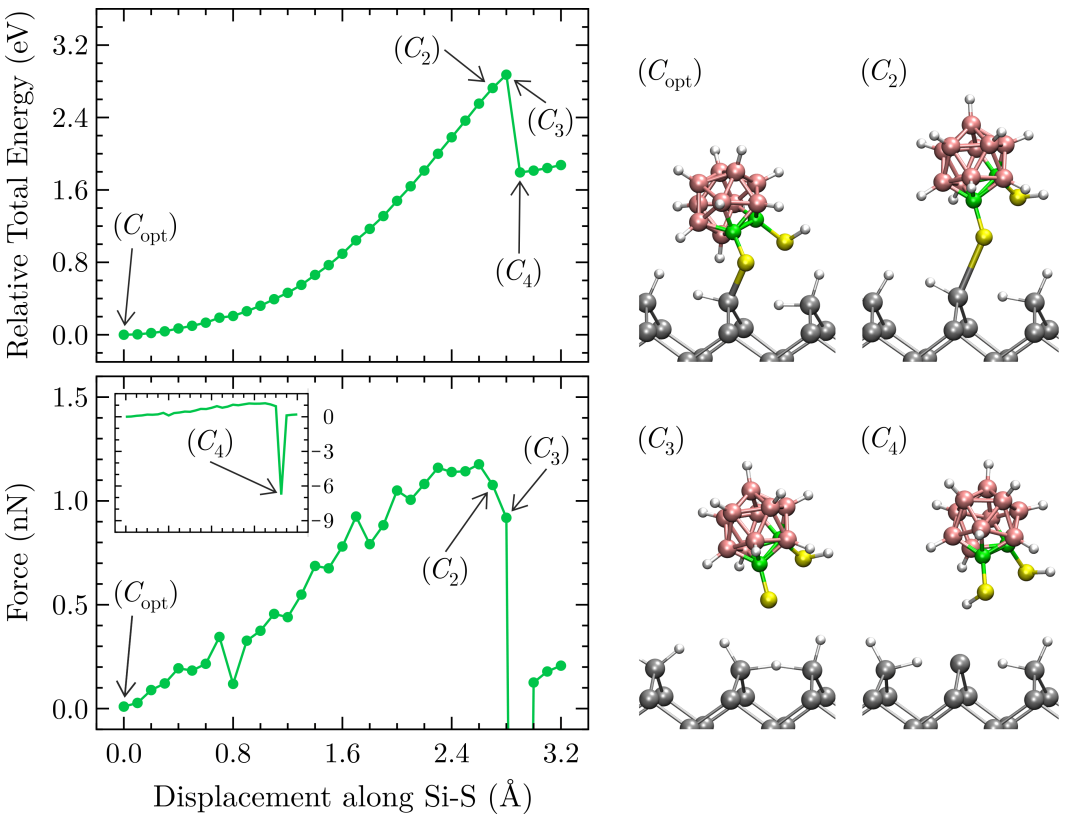

Figure 4.10: Mechanical stretching of C_{opt} junction. Mechanical pulling of the chemisorbed C-bonded carboranedithiol isomer from the silicon surface. Top and bottom right panels characterise the same functions as in Fig. 4.9. On the right-hand side, there are the snapshots of the pulling path of the molecule at the displacements of: (C_{opt}) 0.0, (C_2) 2.7, (C_3) 2.8, and (C_4) 2.9 *Å*.

From the total energy data, we calculate the forces as the numerical derivative of the total energy with respect to the vertical displacement via the backward difference formula. We depict the force dependencies associated with the total energies in bottom left panels of Fig. 4.9 and 4.10. The positive value of the calculated force means the molecule would spring back to the Si surface if the constraint on the z-coordinate of the topmost atom of the carborane cage were removed.

As we gradually lift the molecule, the carborane cage rotates to reduce the tilt angle of the molecule, while the Si-S bond length remains almost unchanged. Regarding the B-bonded junction, by further elongation of the geometry, the Si-S bond is stretched from an initial length of 2.19 *Å*[5] to a maximum of 3.15 *Å* before its rupture (Fig. 4.9, A_3 snapshot at the displacement of 2.9 *Å*), accompanied by a maximum induced force of 1.38 *nN* (bottom left panel, A_2 snapshot at the displacement of 2.8 *Å*). This is followed by the Si-S bond breaking, the pulled bonding Si atom is released back towards the wafer, and the H atom originally bonded to this Si is drawn towards the S of the carborane cage, making the molecule fully saturated (A_4 snapshot at the displacement of 2.8 *Å*). The originally bonding Si atom ends up in a divalent state, only bonded to two other (subsurface) Si atoms of the substrate.

In the case of the C-bonded junction, the Si-S bond is lengthened from 2.23 to 3.12 *Å* (Fig. 4.10, C_2 snapshot at the displacement of 2.7 *Å*), with a maximum sustained force of 1.18 *nN* (bottom left panel, at the displacement of 2.6 *Å*). Unlike the B-bonded isomer, further elongation of the C-bonded junction results in a certain vdW structure

[5] The experimentally observed Si-S bond length is reported between ∼2.12 and ∼2.20 *Å* [122, 123].

(C_3 snapshot at the displacement of 2.8 $\AA$) in which the carborane cage is kept close to the surface due to attractive forces between the S and the two nearest surface Si atoms. In the end, however, the vdW complex transforms into the final conformation (C_4 snapshot at the displacement of 2.9 $\AA$) that is structurally similar to the B-bonded counterpart.

The stress introduced by pulling and constraining the molecule away from the surface is reflected in the roughly monotonic increase of the total energy in top left panels of Fig. 4.9 and 4.10. The associated force increases progressively, with occasional small drops (e.g. at the displacement of 0.3, 1.6, or 2.2 $\AA$ in Fig. 4.9 and 0.8, 1.8, or 2.1 $\AA$ in Fig. 4.10) caused mainly by the rotation of the carborane cage. As for the induced bond-rupture forces of Si-S bond, our results of 1.38 and 1.18 nN for the B-bonded and the C-bonded junctions, respectively, fall within the range of reported values for covalent bonds having one identical atomic species [124]. Specifically, through DFT simulations, from ~2.2 to ~2.9 nN is reported for the Si-Si [125], ~2.8 nN for the Si-C [124, 126], ~2.7 nN for the Au-S [127], and ~1.5 nN for the S-S [128]. However, the results obtained by force microscopy techniques give the lower values, namely ~2.1 nN for the Si-Si [129], ~2.0 nN for the Si-C [124, 126], and ~1.4 nN for the Au-S [127].

4.5.2 Si-S bond strength

From mechanical simulations of the chemisorbed junction stretching, we can calculate the strength of the Si-S bond through a linear fitting of the initial slope of the force curve with respect to the bond elongation. In Fig. 4.11(a) and (b), we show the calculated force as a function of the Si-S bond length for the B-bonded and the C-bonded junctions, respectively. We employ the force data from Fig. 4.9 up to the displacement of 2.8 $\AA$ and from Fig. 4.10 up to the displacement of 2.6 $\AA$. From the linear fit of the first 12 data points in Fig. 4.11(a) and the first 8 data points in Fig. 4.11(b), we get the Si-S bond strength of 22.3 and 13.1 $nN{\cdot}\AA^{-1}$, respectively. The B-bonded value is very close to the reported one of 22.0 $nN{\cdot}\AA^{-1}$ [122, 123] while the C-bonded value is noticeably smaller.

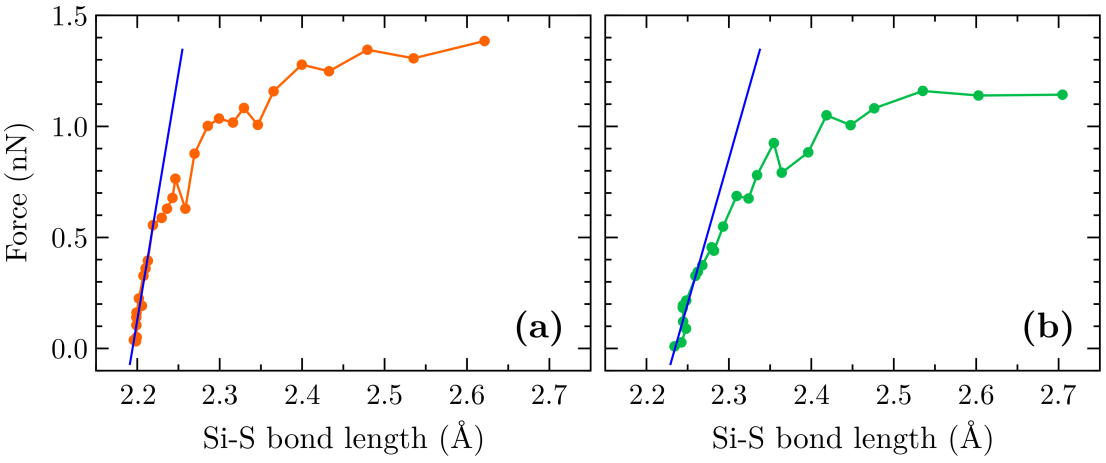

Figure 4.11: Mechanical features of Si-S bond. Calculated force between the molecule and the Si substrate as a function of the Si-S bond length in the stretched geometries of **(a)** the A_{opt} and **(b)** the C_{opt} junctions. The blue lines indicate the initial slope of the force vs. the Si-S bond length obtained by the linear fitting of the first 12 and the first 8 data points in the case of the A_{opt} and the C_{opt} junctions, respectively. In (a) panel, the fit gives: $f(x) = 22.263x - 48.852$; in (b) panel: $f(x) = 13.056x - 29.174$.

4.6 Band properties of substrate

To complete the whole issue of the silicon-molecule junctions, we need to clarify the effect of the molecular dipole layer on the band features of the silicon wafer, representing the main topic of this section. In the first part of this section (part 4.6.1), we are interested in the relative shifts of the silicon band structure caused by the carboranedithiol adsorption. Then, in the second part (part 4.6.2), we combine our results on the electronic properties from part 4.4.2 and the Si band properties from part 4.6.1 to describe in detail the course of the surface transfer doping of the dihydride-terminated Si(100) wafer as the substrate for the A_{opt}, the B_{opt}, and the C_{opt} conformations.

4.6.1 Silicon band structure shift

As we already know from Sec. iii, changing the silicon work function is not only a question of modifying the electrostatic potential energy above the surface (part 4.4.2) but also a question of modifying the electronic features inside the silicon substrate, namely changing the silicon band structure. We observe this last-mentioned change via the carboranedithiol-mediated band structure shift with respect to the energy axis.

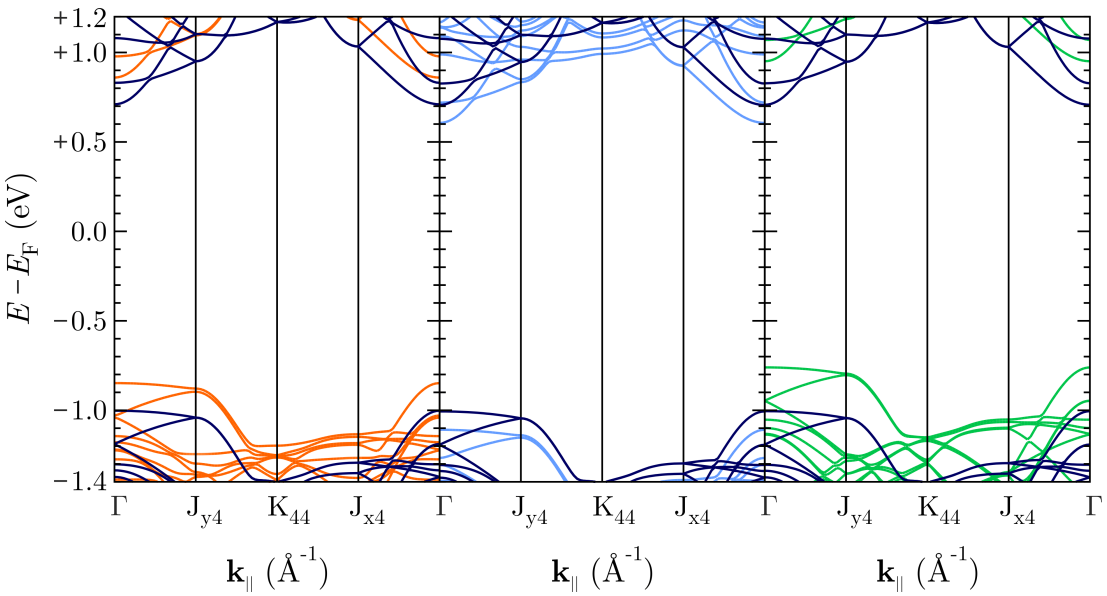

Figure 4.12: Carboranedithiol-mediated Si band structure shift. The electronic energy levels of Si chemical species as functions of the position along the **k**-point path: Γ → J_{y4} → K_{44} → J_{x4} → Γ. Dark-blue, orange, blue, and green lines indicate the Si features of the bare dihydride-terminated Si(100) wafer, the A_{opt} (left panel), the B_{opt} (middle panel), and the C_{opt} junctions (right panel), respectively. All presented structures have the Fermi level shifted to zero and a direct band gap of $E_{\mathrm{g}} \approx 1.71\ eV$.

In Fig. 4.12, we show the band structures projected on Si chemical species for the bare dihydride-terminated Si(100) wafer (dark-blue lines), the A_{opt} (left panel, orange lines), the B_{opt} (middle panel, blue lines), and the C_{opt} junctions (right panel, green lines). We shift the Fermi level of each of these structures to zero, leading to the Fermi level alignment and relative displacements between the Si features of the silicon-molecule junctions and the bare silicon wafer. Specifically, at the valence-band edge, the orange, the blue, and the green lines are shifted relative to the dark-blue one by $+0.157$, -0.103, and $+0.245\ eV$, respectively. At the conduction-band edge, the shifts are $+0.152$, -0.100, and $+0.243\ eV$, respectively, and do not match the valence-band values due to a slight modification of the band gap caused by the carboranedithiol

adsorption. In particular, the band-gap energies of the bare silicon wafer, the A_{opt}, the B_{opt}, and the C_{opt} conformations are 1.713, 1.708, 1.715, and 1.711 eV, respectively. The developments of individual Si bands along the **k**-point path are not affected by the adsorption, only the almost rigid shifts of the Si spectrum occur, which is upward for the A_{opt} and the C_{opt} and downward for the B_{opt}.

4.6.2 Surface transfer doping of Si(100)

Due to the sufficient electrostatic separation of both sides of the our 8-layer silicon slab (see part 2.2.5, Fig. 2.10), we can interpret the carboranedithiol-mediated band structure shift inside this slab as the band bending in the energy diagram of the silicon-molecule junction composed of a semi-infinite wafer (see Sec. iii, Fig. 2 and 3).

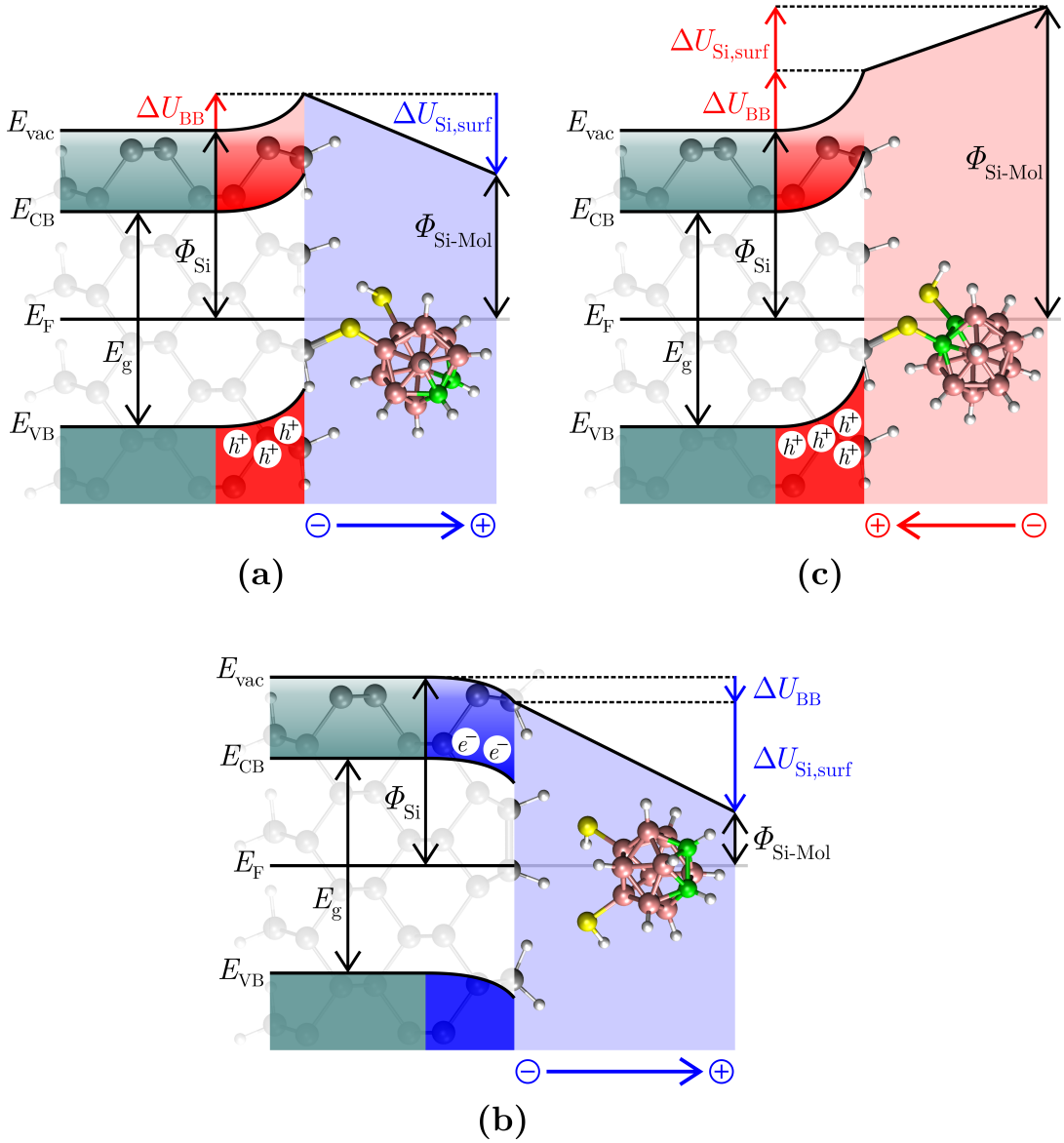

Figure 4.13: Carboranedithiol-mediated surface transfer doping of Si(100). Energy diagram of **(a)** the A_{opt}, **(b)** the B_{opt}, and **(c)** the C_{opt} junctions. Green, red, and blue coloured parts indicate the region of the intrinsic silicon and the regions of the rise and the fall of the electrostatic potential energy along the surface normal, respectively. White circles with "h^+" and "e^-" labels mark accumulated holes and electrons, respectively.

In Fig. 4.13(a), (b), and (c), we depict the proposed energy diagrams of the A_{opt},

the B_{opt}, and the C_{opt} junctions, respectively, where we always regard the left (bottom) side of the wafer as the bulk-like region. The surface-normal direction corresponds to proceeding from left to right across each panel. We provide a detailed analysis of all cross-sectional parts of the energy diagrams and the marked energy quantities in Sec. iii. Regarding the energy quantities, we list the values of $\Delta\mu_{\mathrm{Si,surf}}$ in Tab. 4.4 and the values of Φ_{Si} and $\Phi_{\mathrm{Si\text{-}Mol}}$ in Tab. 4.5. Moreover, from Tab. 4.5, we calculate the band bending from the differences between the Fermi levels of the bare silicon substrate and the final junction conformation. For the A_{opt}, the B_{opt}, and the C_{opt} junctions, we get $\Delta U_{\mathrm{BB}} = +0.153$, -0.101, and $+0.244$ eV, respectively. Thus, in the case of chemisorbed structures, the p-type doping of the Si surface occurs, with the C-bonded isomer being a stronger p-type dopant. The chemisorbed B-bonded isomer mediates the n-type doping of the silicon wafer. We can explain the relative differences between the values of ΔU_{BB} in terms of the charge density difference profiles (Fig. 4.7) where, based on numerical integration up to the right (top) passivation layer, the greatest accumulation of electrons occurs in the B_{opt} case and the lowest one in the C_{opt} case.

Surface transfer doping is also accompanied by the changes in molecular levels relative to the silicon band edges. At the formation of each conformation, we notice a decrease in molecular energies, which can be explained by the stabilisation of the carboranedithiol during the adsorption[6]. As for the position of the LUMO energy above the conduction-band minimum, i.e. E_{LUMO} - E_{CB}, we observe the largest and the lowest decreases in the case of B_{opt} and C_{opt}, respectively. The same applies to the barrier height for electron injection, i.e. ΔU_{e}. The fact that there are no positive changes in ΔU_{e} (or in E_{LUMO} - E_{CB}) in the p-type structures is caused by the adsorption-induced decrease in carboranedithiol levels in all studied junctions. So only the relative differences of these quantities between the studied structures give us a reasonable comparison.

Regarding the position of the valence-band maximum above the HOMO energy, i.e. E_{VB} - E_{HOMO}, or the barrier height for hole injection, i.e. ΔU_{h}, we get no reasonable comparison. Due to the adsorption-induced decrease in molecular levels, these quantities increase for each junction formation. However, the relative differences in the increase of ΔU_{h} (or E_{VB} - E_{HOMO}) between the studied structures do not predict the relative differences in the silicon band structure shift. The reason is probably the influence of the formation of Si-S or S-H bonds on the HOMO level, the main part of which is made up of states of sulphur atoms; the LUMO level is mainly made up of states of backbone atoms. In addition, there are also significant changes in the HOMO-LUMO gap, which are quite different for both carboranedithiol isomers, namely ~ -0.45 and $\sim +0.38$ eV for the B-bonded and the C-bonded molecule.

[6] As we state in Sec. 4.1, the adsorption proceeds by a radical mechanism [118] in which the molecule enters with originally unsaturated thiol linker groups, each carrying a free radical. Radical elimination, which is the driving force of the adsorption, significantly stabilises the molecule.

5. Summary

In this thesis, by means of theoretical calculations based on a density functional theory (DFT), we investigate various conformations of the gold-carboranedithiol and the silicon-carboranedithiol junctions and their isolated subsystems. We divide the thesis into the introduction and the four chapters, the last two of which include the main outputs of our research. We have presented our results at seven scientific conferences, published in two papers and one more is in preparation (see more details in List of publications).

In the introduction, we mainly deal with fundamental semiconductor doping strategies, with a subsequent emphasis on the surface transfer doping (STD) of the silicon surface. We provide fundamental ideas about the band bending, ΔU_{BB}, inside the silicon and the electrostatic potential energy change above the silicon surface, $\Delta U_{\mathrm{Si,surf}}$, caused by the molecular-dipole adsorption. By summing these quantities, we get the change of the silicon work function, $\Delta\Phi_{\mathrm{Si}}$. In the first chapter, we review the grounds of the DFT approach and the DFT-SIESTA implementation, primarily intended for large periodic systems.

In the second chapter, we are interested in the bare Au and Si surfaces and the isolated carborane-based molecules. We optimise the bulk properties of both crystalline solids and perform the structural and the electronic descriptions of the Au(111) and the dihydride-terminated Si(100) wafers. When constructing the Si(100), we find the thickness of 8 Si layers represents the minimum for the sufficient electrostatic separation of both wafer sides.

After studying the solids, we deal with the geometric and the electronic properties of the isolated carborane molecule and the two positional isomers of the carboranedithiol derivatives, each possessing a large molecular dipole. We denote the dithiolated derivatives as the B-bonded or the C-bonded isomers as they have two sulphur atoms attached to either two adjacent carbon atoms or opposite boron atoms of the carborane cage, respectively. These isomers react with substrate via a radical-initiated reaction. Therefore, we only investigate them with H-unsaturated thiol linker groups.

In the third chapter, we investigate the structural and the electronic properties of the gold-molecule junctions, resulting from the adsorption of the B-bonded or the C-bonded positional isomers on the Au(111) wafer composed of 4 Au layers. We sample a large number of interface geometries exploring a wide range of carborane-cage orientations. We see the strong Au-S bonds are the main driving mechanism determining the junction geometry. In particular, the preferred chemisorption of the S atom near hollow sites on Au, the atomic rearrangement of the top Au layer caused by the molecule-mediated pulling of some Au atoms from the surface, and the molecule tilting, are largely caused by the strong Au-S bonds. All these structural changes lead to more stable junctions.

From the stable geometries, we choose two conformations composed of the vertically adsorbed molecules, one of the B-bonded and the other of the C-bonded isomers, each providing the largest possible projection of the molecular dipole along the surface normal and therefore the greatest influence on the electrostatic properties of the substrate. For both vertical junctions, we observe the creation of the negative interfacial dipole at the gold-molecule interface, primarily caused by the Au-S bonds formation. Upon the chemisorption of the B-bonded molecule, the electrostatic potential energy above the Au surface is changed by $\Delta U_{\mathrm{Au,surf}} = -1.284\ eV$ because of the molecular

dipole pointed away from the surface. On the other hand, the dipole of the C-bonded molecule is pointed towards the surface, giving rise to the opposite potential change, namely $\Delta U_{\mathrm{Au,surf}} = +1.186$ eV. Thus, by means of carborane-cage-based molecules, we are able to tune the gold work function in the range of units of eV, making our data comparable to those reported experimentally on metals.

We report the most important outputs of our research in the final fourth chapter on the silicon-molecule junctions, arising from the adsorption of the B-bonded or the C-bonded carboranedithiols on the dihydride-terminated Si(100) wafer composed of 8 Si layers. From a large number of junction geometries, we identify three groups of stable adsorption configurations, referred to as groups A, B, and C, involving the chemisorbed and the physisorbed B-bonded molecule and the chemisorbed C-bonded molecule, respectively. Chemisorbed junctions are formed when one unsaturated thiol group replaces one surface H atom to bind strongly to the substrate via a single Si-S bond; the one replaced H atom saturates the other thiol group. Physisorbed structures result from two H atoms being transferred from the Si surface to saturate both molecular thiol groups; two adjacent dangling bonds remaining on the surface recombine to form a Si-Si dimer. From the groups of stable junction configurations, we select the lowest-energy conformations, denoting as A_{opt}, B_{opt}, and C_{opt}.

For all lowest-energy conformations, we observe the formation of the positive interfacial dipole, primarily induced by surface H atoms being pulled from the surface and, upon chemisorption, also by the negative contribution of the Si-S bond formation. The A_{opt} and the B_{opt} formations change the electrostatic potential energy above the Si surface by $\Delta U_{\mathrm{Si,surf}} = -0.599$ and -0.821 eV, respectively, as the consequence of the molecular dipole pointed away from the surface and the number of transferred surface H atoms towards the molecule; this number is doubled in the case of physisorption, making $\Delta U_{\mathrm{Si,surf}}$ more negative. On the contrary, the C_{opt} formation gives rise the change of $\Delta U_{\mathrm{Si,surf}} = +0.480$ eV due to the molecular dipole pointed towards the Si surface, partially offset by one pulled H atom from the wafer.

Having in mind the band gap of the wafer is the difference of the band edges composed of Si states, the molecule adsorption does not modify this property as molecular features are not present close to the gap, nor do they induce any gap states in it. The A_{opt} and the C_{opt} formations bend the band edges below the Si surface upwards, namely by 0.153 and 0.244 eV, respectively, resulting in the p-type STD of the Si wafer. In contrast, the B_{opt} formation bends the Si states downwards by 0.101 eV, revealing the n-type STD of the slab. Therefore, we observe the shift of the Fermi level in the silicon band gap due to the effect of the adsorbed dipole, creating a certain application potential for carborane molecules in the field of photovoltaics.

Conclusion

By obtaining stable conformations of the silicon-carboranedithiol junctions, we notice shifts of the Fermi level in the silicon band gap in the order of hundreds of meV in both directions. If we consider such a range of changes in the band gap of conventionally doped c-Si at a temperature of 300 K, we get a rough estimate of dopant concentrations in the studied junctions. Specifically, the chemisorbed B-bonded (A_{opt}) or C-bonded (C_{opt}) structures, with the band bending of $\Delta U_{\text{BB}} = +0.153$ or $+0.244$ eV, respectively, reach the dopant concentrations of $\sim 3 \times 10^{12}$ or $\sim 1 \times 10^{14}$ cm^{-3}, respectively. These values potentially brings us into the area of light level ($< 10^{14}$ cm^{-3}) or the limit of light/moderate levels of p-type doping, respectively. In the case of the physisorbed B-bonded (B_{opt}) junction with $\Delta U_{\text{BB}} = -0.101$ eV, we achieve the concentration of $\sim 5 \times 10^{11}$ cm^{-3}, i.e. the area of light n-type doping.

In our third paper, which we are still working on, we investigate all three stable conformations by means of molecular dynamics simulations at 300 K and probe the time evolution of the Si band bending during the system propagation. From the mean values obtained from the specified time intervals, we get noticeable signs of non-invasive silicon doping. Although our results only reach the area of light level of doping (band bending does not exceed 100 meV in any direction), we observe a time-consistent evolution of electronic features that points out to the potential ability of carborane molecules, or their related analogues, to be used in photovoltaic research.

The scope of research on cage-like molecules with a large intrinsic dipole adsorbed on silicon surfaces has been very limited so far. Our work emphasises the potential and impact of the silicon-carboranedithiol junctions in photovoltaic applications by means of non-invasive surface transfer doping strategy. Since there are practically no experimental or theoretical works investigating either these or related geometries, our work is probably the first demonstration of the electronically active self-assembled monolayers on the silicon substrates. With this thesis, we hope to increase the chance of opening a new research direction in the field of photovoltaics, not only for carboranes but also for other related molecules. By increasing the variety of suitable molecular candidates, we can enhance the probability of their usage not only for theoretical but also for experimental applications.

Bibliography

[1] International Renewable Energy Agency *Global Renewables Outlook: Energy transformation 2050*; IRENA: Abu Dhabi, 2020.

[2] International Energy Agency *World Energy Outlook 2022*; World Energy Outlook; IEA: Paris, 2022.

[3] Philipps, S.; Warmuth, W. *Photovoltaics Report*; Fraunhofer Institute for Solar Energy Systems: Freiburg, 2021; [Online; accessed 27-October-2021].

[4] C. Raval, M.; Madugula Reddy, S. In *Solar Cells*; Nayeripour, M., Mansouri, M., Waffenschmidt, E., Eds.; IntechOpen, 2020.

[5] Fischer, M., Woodhouse, M., Herritsch, S., Trube, J., Eds. *International Technology Roadmap for Photovoltaic: 2020 Results*, 12th ed.; VDMA e.V. Photovoltaic Equipment: Frankfurt am Main, 2021.

[6] Solar Price | EnergyTrend. https://www.energytrend.com/solar-price.html, [Online; accessed 12-November-2021].

[7] ITRPV *International Technology Roadmap for Photovoltaic: 2013 Results*, 5th ed.; SEMI: Berlin, 2014.

[8] Colville, F. Monocrystalline cells dominate solar photovoltaic industry, but technology roadmap is far from certain. *Laser Focus World* **2020**, *56*, 30–34, [Online; accessed 13-May-2021].

[9] Wilson, G. M. et al. The 2020 photovoltaic technologies roadmap. *J. Phys. D: Appl. Phys.* **2020**, *53*, 493001.

[10] Smets, A. H. M.; Jäger, K.; Isabella, O.; Swaaij, R. v.; Zeman, M. *Solar Energy: The physics and engineering of photovoltaic conversion, technologies and systems*; UIT Cambridge: Cambridge, England, 2016.

[11] Ho, J. C.; Yerushalmi, R.; Jacobson, Z. A.; Fan, Z.; Alley, R. L.; Javey, A. Controlled nanoscale doping of semiconductors via molecular monolayers. *Nat. Mater.* **2008**, *7*, 62–67.

[12] Ye, L.; Pujari, S. P.; Zuilhof, H.; Kudernac, T.; de Jong, M. P.; van der Wiel, W. G.; Huskens, J. Controlling the Dopant Dose in Silicon by Mixed-Monolayer Doping. *ACS Appl. Mater. Interfaces* **2015**, *7*, 3231–3236.

[13] Chen, W.; Qi, D.; Gao, X.; Wee, A. T. S. Surface transfer doping of semiconductors. *Prog. Surf. Sci.* **2009**, *84*, 279–321.

[14] Veerbeek, J.; Huskens, J. Applications of Monolayer-Functionalized H-Terminated Silicon Surfaces: A Review. *Small Methods* **2017**, *1*, 1700072.

[15] Fabre, B. Functionalization of Oxide-Free Silicon Surfaces with Redox-Active Assemblies. *Chem. Rev.* **2016**, *116*, 4808–4849.

[16] Smith, R. K.; Lewis, P. A.; Weiss, P. S. Patterning self-assembled monolayers. *Prog. Surf. Sci.* **2004**, *75*, 1–68.

[17] Love, J. C.; Estroff, L. A.; Kriebel, J. K.; Nuzzo, R. G.; Whitesides, G. M. Self-Assembled Monolayers of Thiolates on Metals as a Form of Nanotechnology. *Chem. Rev.* **2005**, *105*, 1103–1170.

[18] Gooding, J. J.; Ciampi, S. The molecular level modification of surfaces: from self-assembled monolayers to complex molecular assemblies. *Chem. Soc. Rev.* **2011**, *40*, 2704–2718.

[19] Ye, L.; González-Campo, A.; Núñez, R.; de Jong, M. P.; Kudernac, T.; van der Wiel, W. G.; Huskens, J. Boosting the Boron Dopant Level in Monolayer Doping by Carboranes. *ACS Appl. Mater. Interfaces* **2015**, *7*, 27357–27361.

[20] Ishii, H.; Sugiyama, K.; Ito, E.; Seki, K. Energy Level Alignment and Interfacial Electronic Structures at Organic/Metal and Organic/Organic Interfaces. *Adv. Mater.* **1999**, *11*, 605–625.

[21] Flores, F.; Ortega, J.; Vázquez, H. Modelling energy level alignment at organic interfaces and density functional theory. *Phys. Chem. Chem. Phys.* **2009**, *11*, 8658–8675.

[22] Vilan, A.; Cahen, D. Chemical Modification of Semiconductor Surfaces for Molecular Electronics. *Chem. Rev.* **2017**, *117*, 4624–4666.

[23] Cahen, D.; Kahn, A. Electron Energetics at Surfaces and Interfaces: Concepts and Experiments. *Adv. Mater.* **2003**, *15*, 271–277.

[24] Cahen, D.; Naaman, R.; Vager, Z. The Cooperative Molecular Field Effect. *Adv. Funct. Mater.* **2005**, *15*, 1571–1578.

[25] He, T.; Ding, H.; Peor, N.; Lu, M.; Corley, D. A.; Chen, B.; Ofir, Y.; Gao, Y.; Yitzchaik, S.; Tour, J. M. Silicon/Molecule Interfacial Electronic Modifications. *J. Am. Chem. Soc.* **2008**, *130*, 1699–1710.

[26] Hacker, C. A. Modifying electronic properties at the silicon–molecule interface using atomic tethers. *Solid State Electron.* **2010**, *54*, 1657–1664.

[27] Barber, H. D. Effective mass and intrinsic concentration in silicon. *Solid State Electron.* **1967**, *10*, 1039–1051.

[28] Bludau, W.; Onton, A.; Heinke, W. Temperature dependence of the band gap of silicon. *J. Appl. Phys.* **1974**, *45*, 1846–1848.

[29] Hunger, R.; Jaegermann, W.; Merson, A.; Shapira, Y.; Pettenkofer, C.; Rappich, J. Electronic Structure of Methoxy-, Bromo-, and Nitrobenzene Grafted onto Si(111). *J. Phys. Chem. B* **2006**, *110*, 15432–15441.

[30] Anagaw, A. Y.; Wolkow, R. A.; DiLabio, G. A. Theoretical Study of Work Function Modification by Organic Molecule-Derived Linear Nanostructure on H-Silicon(100)-2 × 1. *J. Phys. Chem. C* **2008**, *112*, 3780–3784.

[31] Baše, T.; Bastl, Z.; Plzák, Z.; Grygar, T.; Plešek, J.; Carr, M. J.; Malina, V.; Šubrt, J.; Boháček, J.; Večerníková, E.; Kříž, O. Carboranethiol-Modified Gold Surfaces. A Study and Comparison of Modified Cluster and Flat Surfaces. *Langmuir* **2005**, *21*, 7776–7785.

[32] Baše, T.; Bastl, Z.; Šlouf, M.; Klementová, M.; Šubrt, J.; Vetushka, A.; Ledinský, M.; Fejfar, A.; Macháček, J.; Carr, M. J.; Londesborough, M. G. S. Gold Micrometer Crystals Modified with Carboranethiol Derivatives. *J. Phys. Chem. C* **2008**, *112*, 14446–14455.

[33] Lübben, J. F.; Baše, T.; Rupper, P.; Künniger, T.; Macháček, J.; Guimond, S. Tuning the surface potential of Ag surfaces by chemisorption of oppositely-oriented thiolated carborane dipoles. *J. Colloid Interface Sci.* **2011**, *354*, 168–174.

[34] Baše, T.; Bastl, Z.; Havránek, V.; Macháček, J.; Langecker, J.; Malina, V. Carboranedithiols: Building Blocks for Self-Assembled Monolayers on Copper Surfaces. *Langmuir* **2012**, *28*, 12518–12526.

[35] Wann, D. A.; Lane, P. D.; Robertson, H. E.; Baše, T.; Hnyk, D. The gaseous structure of closo-9,12-$(SH)_2$-1,2-$C_2B_{10}H_{10}$, a modifier of gold surfaces, as determined using electron diffraction and computational methods. *Dalton Trans.* **2013**, *42*, 12015–12019.

[36] Baše, T.; Macháček, J.; Hájková, Z.; Langecker, J.; Kennedy, J. D.; Carr, M. J. Thermal isomerizations of monothiolated carboranes (HS)C2B10H11 and the solid-state investigation of 9-(HS)-1,2-C2B10H11 and 9-(HS)-1,7-C2B10H11. *J. Organomet. Chem.* **2015**, *798*, 132–140.

[37] Vetushka, A.; Bernard, L.; Guseva, O.; Bastl, Z.; Plocek, J.; Tomandl, I.; Fejfar, A.; Baše, T.; Schmutz, P. Adsorption of oriented carborane dipoles on a silver surface. *Phys. Status Solidi B* **2016**, *253*, 591–600.

[38] Thomas, J. C.; Goronzy, D. P.; Serino, A. C.; Auluck, H. S.; Irving, O. R.; Jimenez-Izal, E.; Deirmenjian, J. M.; Macháček, J.; Sautet, P.; Alexandrova, A. N.; Baše, T.; Weiss, P. S. Acid–Base Control of Valency within Carboranedithiol Self-Assembled Monolayers: Molecules Do the Can-Can. *ACS Nano* **2018**, *12*, 2211–2221.

[39] Soler, J. M.; Artacho, E.; Gale, J. D.; García, A.; Junquera, J.; Ordejón, P.; Sánchez-Portal, D. The SIESTA method for ab initio order-N materials simulation. *J. Phys.: Condens. Matter* **2002**, *14*, 2745–2779.

[40] Artacho, E.; Anglada, E.; Diéguez, O.; Gale, J. D.; García, A.; Junquera, J.; Martin, R. M.; Ordejón, P.; Pruneda, J. M.; Sánchez-Portal, D.; Soler, J. M. The SIESTA method; developments and applicability. *J. Phys.: Condens. Matter* **2008**, *20*, 064208.

[41] Fujii, S.; Akiba, U.; Fujihira, M. Geometry for Self-Assembling of Spherical Hydrocarbon Cages with Methane Thiolates on Au(111). *J. Am. Chem. Soc.* **2002**, *124*, 13629–13635.

[42] Dameron, A. A.; Charles, L. F.; Weiss, P. S. Structures and Displacement of 1-Adamantanethiol Self-Assembled Monolayers on Au{111}. *J. Am. Chem. Soc.* **2005**, *127*, 8697–8704.

[43] Weiss, P. S. Functional Molecules and Assemblies in Controlled Environments: Formation and Measurements. *Acc. Chem. Res.* **2008**, *41*, 1772–1781.

[44] Willey, T. M.; Fabbri, J. D.; Lee, J. R. I.; Schreiner, P. R.; Fokin, A. A.; Tkachenko, B. A.; Fokina, N. A.; Dahl, J. E. P.; Carlson, R. M. K.; Vance, A. L.;

Yang, W.; Terminello, L. J.; Buuren, T. v.; Melosh, N. A. Near-Edge X-ray Absorption Fine Structure Spectroscopy of Diamondoid Thiol Monolayers on Gold. *J. Am. Chem. Soc.* **2008**, *130*, 10536–10544.

[45] Hohman, J. N.; Zhang, P.; Morin, E. I.; Han, P.; Kim, M.; Kurland, A. R.; McClanahan, P. D.; Balema, V. P.; Weiss, P. S. Self-Assembly of Carboranethiol Isomers on Au{111}: Intermolecular Interactions Determined by Molecular Dipole Orientations. *ACS Nano* **2009**, *3*, 527–536.

[46] Vericat, C.; Vela, M. E.; Benitez, G.; Carro, P.; Salvarezza, R. C. Self-assembled monolayers of thiols and dithiols on gold: new challenges for a well-known system. *Chem. Soc. Rev.* **2010**, *39*, 1805–1834.

[47] Häkkinen, H. The gold–sulfur interface at the nanoscale. *Nat. Chem.* **2012**, *4*, 443–455.

[48] Kim, J.; Rim, Y. S.; Liu, Y.; Serino, A. C.; Thomas, J. C.; Chen, H.; Yang, Y.; Weiss, P. S. Interface Control in Organic Electronics Using Mixed Monolayers of Carboranethiol Isomers. *Nano Lett.* **2014**, *14*, 2946–2951.

[49] Hladík, M.; Vetushka, A.; Fejfar, A.; Vázquez, H. Tuning of the gold work function by carborane films studied using density functional theory. *Phys. Chem. Chem. Phys.* **2019**, *21*, 6178–6185.

[50] Coulter, S. K.; Schwartz, M. P.; Hamers, R. J. Sulfur Atoms as Tethers for Selective Attachment of Aromatic Molecules to Silicon(001) Surfaces. *J. Phys. Chem. B* **2001**, *105*, 3079–3087.

[51] Hladík, M.; Fejfar, A.; Vázquez, H. Doping of the hydrogen-passivated Si(100) electronic structure through carborane adsorption studied using density functional theory. *Phys. Chem. Chem. Phys.* **2021**, *23*, 20379–20387.

[52] Kümmel, S.; Kronik, L. Orbital-dependent density functionals: Theory and applications. *Rev. Mod. Phys.* **2008**, *80*, 3–60.

[53] Parr, R. G.; Yang, W. *Density-functional theory of atoms and molecules*; International series of monographs on chemistry 16; Oxford University Press, Inc.: New York, NY, 1989.

[54] Koch, W.; Holthausen, M. C. *A Chemist's Guide to Density Functional Theory*, 2nd ed.; Wiley-VCH Verlag GmbH: Weinheim; New York, 2001.

[55] Hohenberg, P.; Kohn, W. Inhomogeneous Electron Gas. *Phys. Rev.* **1964**, *136*, B864–B871.

[56] Vosko, S. H.; Wilk, L.; Nusair, M. Accurate spin-dependent electron liquid correlation energies for local spin density calculations: a critical analysis. *Can. J. Phys.* **1980**, *58*, 1200–1211.

[57] Ceperley, D. M.; Alder, B. J. Ground State of the Electron Gas by a Stochastic Method. *Phys. Rev. Lett.* **1980**, *45*, 566–569.

[58] Perdew, J. P.; Wang, Y. Accurate and simple density functional for the electronic exchange energy: Generalized gradient approximation. *Phys. Rev. B* **1986**, *33*, 8800–8802.

[59] Perdew, J. P.; Burke, K.; Ernzerhof, M. Generalized Gradient Approximation Made Simple. *Phys. Rev. Lett.* **1996**, *77*, 3865–3868.

[60] Zhang, Y.; Yang, W. Comment on "Generalized Gradient Approximation Made Simple". *Phys. Rev. Lett.* **1998**, *80*, 890–890.

[61] Berland, K.; Cooper, V. R.; Lee, K.; Schröder, E.; Thonhauser, T.; Hyldgaard, P.; Lundqvist, B. I. van der Waals forces in density functional theory: a review of the vdW-DF method. *Rep. Prog. Phys.* **2015**, *78*, 066501.

[62] Hyldgaard, P.; Jiao, Y.; Shukla, V. Screening nature of the van der Waals density functional method: a review and analysis of the many-body physics foundation. *J. Phys.: Condens. Matter* **2020**, *32*, 393001.

[63] Rydberg, H.; Dion, M.; Jacobson, N.; Schröder, E.; Hyldgaard, P.; Simak, S. I.; Langreth, D. C.; Lundqvist, B. I. Van der Waals Density Functional for Layered Structures. *Phys. Rev. Lett.* **2003**, *91*, 126402.

[64] Dion, M.; Rydberg, H.; Schröder, E.; Langreth, D. C.; Lundqvist, B. I. Van der Waals Density Functional for General Geometries. *Phys. Rev. Lett.* **2004**, *92*, 246401.

[65] Bhattarai, P.; Patra, A.; Shahi, C.; Perdew, J. P. How accurate are the parametrized correlation energies of the uniform electron gas? *Phys. Rev. B* **2018**, *97*, 195128.

[66] Kohn, W.; Sham, L. J. Self-Consistent Equations Including Exchange and Correlation Effects. *Phys. Rev.* **1965**, *140*, A1133–A1138.

[67] Perdew, J. P. Accurate Density Functional for the Energy: Real-Space Cutoff of the Gradient Expansion for the Exchange Hole. *Phys. Rev. Lett.* **1985**, *55*, 1665–1668.

[68] Hermann, J. Towards unified density-functional model of van der Waals interactions. Ph.D. Thesis, Humboldt-Universität zu Berlin, Berlin, 2018.

[69] Kleinman, L.; Bylander, D. M. Efficacious Form for Model Pseudopotentials. *Phys. Rev. Lett.* **1982**, *48*, 1425–1428.

[70] Mazzarello, R.; Cossaro, A.; Verdini, A.; Rousseau, R.; Casalis, L.; Danisman, M. F.; Floreano, L.; Scandolo, S.; Morgante, A.; Scoles, G. Structure of a CH_3S Monolayer on Au(111) Solved by the Interplay between Molecular Dynamics Calculations and Diffraction Measurements. *Phys. Rev. Lett.* **2007**, *98*, 016102.

[71] Krüger, D.; Fuchs, H.; Rousseau, R.; Marx, D.; Parrinello, M. Pulling Monatomic Gold Wires with Single Molecules: An Ab Initio Simulation. *Phys. Rev. Lett.* **2002**, *89*, 186402.

[72] Xue, Y.; Li, X.; Li, H.; Zhang, W. Quantifying thiol–gold interactions towards the efficient strength control. *Nat. Commun.* **2014**, *5*, 4348.

[73] Suh, I.-K.; Ohta, H.; Waseda, Y. High-temperature thermal expansion of six metallic elements measured by dilatation method and X-ray diffraction. *J. Mater. Sci.* **1988**, *23*, 757–760.

[74] Haas, P.; Tran, F.; Blaha, P. Calculation of the lattice constant of solids with semilocal functionals. *Phys. Rev. B* **2009**, *79*, 085104.

[75] Chen, W.-J.; Yeh, C.-H.; Chang, C.-C.; Ho, J.-J. Energetics of C–N coupling reactions on Pt(111) and Ni(111) surfaces from application of density-functional theory. *Phys. Chem. Chem. Phys.* **2013**, *15*, 10395–10401.

[76] Bernard Rodríguez, C. R.; Santana, J. A. Adsorption and diffusion of sulfur on the (111), (100), (110), and (211) surfaces of FCC metals: Density functional theory calculations. *J. Chem. Phys.* **2018**, *149*, 204701.

[77] Grönbeck, H.; Curioni, A.; Andreoni, W. Thiols and Disulfides on the Au(111) Surface: The Headgroup-Gold Interaction. *J. Am. Chem. Soc.* **2000**, *122*, 3839–3842.

[78] Daigle, A. D.; BelBruno, J. J. Density Functional Theory Study of the Adsorption of Nitrogen and Sulfur Atoms on Gold (111), (100), and (211) Surfaces. *J. Phys. Chem. C* **2011**, *115*, 22987–22997.

[79] Cometto, F. P.; Paredes-Olivera, P.; Macagno, V. A.; Patrito, E. M. Density Functional Theory Study of the Adsorption of Alkanethiols on Cu(111), Ag(111), and Au(111) in the Low and High Coverage Regimes. *J. Phys. Chem. B* **2005**, *109*, 21737–21748.

[80] Mete, E.; Yılmaz, A.; Danışman, M. F. A van der Waals density functional investigation of carboranethiol self-assembled monolayers on Au(111). *Phys. Chem. Chem. Phys.* **2016**, *18*, 12920–12927.

[81] Min, B. K.; Alemozafar, A. R.; Biener, M. M.; Biener, J.; Friend, C. M. Reaction of Au(111) with Sulfur and Oxygen: Scanning Tunneling Microscopic Study. *Top. Catal.* **2005**, *36*, 77–90.

[82] Hanke, F.; Björk, J. Structure and local reactivity of the Au(111) surface reconstruction. *Phys. Rev. B* **2013**, *87*, 235422.

[83] Dubois, L. H.; Nuzzo, R. G. Synthesis, Structure, and Properties of Model Organic Surfaces. *Annu. Rev. Phys. Chem.* **1992**, *43*, 437–463.

[84] Ulman, A. Formation and Structure of Self-Assembled Monolayers. *Chem. Rev.* **1996**, *96*, 1533–1554.

[85] Schreiber, F. Structure and growth of self-assembling monolayers. *Prog. Surf. Sci.* **2000**, *65*, 151–257.

[86] Becker, P.; Scyfried, P.; Siegert, H. The lattice parameter of highly pure silicon single crystals. *Z. Phys. B - Condensed Matter* **1982**, *48*, 17–21.

[87] Rivero, P.; García-Suárez, V. M.; Pereñiguez, D.; Utt, K.; Yang, Y.; Bellaiche, L.; Park, K.; Ferrer, J.; Barraza-Lopez, S. Systematic pseudopotentials from reference eigenvalue sets for DFT calculations. *Comput. Mater. Sci.* **2015**, *98*, 372–389.

[88] Körzdörfer, T. On the relation between orbital-localization and self-interaction errors in the density functional theory treatment of organic semiconductors. *J. Chem. Phys.* **2011**, *134*, 094111.

[89] Duke, C. B. Semiconductor Surface Reconstruction: The Structural Chemistry of Two-Dimensional Surface Compounds. *Chem. Rev.* **1996**, *96*, 1237–1260.

[90] Waltenburg, H. N.; Yates, J. T. Surface Chemistry of Silicon. *Chem. Rev.* **1995**, *95*, 1589–1673.

[91] Perrine, K. A.; Teplyakov, A. V. Reactivity of selectively terminated single crystal silicon surfaces. *Chem. Soc. Rev.* **2010**, *39*, 3256–3274.

[92] Yoshinobu, J. Physical properties and chemical reactivity of the buckled dimer on Si(100). *Prog. Surf. Sci.* **2004**, *77*, 37–70.

[93] Chadi, D. J. Atomic and Electronic Structures of Reconstructed Si(100) Surfaces. *Phys. Rev. Lett.* **1979**, *43*, 43–47.

[94] Buriak, J. M. Organometallic Chemistry on Silicon and Germanium Surfaces. *Chem. Rev.* **2002**, *102*, 1271–1308.

[95] Akremi, A.; Lacharme, J. P.; Sébenne, C. A. Residual gap surface states along variously hydrogenated silicon (111) and (100) surfaces. *Surf. Sci.* **1997**, *377-379*, 192–196.

[96] Chabal, Y. J.; Higashi, G. S.; Raghavachari, K.; Burrows, V. A. Infrared spectroscopy of Si(111) and Si(100) surfaces after HF treatment: Hydrogen termination and surface morphology. *J. Vac. Sci. Technol. A* **1989**, *7*, 2104–2109.

[97] Shirahata, N.; Hozumi, A.; Yonezawa, T. Monolayer-derivative functionalization of non-oxidized silicon surfaces. *Chem. Rec.* **2005**, *5*, 145–159.

[98] Miyata, N.; Watanabe, S.; Okamura, S. Infrared and Raman study of H-terminated Si(100) surfaces produced by etching solutions. *Appl. Surf. Sci.* **1997**, *117-118*, 26–31.

[99] Northrup, J. E. Structure of Si(100)H: Dependence on the H chemical potential. *Phys. Rev. B* **1991**, *44*, 1419–1422.

[100] Beall, H. In *Boron Hydride Chemistry*; Muetterties, E. L., Ed.; Academic Press: New York, N.Y., 1975; pp 301–347.

[101] Grimes, R. N. In *Carboranes (Second Edition)*; Grimes, R. N., Ed.; Academic Press: Oxford, 2011; pp 301–540.

[102] Laubengayer, A. W.; Rysz, W. R. The Dipole Moments of the Isomers of Dicarbadecaborane, $B_{10}H_{10}C_2H_2$. *Inorg. Chem.* **1965**, *4*, 1513–1514.

[103] Bregadze, V. I. Dicarba-closo-dodecaboranes $C_2B_{10}H_{12}$ and their derivatives. *Chem. Rev.* **1992**, *92*, 209–223.

[104] Wade, K. In *Advances in Inorganic Chemistry and Radiochemistry*; Emeléus, H. J., Sharpe, A. G., Eds.; Academic Press: New York, N.Y., 1976; Vol. 18; pp 1–66.

[105] King, R. B. Three-Dimensional Aromaticity in Polyhedral Boranes and Related Molecules. *Chem. Rev.* **2001**, *101*, 1119–1152.

[106] Schwartz, J. J.; Mendoza, A. M.; Wattanatorn, N.; Zhao, Y.; Nguyen, V. T.; Spokoyny, A. M.; Mirkin, C. A.; Baše, T.; Weiss, P. S. Surface Dipole Control of Liquid Crystal Alignment. *J. Am. Chem. Soc.* **2016**, *138*, 5957–5967.

[107] Natan, A.; Kronik, L.; Shapira, Y. Computing surface dipoles and potentials of self-assembled monolayers from first principles. *Appl. Surf. Sci.* **2006**, *252*, 7608–7613.

[108] Hofmann, O. T.; Zojer, E.; Hörmann, L.; Jeindl, A.; Maurer, R. J. First-principles calculations of hybrid inorganic–organic interfaces: from state-of-the-art to best practice. *Phys. Chem. Chem. Phys.* **2021**, *23*, 8132–8180.

[109] Román-Pérez, G.; Soler, J. M. Efficient Implementation of a van der Waals Density Functional: Application to Double-Wall Carbon Nanotubes. *Phys. Rev. Lett.* **2009**, *103*, 096102.

[110] Shuttleworth, I. G. Development of the ReaxFF Reactive Force-Field Description of Gold Oxides. *J. Phys. Chem. C* **2017**, *121*, 25255–25270.

[111] Chen, J.; Gathiaka, S.; Wang, Z.; Thuo, M. Role of Molecular Dipoles in Charge Transport across Large Area Molecular Junctions Delineated Using Isomorphic Self-Assembled Monolayers. *J. Phys. Chem. C* **2017**, *121*, 23931–23938.

[112] Heimel, G.; Romaner, L.; Zojer, E.; Brédas, J.-L. Toward Control of the Metal-Organic Interfacial Electronic Structure in Molecular Electronics: A First-Principles Study on Self-Assembled Monolayers of Pi-Conjugated Molecules on Noble Metals. *Nano Lett.* **2007**, *7*, 932–940.

[113] Obersteiner, V.; Egger, D. A.; Zojer, E. Impact of Anchoring Groups on Ballistic Transport: Single Molecule vs Monolayer Junctions. *J. Phys. Chem. C* **2015**, *119*, 21198–21208.

[114] Foti, G.; Vázquez, H. Tip-induced gating of molecular levels in carbene-based junctions. *Nanotechnology* **2016**, *27*, 125702.

[115] Junquera, J.; Zimmer, M.; Ordejón, P.; Ghosez, P. First-principles calculation of the band offset at $BaO/BaTiO_3$ and $SrO/SrTiO_3$ interfaces. *Phys. Rev. B* **2003**, *67*, 155327.

[116] Djurabekova, F.; Ruzibaev, A.; Holmström, E.; Parviainen, S.; Hakala, M. Local changes of work function near rough features on Cu surfaces operated under high external electric field. *J. Appl. Phys.* **2013**, *114*, 243302.

[117] Junquera, J.; Cohen, M. H.; Rabe, K. M. Nanoscale smoothing and the analysis of interfacial charge and dipolar densities. *J. Phys.: Condens. Matter* **2007**, *19*, 213203.

[118] Peiris, C. R.; Ciampi, S.; Dief, E. M.; Zhang, J.; Canfield, P. J.; Brun, A. P. L.; Kosov, D. S.; Reimers, J. R.; Darwish, N. Spontaneous S–Si bonding of alkanethiols to Si(111)–H: towards Si–molecule–Si circuits. *Chem. Sci.* **2020**, *11*, 5246–5256.

[119] Huang, Y.-S.; Chen, C.-H.; Chen, C.-H.; Hung, W.-H. Fabrication of Octadecyl and Octadecanethiolate Self-Assembled Monolayers on Oxide-Free Si(111) with a One-Cell Process. *ACS Appl. Mater. Interfaces* **2013**, *5*, 5771–5776.

[120] Huheey, J. E.; Keiter, E. A.; Keiter, R. L. *Inorganic chemistry: principles of structure and reactivity*, 4th ed.; HarperCollins College Publishers: New York, NY, 1993; OCLC: 26974220.

[121] Serino, A. C.; Anderson, M. E.; Saleh, L. M. A.; Dziedzic, R. M.; Mills, H.; Heidenreich, L. K.; Spokoyny, A. M.; Weiss, P. S. Work Function Control of Germanium through Carborane-Carboxylic Acid Surface Passivation. *ACS Appl. Mater. Interfaces* **2017**, *9*, 34592–34596.

[122] Abel, E. W.; Armitage, D. A. In *Advances in Organometallic Chemistry*; Stone, F. G. A., West, R., Eds.; Academic Press, 1967; Vol. 5; pp 1–92.

[123] Borisov, S. N.; Voronkov, M. G.; Lukevits, E. Y. In *Organosilicon Derivatives of Phosphorus and Sulfur*; Borisov, S. N., Voronkov, M. G., Lukevits, E. Y., Eds.; Monographs in Inorganic Chemistry; Springer: Boston, MA, 1971; pp 157–333.

[124] Grandbois, M.; Beyer, M.; Rief, M.; Clausen-Schaumann, H.; Gaub, H. E. How Strong Is a Covalent Bond? *Science* **1999**, *283*, 1727–1730.

[125] Pérez, R.; Štich, I.; Payne, M. C.; Terakura, K. Surface-tip interactions in noncontact atomic-force microscopy on reactive surfaces: Si(111). *Phys. Rev. B* **1998**, *58*, 10835–10849.

[126] Schmidt, S. W.; Beyer, M. K.; Clausen-Schaumann, H. Dynamic Strength of the Silicon-Carbon Bond Observed over Three Decades of Force-Loading Rates. *J. Am. Chem. Soc.* **2008**, *130*, 3664–3668.

[127] Garnier, L.; Gauthier-Manuel, B.; van der Vegte, E. W.; Snijders, J.; Hadziioannou, G. Covalent bond force profile and cleavage in a single polymer chain. *J. Chem. Phys.* **2000**, *113*, 2497–2503.

[128] Hanson, D. E.; Barber, J. L. The bond rupture force for sulfur chains calculated from quantum chemistry simulations and its relevance to the tensile strength of vulcanized rubber. *Phys. Chem. Chem. Phys.* **2018**, *20*, 8460–8465.

[129] Lantz, M. A.; Hug, H. J.; Hoffmann, R.; van Schendel, P. J. A.; Kappenberger, P.; Martin, S.; Baratoff, A.; Güntherodt, H.-J. Quantitative Measurement of Short-Range Chemical Bonding Forces. *Science* **2001**, *291*, 2580–2583.

[130] Callen, H. B.; Welton, T. A. Irreversibility and Generalized Noise. *Phys. Rev.* **1951**, *83*, 34–40.

[131] Berland, K.; Hyldgaard, P. Exchange functional that tests the robustness of the plasmon description of the van der Waals density functional. *Phys. Rev. B* **2014**, *89*, 035412.

[132] Kannemann, F. O.; Becke, A. D. van der Waals Interactions in Density-Functional Theory: Intermolecular Complexes. *J. Chem. Theory Comput.* **2010**, *6*, 1081–1088.

[133] Langreth, D. C. et al. A density functional for sparse matter. *J. Phys.: Condens. Matter* **2009**, *21*, 084203.

[134] Kelkkanen, A. K.; Lundqvist, B. I.; Nørskov, J. K. Density functional for van der Waals forces accounts for hydrogen bond in benchmark set of water hexamers. *J. Chem. Phys.* **2009**, *131*, 046102.

[135] Lee, K.; Kelkkanen, A. K.; Berland, K.; Andersson, S.; Langreth, D. C.; Schröder, E.; Lundqvist, B. I.; Hyldgaard, P. Evaluation of a density functional with account of van der Waals forces using experimental data of H_2 physisorption on Cu(111). *Phys. Rev. B* **2011**, *84*, 193408.

[136] Sun, D.; Kim, D.-H.; Le, D.; Borck, Ø.; Berland, K.; Kim, K.; Lu, W.; Zhu, Y.; Luo, M.; Wyrick, J.; Cheng, Z.; Einstein, T. L.; Rahman, T. S.; Hyldgaard, P.; Bartels, L. Effective elastic properties of a van der Waals molecular monolayer at a metal surface. *Phys. Rev. B* **2010**, *82*, 201410.

[137] Yanagisawa, S.; Hamada, I.; Lee, K.; Langreth, D. C.; Morikawa, Y. Adsorption of Alq_3 on Mg(001) surface: Role of chemical bonding, molecular distortion, and van der Waals interaction. *Phys. Rev. B* **2011**, *83*, 235412.

[138] Johnston, K.; Kleis, J.; Lundqvist, B. I.; Nieminen, R. M. Influence of van der Waals forces on the adsorption structure of benzene on silicon studied using density functional theory. *Phys. Rev. B* **2008**, *77*, 121404.

[139] Li, G.; Cooper, V. R.; Cho, J.-H.; Du, S.; Gao, H.-J.; Zhang, Z. Self-assembly of molecular wires on H-terminated Si(100) surfaces driven by London dispersion forces. *Phys. Rev. B* **2011**, *84*, 241406.

List of Figures

List of Tables

List of Symbols

Abbreviations

Symbol	Description
A_{opt}	the most stable B-bonded chemisorbed silicon-molecule junction
AD_{min}	the most stable B-bonded gold-molecule junction with Au adatom
B_{min}	the most stable B-bonded gold-molecule junction
B_{opt}	the most stable B-bonded physisorbed silicon-molecule junction
C_{min}	the most stable C-bonded gold-molecule junction
C_{opt}	the most stable C-bonded chemisorbed silicon-molecule junction
c-Si	crystalline silicon
DFT	density functional theory
DZP	double-ζ plus polarisation
FFC	face-centred cubic
GGA	generalised-gradient approximation
HOMO	highest occupied molecular orbital
KB	Kleinman-Bylander
KS	Kohn-Sham
LUMO	lowest unoccupied molecular orbital
MLD	monolayer doping
mono-Si	monocrystalline silicon
multi-Si	multicrystalline silicon
PBC(s)	periodic boundary condition(s)
PBE	Perdew–Burke–Ernzerhof
PDOS	projected density of states
PERx	passivated emitter and rear side
PV	photovoltaic (*adj.*), photovoltaics (*n.*)
SAM(s)	self-assembled monolayer(s)
SZP	single-ζ plus polarisation
SiO_2	silicon dioxide
STD	surface transfer doping
TR_{min}	the most stable B-bonded gold-molecule junction with Au trimer
vdW	van der Waals
vdW-DF	van der Waals density functional
WEC	world energy consumption
Wp	Watt-peak, i.e. the unit of nominal power of the solar panel under standard test conditions for AM 1.5 illumination

Constants

Symbol	Description
a_{Au}	lattice constant of gold (optimised in this thesis) [$= 4.200$ $\mathring{A}$]
a_{Si}	lattice constant of silicon (optimised in this thesis) [$= 5.497(372)$ $\mathring{A}$]
e	elementary charge [$\approx 1.602 \times 10^{-19}$ C]
ϵ_0	vacuum permittivity [$\approx 8.854 \times 10^{-12}$ $C \cdot V^{-1} \cdot m^{-1}$]
Ω_{Au}	unit-cell area of the Au(111) wafer [≈ 122.213 $\mathring{A}^2$]
Ω_{Si}	unit-cell area of the H_2-terminated Si(100) wafer [≈ 241.769 $\mathring{A}^2$]

Selected quantities

Symbol	Description
$\alpha_{\text{H-H}}$	H-Si-H bond angle [°]
$\mathbf{c_1}$, $\mathbf{c_2}$, $\mathbf{c_3}$	primitive translation vectors of the FCC lattice [$\mathring{A}$]
$d_{\text{Au-Au}}$	Au-Au bond length [$\mathring{A}$]
$d_{\text{H-H}}$	hydrogen-hydrogen spacing between adjacent SiH_2 groups [$\mathring{A}$]
$d_{\text{Si-S}}$	Si-S bond length/shortest Si-S distance [$\mathring{A}$]
$d_{\text{Si-H}}$	Si-H bond length [$\mathring{A}$]
$d_{\text{Si-Si}}$	Si-Si bond length [$\mathring{A}$]
$\Delta\mu$	electric dipole moment change [D]
$\Delta\mu_{\text{Au,surf}}$	$\Delta\mu$ of the Au surface [D], ($= \mu_{\text{Au-Mol}} - \mu_{\text{Au}}$)
$\Delta\mu_{\text{Si,surf}}$	$\Delta\mu$ of the Si surface [D], ($= \mu_{\text{Si-Mol}} - \mu_{\text{Si}}$)
$\Delta\mu_{\text{surf}}$	$\Delta\mu$ of the surface [D]
$\Delta\Phi$	work function change [eV]
$\Delta\Phi_{\text{Au}}$	$\Delta\Phi$ of the Au substrate [eV], ($= \Phi_{\text{Au-Mol}} - \Phi_{\text{Au}}$)
$\Delta\Phi_{\text{Si}}$	$\Delta\Phi$ of the Si substrate [eV], ($= \Phi_{\text{Si-Mol}} - \Phi_{\text{Si}}$)
ΔU_{BB}	band bending [eV]
ΔU_{e}	barrier height for electron injection [eV], ($= E_{\text{LUMO}} - E_{\text{F}}$)
ΔU_{h}	barrier height for hole injection [eV], ($= E_{\text{F}} - E_{\text{HOMO}}$)
$\Delta U_{\text{Au,surf}}$	Au-surface potential-energy step [eV], ($= \Delta\Phi_{\text{Au}}$)
$\Delta U_{\text{Si,surf}}$	Si-surface potential-energy step [eV]
ΔU_{surf}	surface potential-energy step [eV]
$\delta V_{\text{H}}(z)$	plane-averaged distorted potential energy [eV], ($= V_{\text{El}}(z) - V_{\text{NA}}(z)$)
$\langle \delta V_{\text{H}} \rangle_{\text{slab}}$	nano-smoothed $\delta V_{\text{H}}(z)$ in the middle of the slab [eV]
$\langle \delta V_{\text{H}} \rangle_{\text{vac}}$	nano-smoothed $\delta V_{\text{H}}(z)$ in the vacuum above the surface [eV]
$\Delta\langle \delta V_{\text{H}} \rangle$	the line-up term [eV], ($= \langle \delta V_{\text{H}} \rangle_{\text{vac}} - \langle \delta V_{\text{H}} \rangle_{\text{slab}}$)
$E_{\text{Au-Mol}}$	E_{tot} of the Au-molecule junction [eV], ($E_{\text{Au-Mol}} < 0$)
E_{B}	binding energy [eV]
$E_{\text{B\{jcn\}}}$	binding energy in the junction basis set [eV]
E_{CB}	conduction-band edge (minimum) [eV]
E_{F}	Fermi level [eV]
E_{g}	band-gap energy [eV], ($= E_{\text{CB}} - E_{\text{VB}}$)
E_{Γ}	band-gap energy at Γ point [eV]

Symbol	Description
E_{HOMO}	energy of HOMO $[eV]$
$E_{\mathrm{H,rad}}$	E_{tot} of the hydrogen radical $[eV]$
E_{LUMO}	energy of LUMO $[eV]$
E_{Mol}	E_{tot} of the unsaturated carboranedithiol $[eV]$, $(E_{\mathrm{mol}} < 0)$
$E_{\mathrm{Mol+H}}$	E_{tot} of the mono-saturated carboranedithiol $[eV]$, $(E_{\mathrm{Mol+H}} < 0)$
$E_{\mathrm{Mol+2H}}$	E_{tot} of the fully saturated carboranedithiol $[eV]$, $(E_{\mathrm{Mol+2H}} < 0)$
E_{rec}	energy released in reconstructing the Si surface $[eV]$, $(E_{\mathrm{rec}} < 0)$
$E_{\mathrm{S\text{-}H}}$	energy released in forming the S-H bond(s) $[eV]$, $(E_{\mathrm{S\text{-}H}} < 0)$
E_{Si}	E_{tot} of the bare (H_2-terminated) Si substrate $[eV]$, $(E_{\mathrm{Si}} < 0)$
$E_{\mathrm{Si\text{-}Mol}}$	E_{tot} of the Si-molecule junction $[eV]$, $(E_{\mathrm{Si\text{-}Mol}} < 0)$
$E_{\mathrm{Si,rad}}$	E_{tot} of the Si substrate with one dangling bond $[eV]$, $(E_{\mathrm{Si,rad}} < 0)$
$E_{\mathrm{Si,2rad}}$	E_{tot} of the Si substrate with two dangling bonds $[eV]$, $(E_{\mathrm{Si,2rad}} < 0)$
$E_{\mathrm{Si\text{-}S}}$	energy released in forming the Si-S bond $[eV]$, $(E_{\mathrm{Si\text{-}S}} < 0)$
$E_{\mathrm{Si\text{-}H}}$	energy absorbed in breaking the Si-H bond(s) $[eV]$, $(E_{\mathrm{Si\text{-}H}} > 0)$
E_{tot}	total energy $[eV]$, $(E_{\mathrm{tot}} < 0)$
E_{vac}	vacuum level $[eV]$, $(= \Delta\langle\delta V_{\mathrm{H}}\rangle$ - $\langle V_{\mathrm{El}}\rangle_{\mathrm{bulk}})$
E_{VB}	valence-band edge (maximum) $[eV]$
$\mathbf{h_1}$, $\mathbf{h_2}$, $\mathbf{h_3}$	primitive translation vectors of the hexagonal lattice $[\AA]$
$\mathbf{k}$	k-vector in the reciprocal space scaled by π/a_{Si} $[\AA^{-1}]$
$\mathbf{k}_{\parallel}$	in-plane k-vector in the reciprocal space scaled by π/a_{Si} $[\AA^{-1}]$
μ	electric dipole moment $[D]$
μ_{Au}	μ of the bare Au substrate $[D]$, $(\mu_{\mathrm{Au}} \parallel z\text{-axis})$
$\mu_{\mathrm{Au\{jcn\}}}$	μ_{Au} in the junction basis set $[D]$, $(\mu_{\mathrm{Au\{jcn\}}} \parallel z\text{-axis})$
$\mu_{\mathrm{Au\text{-}Mol}}$	μ of the Au-molecule junction $[D]$, $(= \mu_{\mathrm{Au\{jcn\}}} + \mu_{\mathrm{Mol\{jcn\}}} + \mu_{\mathrm{Au\text{-}S}})$
$\mu_{\mathrm{Au\text{-}S}}$	μ of the Au-molecule interface $[D]$, $(\mu_{\mathrm{Au\text{-}S}} \parallel z\text{-axis})$
μ_{int}	μ of the substrate-adsorbate interface $[D]$, $(\mu_{\mathrm{int}} \parallel z\text{-axis})$
μ_{Mol}	μ of the molecule/molecular adsorbate $[D]$, $(\mu_{\mathrm{Mol}} \parallel z\text{-axis})$
$\mu_{\mathrm{Mol\{jcn\}}}$	μ_{Mol} in the junction basis set $[D]$, $(\mu_{\mathrm{Mol\{jcn\}}} \parallel z\text{-axis})$
μ_{Si}	μ of the bare (H_2-terminated) Si substrate $[D]$, $(\mu_{\mathrm{Si}} \parallel z\text{-axis})$
$\mu_{\mathrm{Si\{jcn\}}}$	μ_{Si} in the junction basis set $[D]$, $(\mu_{\mathrm{Si\{jcn\}}} \parallel z\text{-axis})$
$\mu_{\mathrm{Si\text{-}Mol}}$	μ of the Si-molecule junction $[D]$, $(= \mu_{\mathrm{Si\{jcn\}}} + \mu_{\mathrm{Mol\{jcn\}}} + \mu_{\mathrm{Si\text{-}S}})$
$\mu_{\mathrm{Si\text{-}S}}$	μ of the Si-molecule interface $[D]$, $(\mu_{\mathrm{Si\text{-}S}} \parallel z\text{-axis})$
μ_{unit}	μ of the unit cell $[D]$, $(\mu_{\mathrm{unit}} \parallel z\text{-axis})$
μ_{z}, $\mu_{\perp}$	projection of μ along the z-axis/surface normal $[D]$
ν(Si–H)	infrared stretching-vibration frequency of Si-H bonds $[cm^{-1}]$
Ω	surface area taken by one adsorbed molecule $[\AA^2]$
Φ	work function $[eV]$, $(= E_{\mathrm{vac}} - E_{\mathrm{F}})$
Φ_{Au}	work function of the bare Au substrate $[eV]$
$\Phi_{\mathrm{Au\text{-}Mol}}$	work function of the Au-molecule junction $[eV]$
Φ_{Si}	work function of the bare (H_2-terminated) Si substrate $[eV]$
$\Phi_{\mathrm{Si\text{-}Mol}}$	work function of the Si-molecule junction $[eV]$
φ_{Mol}	azimuthal angle of the molecule [°]
$\rho(z)$	plane-averaged charge density $[\lvert e\rvert\cdot\AA^{-1}]$, $(= \rho_{\mathrm{el}}(z) - \rho_{\mathrm{ion}}(z))$

Symbol	Description
$\rho_{\text{Au\{jcn\}}}(z)$	$\rho(z)$ of the bare Au substrate in the junction basis set $[\lvert e\rvert \cdot \mathring{A}^{-1}]$
$\rho_{\text{Au-Mol}}(z)$	$\rho(z)$ of the Au-molecule junction $[\lvert e\rvert \cdot \mathring{A}^{-1}]$
$\rho_{\text{diff}}(z)$	plane-averaged charge density difference $[\lvert e\rvert \cdot \mathring{A}^{-1}]$
$\rho_{\text{el}}(z)$	plane-averaged electron charge density $[\lvert e\rvert \cdot \mathring{A}^{-1}]$
$\rho_{\text{ion}}(z)$	plane-averaged ionic charge density $[\lvert e\rvert \cdot \mathring{A}^{-1}]$
$\rho_{\text{Mol\{jcn\}}}(z)$	$\rho(z)$ of the isolated molecule in the junction basis set $[\lvert e\rvert \cdot \mathring{A}^{-1}]$
$\rho_{\text{Si\{jcn\}}}(z)$	$\rho(z)$ of the bare Si substrate in the junction basis set $[\lvert e\rvert \cdot \mathring{A}^{-1}]$
$\rho_{\text{Si-Mol}}(z)$	$\rho(z)$ of the Si-molecule junction $[\lvert e\rvert \cdot \mathring{A}^{-1}]$
T	temperature $[K]$
$\mathbf{t_1}$, $\mathbf{t_2}$, $\mathbf{t_3}$	primitive translation vectors of the tetragonal lattice $[\mathring{A}]$
$\theta_{\text{H-H}}$	canted angle of terminal dihydride groups [°]
θ_{Mol}	tilt (polar) angle of the molecule [°]
$\theta_{\text{Si-Si}}$	canted angle of outermost Si-Si bonds [°]
$V_{\text{El}}(z)$	plane-averaged electrostatic potential energy $[eV]$
$\langle V_{\text{El}} \rangle_{\text{bulk}}$	nano-smoothed $V_{\text{El}}(z)$ of the bulk $[eV]$
$\langle V_{\text{El}} \rangle_{\text{slab}}$	nano-smoothed $V_{\text{El}}(z)$ in the middle of the slab $[eV]$
$\langle V_{\text{El}} \rangle_{\text{vac}}$	nano-smoothed $V_{\text{El}}(z)$ in the vacuum above the surface $[eV]$
$V_{\text{NA}}(z)$	plane-averaged neutral-atom potential energy $[eV]$
$\langle V_{\text{NA}} \rangle_{\text{slab}}$	nano-smoothed $V_{\text{NA}}(z)$ in the middle of the slab $[eV]$
$\langle V_{\text{NA}} \rangle_{\text{vac}}$	nano-smoothed $V_{\text{NA}}(z)$ in the vacuum above the surface $[eV]$
$\hat{\mathbf{x}}$, $\hat{\mathbf{y}}$, $\hat{\mathbf{z}}$	unit vectors in the direction of x, y, and z-coordinate axes $[\mathring{A}]$
z_{unit}	unit cell size along the z-axis/surface normal $[\mathring{A}]$

List of publications

Papers

- Hladík, M.; Fejfar, A.; Vázquez, H. Doping of the hydrogen-passivated Si(100) electronic structure through carborane adsorption studied using density functional theory. *Phys. Chem. Chem. Phys.* **2021**, 23, 20379 – 20387, doi: 10.1039/D1CP01654G
- Hladík, M.; Vetushka, A.; Fejfar, A.; Vázquez, H. Tuning of the gold work function by carborane films studied using density functional theory. *Phys. Chem. Chem. Phys.* **2019**, 21, 6178 – 6185, doi: 10.1039/C9CP00346K
- Hladík, M.; Fejfar, A.; Vázquez, H. Carboranedithiol-mediated surface transfer doping of the monohydride- and the dihydride-terminated Si(100) wafers. *in preparation*

Conferences

- Hladík, M.; Fejfar, A.; Vázquez, H.; *Doping of the hydrogen-passivated Si(100) surface by carborane films studied using DFT*, English, poster, 18$^{\text{th}}$ IUVSTA International Summer School on Physics at Nanoscale 2021, Prague, Czech republic, June 2021.
- Hladík, M.; Vázquez, H.; Vetushka, A.; Fejfar, A.; *Stability of carborane films on hydrogen-passivated silicon surfaces studied using density functional theory*, English, oral presentation, Smart NanoMaterials 2019, Paris, France, December 2019.
- Hladík, M.; Vázquez, H.; Vetushka, A.; Fejfar, A.; *Tuning of gold work function by carborane films studied using van der Waals DFT*, English, poster, 9$^{\text{th}}$ International Conference on Molecular Electronics 2018, Paris, France, December 2018.
- Hladík, M.; Vázquez, H.; Vetushka, A.; Fejfar, A.; *Tuning of gold work function by carborane films using a Density Functional Theory*, English, oral presentation, International Conference on Nanoscience + Technology 2018, Brno, Czech republic, July 2018.
- Hladík, M.; Vázquez, H.; Vetushka, A.; Fejfar, A.; *Self-assembled carboranes chemisorbed on Au(111) surfaces studied by Density Functional Theory*, English, poster, 16$^{\text{th}}$ IUVSTA International Summer School on Physics at Nanoscale 2017, Devět Skal, Czech republic, June 2017.
- Hladík, M.; Vázquez, H.; Vetushka, A.; Fejfar, A.; *Binding of Carboranes on Au(111) Studied by Density Functional Theory*, English, oral presentation, 5$^{\text{th}}$ International Education Forum on Environment and Energy Science 2016, San Diego, California, USA, December 2016.
- Hladík, M.; Vázquez, H.; Vetushka, A.; Fejfar, A.; *Carboranes binding on metal surfaces studied by Density Functional Theory*, English, poster, 6$^{\text{th}}$ EuChemS Chemistry Congress 2016, Seville, Spain, September 2016.

Appendices

A Adiabatic connection

The exact $E_{\mathrm{XC}}[\rho]$ correctly describes all forces in the system, including dispersions. Its structure can be expressed via the adiabatic connection formula, i.e. the formula that adiabatically connects the KS reference system to the real one by gradually turning on the electron-electron interaction operator, $\lambda\hat{V}_{\mathrm{ee}}$, where $\lambda \in \langle 0,1\rangle$ is the coupling strength parameter. The adiabatic coupling transfer the contribution of $T_{\mathrm{C}}[\rho]$ into the exchange-correlation hole to make the hole exact [54].

The electron density fluctuations, as the source of long-range forces, can be described in terms of the time-depend response of the electron density, $\rho(\mathbf{r},t)$, at time t to the applied external potential, $\mathcal{V}_{\mathrm{en}}(\mathbf{r}',t')$, at time $t' < t$. For small fluctuations that do not excite the system, one gets:

$$\rho(\mathbf{r},t) = \iint \chi(\mathbf{r},\mathbf{r}',t-t')\,\mathcal{V}_{\mathrm{en}}(\mathbf{r}',t')\,\mathrm{d}\mathbf{r}'\,\mathrm{d}t' \tag{A.1}$$

where $\chi(\mathbf{r},\mathbf{r}',t-t') = \delta\rho(\mathbf{r},t)/\delta\mathcal{V}_{\mathrm{en}}(\mathbf{r}',t')$ is the linear density response function. By means of the fluctuation-dissipation theorem[①] [130], the density response function is related to $E_{\mathrm{XC}}[\rho]$ via the electron-pair density:

$$\rho_{2,\lambda}(\mathbf{r},\mathbf{r}') = \frac{1}{\pi i}\int_0^\infty \chi_\lambda(\mathbf{r},\mathbf{r}',\omega)\,\mathrm{d}\omega + \rho(\mathbf{r})\rho(\mathbf{r}') - \delta(\mathbf{r}-\mathbf{r}')\rho(\mathbf{r}) \tag{A.2}$$

where $\chi_\lambda(\mathbf{r},\mathbf{r}',\omega)$ is the Fourier image of the density response at coupling strength λ. The result is the adiabatic-connection fluctuation-dissipation formula for the exact $E_{\mathrm{XC}}[\rho]$ [68]:

$$E_{\mathrm{XC}}[\rho] = \frac{1}{2}\int_0^1 \left\{ \iint \left[\int_0^\infty \chi_\lambda(\mathbf{r},\mathbf{r}',\omega)\,\frac{\mathrm{d}\omega}{\pi i} - \delta(\mathbf{r}-\mathbf{r}')\rho(\mathbf{r}) \right] \frac{\mathrm{d}\mathbf{r}\,\mathrm{d}\mathbf{r}'}{|\mathbf{r}-\mathbf{r}'|} \right\} \mathrm{d}\lambda \tag{A.3}$$

Here, the second term in the square bracket is a divergent quantity called the self-energy, E_{self}, (not to be confused with the self-interaction), which is removed by the divergence in the first term. One defines the Hartree kernel: $\mathcal{W}(\mathbf{r},\mathbf{r}') = 1/|\mathbf{r}-\mathbf{r}'|$, and the trace of the matrix: $\mathrm{Tr}[\chi_\lambda\mathcal{W}] = \iint \chi_\lambda(\mathbf{r},\mathbf{r}')\mathcal{W}(\mathbf{r}',\mathbf{r})\,\mathrm{d}\mathbf{r}\,\mathrm{d}\mathbf{r}'$, where the Hartree kernel is symmetric: $\mathcal{W}(\mathbf{r},\mathbf{r}') = \mathcal{W}(\mathbf{r}',\mathbf{r})$. In addition, one introduces the linear density response to the applied Kohn-Sham potential: $\widetilde{\chi}(\mathbf{r},\mathbf{r}',t-t') = \delta\rho(\mathbf{r},t)/\delta\mathcal{V}_{\mathrm{KS}}(\mathbf{r}',t')$, which is related to the bare response via the Dyson-type equation: $\chi_\lambda = \widetilde{\chi}_\lambda + \lambda(\widetilde{\chi}_\lambda\,\mathcal{V}\,\chi_\lambda)$, leading to the simpler expression for $E_{\mathrm{XC}}[\rho]$:

$$E_{\mathrm{XC}}[\rho] = \int_0^\infty \left\{ \int_0^1 \mathrm{Tr}\left[\frac{\widetilde{\chi}_\lambda(\omega)\,\mathcal{W}}{1-\lambda(\widetilde{\chi}_\lambda(\omega)\,\mathcal{W})} \right] \mathrm{d}\lambda \right\} \frac{\mathrm{d}\omega}{2\pi i} - E_{\mathrm{self}} \tag{A.4}$$

[①] It relates internal fluctuations of any physical quantity describing a system in equilibrium with the dissipative non-equilibrium response of that quantity to an external perturbation of the system.

B van der Waals density functional

A practical form of the vdW-DF functional (Eq. 1.21) stems from the work of Dion et al. [64], where the starting point is Eq. A.4 and one goes through several (a total of six) approximation steps. The **first** approximation is the full potential approximation where $\widetilde{\chi}_\lambda$ is replaced by $\widetilde{\chi}_1 \equiv \widetilde{\chi}$, making the inner λ-integration in the curly bracket explicitly solvable. The result is: $-\mathrm{Tr}[\ln(1-\widetilde{\chi}\mathcal{W})]$, which is asymptotically exact for the long-range correlation effects. In order to express $E_{\mathrm{XC}}[\rho]$ in terms of the electron density, it is convenient to replace the response function $\tilde{\chi}$ with the polarisability, α, or the dielectric constant, ϵ. In matrix notation, the first-order electron density change reads: $\delta\rho = \boldsymbol{\nabla}\cdot\boldsymbol{\alpha}\cdot\boldsymbol{\nabla}(\delta\mathcal{V}_{\mathrm{KS}})$, so the density response is: $\widetilde{\chi} = \boldsymbol{\nabla}\cdot\boldsymbol{\alpha}\cdot\boldsymbol{\nabla}$. The polarisability tensor $\boldsymbol{\alpha}$ is related to the dielectric tensor $\boldsymbol{\epsilon}$ by: $\boldsymbol{\epsilon} = \mathbf{1} + 4\pi\boldsymbol{\alpha}$, giving rise to $E_{\mathrm{XC}}[\rho]$ expressed in terms of $\boldsymbol{\epsilon}$:

$$E_{\mathrm{XC}}[\rho] = -\frac{1}{2\pi i}\int_0^\infty \mathrm{Tr}\Big[\ln\left(\boldsymbol{\nabla}\cdot\boldsymbol{\epsilon}\cdot\boldsymbol{\nabla}G\right)\Big]\,\mathrm{d}\omega - E_{\mathrm{self}} \tag{B.1}$$

where $G = -\mathcal{W}/(4\pi)$ is the Coulomb Green's function which satisfies: $\nabla^2 G = 1$. In an isotropic medium, the tensor $\boldsymbol{\epsilon}$ corresponds only to the dielectric constant ϵ, so $\boldsymbol{\nabla}\cdot\boldsymbol{\epsilon}\cdot\boldsymbol{\nabla}G \Rightarrow \epsilon\boldsymbol{\nabla}\cdot\boldsymbol{\nabla}G = \epsilon$. This gives the regular functional $E^0_{\mathrm{XC}}[\rho]$:

$$E^0_{\mathrm{XC}}[\rho] = \int \rho(\mathbf{r})\,\varepsilon^0_{\mathrm{XC}}(\mathbf{r})\,\mathrm{d}\mathbf{r} = -\frac{1}{2\pi i}\int_0^\infty \mathrm{Tr}\Big[\ln(\epsilon)\Big]\,\mathrm{d}\omega - E_{\mathrm{self}}\,, \tag{B.2}$$

i.e. the energy of the jellium within the vdW-DF approximation, where $\varepsilon^0_{\mathrm{XC}}(\mathbf{r})$ is the corresponding one-particle reference energy. The functional $E^0_{\mathrm{XC}}[\rho]$ is a good approximation for a slowly varying system, becoming exact for a uniform system.

The **second** approximation is subtracting Eq. B.2 from Eq. B.1 and getting the non-local functional $E^{\mathrm{nl}}_{\mathrm{C}}[\rho]$. At this stage, it is necessary to express both $E^0_{\mathrm{XC}}[\rho]$ and $E^{\mathrm{nl}}_{\mathrm{C}}[\rho]$ in the same quantity, hereafter called the generalised polarisation function, $S_{\mathrm{XC}} \equiv \ln(\epsilon)$. Therefore, one has to introduce the **third** approximation to replace the tensor $\boldsymbol{\epsilon}$ by the isotropic constant ϵ directly in the expression for $E_{\mathrm{XC}}[\rho]$ (Eq. B.1), then employ the substitution: $\epsilon = \exp(S_{\mathrm{XC}})$, and expand the trace, $\mathrm{Tr}[\ln(\nabla(\exp(S_{\mathrm{XC}}))\cdot\nabla G)]$, to second order in S_{XC}. The first-order term, $\mathrm{Tr}[S_{\mathrm{XC}}]$, belongs to $E^0_{\mathrm{XC}}[\rho]$. The second-order term is identified as the vdW-DF-based approximation for $E^{\mathrm{nl}}_{\mathrm{C}}[\rho]$:

$$E^{\mathrm{nl}}_{\mathrm{C}}[\rho] \approx -\frac{1}{4\pi i}\int_0^\infty \mathrm{Tr}\Big[\ln\left(S^2_{\mathrm{XC}} - (\nabla S_{\mathrm{XC}}\cdot\nabla G)^2\right)\Big]\,\mathrm{d}\omega \tag{B.3}$$

The **fourth** approximation is related to expressing S_{XC} in terms of the electron density. This strategy is performed in the plane-wave representation where the Fourier image of the generalised polarisation, $S_{\mathrm{XC}}(\mathbf{k},\mathbf{k}',\omega)$, is the prominent quantity. The approximated $S_{\mathrm{XC}}(\mathbf{k},\mathbf{k}',\omega)$ is symmetric with respect to time inversion, which is fulfilled when $S_{\mathrm{XC}}(\mathbf{k},\mathbf{k}',\omega) = [\widetilde{S}(\mathbf{k},\mathbf{k}',\omega) + \widetilde{S}(-\mathbf{k}',-\mathbf{k},\omega)]/2$, where the quantity $\widetilde{S}$ reads:

$$\widetilde{S}\Big(\mathbf{k},\mathbf{k}',\omega\Big) = \int e^{-i(\mathbf{k}-\mathbf{k}')\cdot\mathbf{r}}\,\frac{4\pi\rho(\mathbf{r})}{[\omega+\omega_k(\mathbf{r})][-\omega+\omega_{k'}(\mathbf{r})]}\,\mathrm{d}\mathbf{r}\,. \tag{B.4}$$

Here, $\omega_k(\mathbf{r})$ is the plasmon dispersion frequency. Regarding $E^0_{\mathrm{XC}}[\rho]$ described by Eq. B.2 (with the term $\mathrm{Tr}[S_{\mathrm{XC}}]$), substituting for S_{XC} by means of Eq. B.4, one gets the one-particle energy: $\varepsilon^0_{\mathrm{XC}} \propto \int[(1/\omega_k) - (1/k^2)]\,\mathrm{d}\mathbf{k}$, where the second term belongs to E_{self}. At the large-k limit, the dispersion frequency approaches to $\omega_k \to k^2/2$, making

this frequency cancelling the divergent behaviour of E_{self} and thus causing the one-particle energy $\varepsilon^0_{\text{XC}}$ to be zero. This corresponds to a state of fast moving free electrons with no time to interact with each other. At the small-k limit, ω_k is a constant.

The **fifth** approximation utilises the small and the large-k limits of $\omega_k(\mathbf{r})$ and constructs the final vdW-DF-based relation where the frequency $\omega_k(\mathbf{r})$ smoothly switches between the constant and the quadratic behaviours in k:

$$\omega_k(\mathbf{r}) = \frac{k^2}{2}\left[1 - \exp\left(-\frac{4\pi}{9}\frac{k^2}{(k_0(\mathbf{r}))^2}\right)\right]^{-1}. \tag{B.5}$$

Here, $k_0(\mathbf{r})$ is the reciprocal parameter witch sets the length scale, $1/k_0$, for the vdW-DF framework. Since the energy $\varepsilon^0_{\text{XC}}(\mathbf{r})$ has an explicit form: $\varepsilon^0_{\text{XC}} = -(3/(4\pi))k_0$, resembling the exchange energy within the LDA strategy[②], $k_0(\mathbf{r})$ is related to the local Fermi wave-vector, k_{F} (see Fn. ②), via the formula: $k_0(\mathbf{r}) = (\varepsilon^0_{\text{XC}}/\varepsilon^{\text{LDA}}_{\text{X}})k_{\text{F}}$.

The **last** approximation derives a particular structure of $\varepsilon^0_{\text{XC}}$ which is exclusively assembled from the LDA-based correlation energy and the LDA-based gradient-corrected exchange energy:

$$\varepsilon^0_{\text{XC}}(\mathbf{r}) \approx \varepsilon^{\text{LDA}}_{\text{C}}(\mathbf{r}) + \varepsilon^{\text{LDA}}_{\text{X}}(\mathbf{r})\,F^0_{\text{X}}(s(\mathbf{r})) = \varepsilon^{\text{LDA}}_{\text{C}}(\mathbf{r}) + \varepsilon^{\text{LDA}}_{\text{X}}(\mathbf{r})\left[1 - \frac{Z_{\text{ab}}}{9}(s(\mathbf{r}))^2\right] \tag{B.6}$$

where $F^0_{\text{X}}(s(\mathbf{r}))$ is the exchange enhancement factor defined as the function of the reduced density gradient $s(\mathbf{r})$ with the dimensionless quantity $Z_{\text{ab}} = -0.8491$ [64] taken from the gradient expansion for slowly varying electron gas.

All given non-empirical approximations lead to the final form of $E^{\text{nl}}_{\text{C}}[\rho]$:

$$E^{\text{nl}}_{\text{C}}[\rho] = \frac{1}{2}\iint \rho(\mathbf{r})\,\Theta(\mathbf{r},\mathbf{r}')\,\rho(\mathbf{r}')\,\mathrm{d}\mathbf{r}\,\mathrm{d}\mathbf{r}', \tag{B.7}$$

which represents the equivalent formulation of Eq. B.3, so the non-local part vanishes at the jellium-model limit. Here, $\Theta(\mathbf{r},\mathbf{r}') = \Theta(d,d')$ is the non-local kernel mediating an effective interaction between the densities $\rho(\mathbf{r})$ and $\rho(\mathbf{r}')$; its spatial dependence is given by effective dimensionless separations $d = k_0(\mathbf{r})|\mathbf{r}-\mathbf{r}'|$ and $d' = k_0(\mathbf{r}')|\mathbf{r}-\mathbf{r}'|$, where $k_0(\mathbf{r})$ parametrise the strength of the interaction in terms of the local density and its generalised gradient. For practical calculations, it is convenient to demonstrate the kernel only as a function of two variables, namely the scaled distance, $D = (d+d')/2$, and the measure of asymmetry, $\delta = |d-d'|/(d+d')$, between $\mathbf{r}$ and $\mathbf{r}'$, ranging in $D \in \langle 0,\infty)$ and $\delta \in \langle 0,1)$, respectively. Dion et al. [64] reveal the plots of $4\pi D^2\Theta$ vs D for several values of δ to show the interaction is repulsive at shorter distances, becomes attractive with a minimum at intermediate distances, and asymptotically goes to zero at longer distances. The interaction is strongest when $\rho(\mathbf{r})$ and $\rho(\mathbf{r}')$ are equivalent, i.e. $\delta = 0$. At the jellium-model limit ($\delta = 0$), $\int 4\pi D^2\Theta\,\mathrm{d}D = 0$, which means that the non-local correlations do not change the energy of the uniform electron gas.

The regular part of the vdW-DF functional, i.e. the energy of the jellium under the full potential approximation, is nearly equivalent to the LDA. However, the form of $E^0_{\text{XC}}[\rho]$ is not local because of the enhancement factor $F^0_{\text{X}}(s)$ in Eq. B.6. In particular, Dion et al. [64] compile $E^0_{\text{XC}}[\rho]$ from the GGA exchange and the LDA correlation energies. Indeed, $E^{\text{nl}}_{\text{C}}[\rho]$ is assumed to include all non-local correlations and the spurious double counting could occur when using the GGA correlation contributions, hence the use of the LDA is recommended. On the other hand, $E^0_{\text{XC}}[\rho]$ should cover all exchange

[②] The LDA-based exchange energy per particle reads: $\varepsilon^{\text{LDA}}_{\text{X}} = -(3/4\pi)\,k_{\text{F}}$, where $k_{\text{F}} = (3\pi^2\rho)^{1/3}$ is the local Fermi wave-vector

effects that the GGA adequately describes. Based on numerical results, Dion et al. employ the revised PBE (revPBE) exchange functional [60] that exhibits a more significant repulsive character compared to the original PBE, as its exchange enhancement factor grows faster in the range of the generalised gradient $s(\mathbf{r})$ up to about $s = 1.5$ [131]. As a result, the revPBE does not cause spurious exchange-mediated binding dispersions, typically exhibited by LDA and several GGA exchange functionals when studying noble gas dimers [132].

The Dion's non-empirical functional is promising for a variety of issues with layered and general geometries, such as dispersion forces between parallel graphene sheets forming graphite, adsorption of hydrocarbons on metal and semiconductor surfaces, binding in molecular dimers and molecular crystals, hydrogen storage in graphite and metal-organic frameworks, and others [133]. However, the more aggressive enhancement factor of the revPBE functional slightly overestimates bulk lattice constants and equilibrium separations between vdW bound fragments [64, 131, 133] and underestimates hydrogen-bond strengths [134]. Despite its shortcomings, this vdW-DF functional has its share of successes in DFT calculations of non-local correlation contributions, it greatly outperforms its semi-local counterparts in describing molecular monolayers adsorbed on metals [135–137] or semiconductors [138, 139], making the final junctions more stable and generally more consistent with experimental and *ab initio* data.